The Role of Quantum Confinement Effects in the Visible Photoluminescence from Silicon Nanoparticles

by

Eric Werwa

B.S. Eng. Materials Science and Engineering
University of Pennsylvania, 1992

Submitted to the Department of Materials Science and Engineering
in partial fulfillment of the requirements for the degree of

Doctor of Philosophy in Electronic Materials

at the

MASSACHUSETTS INSTITUTE OF TECHNOLOGY

September 1997

Signature of Author .....
Department of Materials Science and Engineering
August 8, 1997

Certified by .....
Kirk D. Kolenbrander
Associate Professor of Electronic Materials
Thesis Supervisor

Accepted by .....
Linn W. Hobbs
John F. Elliott Professor of Materials
Chairman, Departmental Committee on Graduate Students

The Role of Quantum Confinement Effects in the Visible Photoluminescence from Silicon Nanoparticles

by

Eric Werwa

Submitted to the Department of Materials Science and Engineering
on August 8, 1997, in partial fulfillment of the
requirements for the degree of
Doctor of Philosophy in Electronic Materials

Abstract

Visible light emitting silicon nanostructures have received a great deal of attention from the materials research community because of their potential applications in optoelectronic and photonic devices. While light emission has been observed and exploited for device applications, debate has continued to rage about the identity of the light emitting species and the emission pathway. To seek a definitive answer to this perplexing question, thin films of silicon nanoparticles have been deposited using a pulsed laser ablation supersonic expansion cluster source. These films consist of a polydisperse collection of silicon particles embedded in a native oxide matrix which efficiently emits visible light under ultraviolet photoexcitation. The light emitting properties of these films have been studied by photoluminescence emission spectroscopy. Standard films were found to consist of crystalline silicon particles using a variety of techniques, including transmission electron microscopy, x-ray photoelectron spectroscopy, and x-ray diffraction. Scanning transmission electron microscopy, however, revealed that the films consist of a fairly continuous film of silicon, which may be an amorphous layer that could potentially be the luminescing species.

To determine the luminescing species from among this array of particle sizes, several size selection schemes were investigated. Size discrimination attempts based on particle size based velocity slip, crossed beam based gas jet particle deflection, and radiation pressure based light deflection of particles were unable to reveal the source of the emission. Finally, a quadrupole mass filter was employed in order to select out specific sizes of particles. Due to the initial kinetic energies of the particles, it was not possible to eliminate all of the larger particles from the deposited films. It was possible to exclude the very small, structurally disordered particles, which can migrate on the substrate and form a continuous amorphous silicon layer. Visible photoluminescence has been observed from films deposited without these smallest clusters, indicating that the light emitting species is not this continuous amorphous silicon. Parallel study of larger silicon particles reveals no light emission, indicating that the intermediately sized particles, which are of the size range to exhibit quantum confinement effects, are the emitting species.

To confirm this and to study the luminescence recombination pathway, the excitation intensity dependence of the photoluminescence (PL) was studied as a function of temperature and temporal nature of the light source. It was found that the excitation intensity dependence of the PL depends strongly on the temporal nature of the light source. Pulsed excited

luminescence is characteristic of a state filling mechanism while continuous source excitation results in behavior characteristic of Auger recombination. The presence of both of these competing mechanisms means that state filling exists as a viable mechanism, which indicates that quantum confinement effects are responsible for the visible photoluminescence. These results are consistent with previous studies in which changing the mean particle size resulted in a shifting of the photoluminescence emission spectrum.

Thesis Supervisor: Kirk D. Kolenbrander
Title: Associate Professor of Electronic Materials

Contents

List of Figures

Acknowledgments

Well, I must admit that I learned a whole lot of things while I was at MIT. I learned a great deal about materials science from my classes, but I learned far more about it in the lab and while being a TA. I learned a lot about doing science while designing my thesis project, figuring out why it wasn't working, and then finally coming up with a way to put together a thesis and get out. I also had the chance to learn which aspects of this education I really enjoyed and wanted to spend my life after MIT pursuing, and which ones I didn't like as much. For all of this I thank my advisor, Kirk Kolenbrander. He gave me the opportunity to make the decisions (many times to my chagrin) and to get exposed to different things and to really learn who I am and what I want to do. I learned a lot from watching him supervise the students in our group and teach a class, lessons I hope to take with me and use well when I am in that position. He was also a friend, supportive in the times when grad school didn't look all that rosy and concerned about more than just how things were going in the lab. I know my graduate school experience was different from those of many other students and I am glad for that, and for that I thank Kirk.

I thank the members of my thesis committee, Professor Lionel C. Kimerling and Dean John B. VanderSande, whose careful consideration of this thesis and the lively discussion we had about it made this a far better document than it was when I first wrote it. Much of the work that is covered here relied on the experimental assistance of others, especially those people who run the shared experimental facilities. I thank Tim McClure, Libby Shaw, Mike Frongillo, Dr. Tony Garrat-Reed, Peter Kloumann, Dr. Chuxin Zhou, and Dr. Das Chowdhury for their help and for putting up with some of the ridiculous requests that I made of them.

I thank my parents, who always claimed that they had no idea what I was doing but continued to support me and believe in my ability no matter how long I was here. Speaking of support, I am grateful to 3M and AT&T Bell Labs for the fellowships. Thanks to Dr. Bob Messner from 3M for keeping me in the rolodex many years after I was no longer on the official payroll and inviting me to the free food events.

A lot of what I learned at MIT happened outside of the classroom. For that, I must thank the many great people I met while I was here, and I guess I need to thank MIT for bringing them together in this "unique" environment. The other members of the Kolenbrander group were an invaluable resource, from discussions of experiments and data to sporting events and everything in between. In particular, I thank Dr. Arun Seraphin, Dr. Shih-Tung Ngiam, Tracey Burr, and Leon Chiu, without whom graduate school would have been a lonely time in a desolate lab (as I found during my final year). They were great co-workers and great friends, and I will always remember the times we spent together (like that midweek Yankees-Red Sox day game). There were many other people who I thank for their conversations about everything, both daily at lunch and in the halls and on those many trips to the Muddy (which I would also like to thank). I don't know if I can even remember them all, but they include Doug Blom, Dr. Jim Foresi, Dr. Mike Morse, Dr. Harold Ackler, Dr. AnnaLena Thilderqvist, Dr. Christopher San Marchi, Rita Gupta, Erika Abbas, Dr. Tom McNamara, Kamala Crawley, Sean Donovan, Laura Giovane, Dr. Heather Inglefield, Dr. Bethanie Stadler, Tony Nichtawitz, Erin Lavik, "the kids" Debbie Lightly and Aaron Blanchet, and the inimitable Peter Heron.

I did many things to help me get through the time here, and I thank the people I did them with: my days as social chairman, and the assistance of Commander Vegetable, Kathy Chen, with the department picnic; the MIT championship softball team, led by John Matz; the hockey teams with Mark Brillhart, Dr. Doug Matson, Dr. Darren Castro, and Josh Freedman; the wonderful MIT gym and Matz and Ali Farah, who dragged me there and got me into the habit (and all of the gym celebrities who kept me going, like Wally, Batman, the Angry Guy, Annoying Guy, Ugly Pants Guy, Towel on the Shoulders Guy, John, the Sweating Guy, Annoying Woman, Squatting Guy and Gilligan, Benching Guy, Wild Mouth Guy, $2^1/_2$ pound Guy, Underwear Guy, the Ape Man, and all the others); the Penn Club of Boston and the 1997 Boston Area Ivy League Alumni Softball League Champion Penn softball team; and all of the various educational outreach programs and Valarie Benezra and Dr. Patrick Tepesch who made it possible for me to participate in them. I would also like to thank Kevin Nash, Scott Hall, Shawn Michaels, Bret Hart, Howard Stern, Robin Quivers, Jackie Martling, Fred (Eric) Norris, and Gary Dell 'Abate. And as for everything written in

this thesis, well that's the bottom line because Stone Cold Said So!

Chapter 1

Introduction

1.1 Motivation: Photonics and Optoelectronics

Since the invention of the silicon integrated circuit, the microelectronics industry has maintained a rapid pace of technological innovation. Dramatic increases in the speed and power of computing systems have been achieved while at the same time reducing size and cost. The continuing push for higher speed and lower cost telecommunications systems have fueled the drive to design new devices that can meet increasingly more stringent technical specifications. The change has been so dramatic that the fundamental physical limits of semiconductor microelectronics technology are in sight, and in order to continue the improvements in speed and information and computing capacity, new technological avenues need to be investigated. In particular, the fields of optoelectronics, in which electrons and holes are used to control optical signals, and photonics, in which light is used to control optical signals, may provide the building blocks for the development of this new technology.

In the constant push to improve speed and computing power, device dimensions have reduced dramatically and the resulting density of devices on a chip has skyrocketed. As predicted by Moore's law, the transistor density for new microprocessors has doubled every two years. This increase in device density means that more and more information must be brought on and off of a chip. The interconnections between traditional chips and the rest of a computer are the pinouts, and as such the number of pins on a microprocessor has increased as well. For an Intel 80286 microprocessor, there were 40 pins; for an 80386 there

were 100 pins; an 80486 had 168 pins; a Pentium chip has 296, and for the next generation of Pentium Pro processors, there are 387 pins. This progression cannot continue forever due to capacitance issues between the metal lines that are connected to the pins. As the lines grow thinner and closer together the capacitive losses between them limit the speed of operation. There is also simply not enough space to attach more pins onto the chip. This presents opportunities for more efficient information transfer. The telecommunications industry has already "seen the light" with a switch to optical fibers, which can carry many thousands of signals on the same fiber. This would require only one connection to each chip, rather than hundreds. The only missing link at this point is the key optoelectronic device, a light emitter integrated onto the microprocessor chip. It is also of interest to capitalize on the silicon explosion by making displays that can be integrated with the microelectronic circuitry. In order to do this, a visible light emitter based on silicon must be devised.

Extending the issues of speed and capacity of telecommunications and microelectronics even further, there are even greater opportunities in the area of switching information flow. Currently, optical signals are converted into electronic ones by detectors, then processed electronically, and then reconverted back into light. This switching process is slowed by the fact that electrons are being used. Electrons, while quite small, have a real mass, and thus the maximum speed they can achieve is limited by relativity. By performing the switching process optically, the ultimate speed would be the speed of light, and great advances could be made. There is great interest in creating the necessary photonic materials, in which the light could be switched using light, to make these switches a reality. This will require materials with excellent nonlinear optical properties, in particular the ability to achieve absorption saturation when exposed to sufficient amounts of light. As with optoelectronic materials, it is also interesting to try to make these photonic materials from silicon, due to the great commercial investment in, knowledge base about, and advantageous properties of silicon.

1.2 Materials Choices

Over the past several decades, a great deal of research and development effort has been expended in designing new optoelectronic and photonic devices and developing new materials

from which to make them. The development of optoelectronic devices, such as semiconductor lasers, detectors, and light emitting diodes, and photonic devices, such as directional couplers and all-optical switches, have been spurred by the need to improve speed and quality of information flow. The materials these devices have been manufactured from have been chosen specifically for their outstanding optical properties, having direct band gaps with magnitudes in the wavelength range of interest, such as GaAs, CdSe, GaP, GaN, AlGaAs, and AlInGaAs. Many of these materials are either very expensive or they are incompatible with silicon microelectronics technology, either due to processing or materials properties issues. This makes it difficult to realize integrated microelectronic and optoelectronic or photonic systems that are affordable.

Ideally, photonic and optoelectronic devices would be made using silicon, which would guarantee compatibility with current microelectronics processing. The advantages of silicon are numerous. As an elemental semiconductor, there are no issues of stoichiometry maintenance in silicon growth. Silicon can be easily doped by introducing impurities that substitute on lattice sites for silicon atoms. These dopants can provide additional electrons and holes into the material, allowing for the fabrication of optoelectronic devices utilizing p-n junctions, such as lasers and LED's. The doping levels can be readily adjusted to modify the electronic properties of the silicon, so that these devices can be optimized for best performance. Silicon also grows a robust and yet removable surface oxide, silicon dioxide (SiO_2) which serves to passivate the unsatisfied bonds that exist at the surface of the material. This oxide is an excellent insulator and can be used to isolate microelectronic devices on a single wafer.

Aside from its physical properties, the major advantage of silicon is that huge amounts of resources have been devoted to materials research and development in silicon since the invention of the transistor in 1947. Advances in crystal growth technology have allowed the production of very large, defect free crystal boules. Refinements in processing have enabled the growth of oxide layers with very low densities of oxide/silicon interface states, resulting in high performance devices by eliminating electronic trap states. Large financial investments in equipment and research and development were necessary to achieve these advances. This has significant ramifications regarding the possibilities of switching to a new materials system. The giants of the semiconductor industry are very hesitant to give up

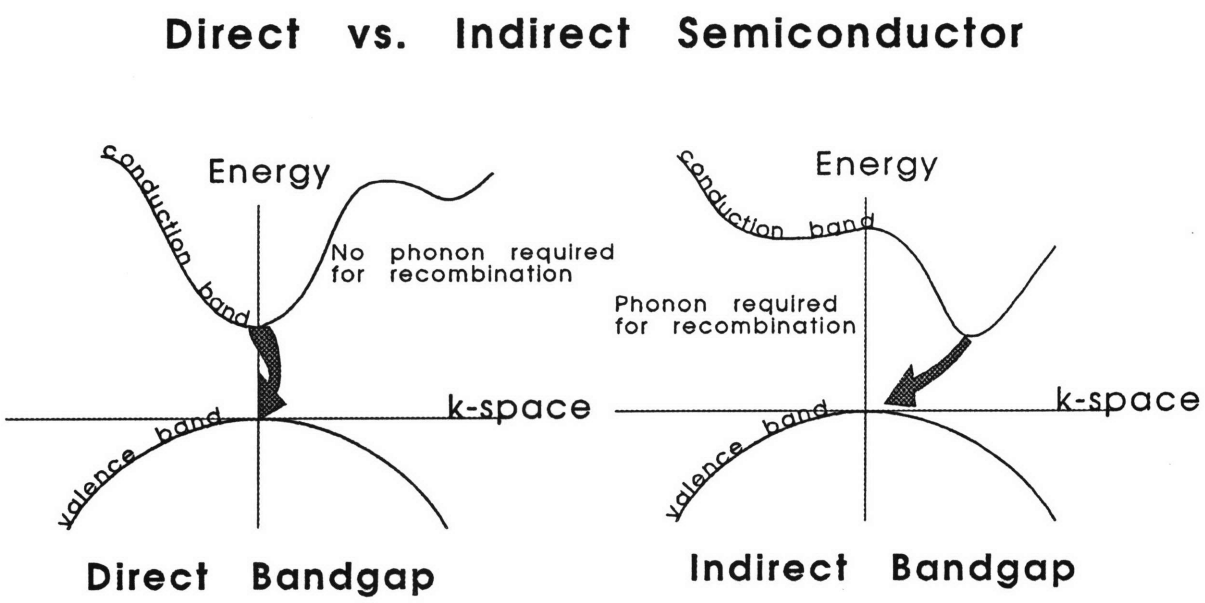

Figure 1-1: Schematic representation of both direct and indirect energy gap band structures in semiconductors. A phonon is required for transitions across the gap in the indirect gap material

silicon and all of the equipment and knowledge for which they paid, as well as surrendering their positions as industry leaders, to switch to a completely different materials system so as to be able to employ optoelectronic and photonic devices. Unfortunately, bulk silicon is not a particularly suitable optical material for these applications. It has an indirect energy gap, which translates into poor light emission efficiency, and its band gap energy is 1.12 eV, which lies in the infrared but not at an optical fiber attenuation minimum, making silicon unsuitable for both fiber transmission sources and display applications.

1.3 Energy Gaps in Semiconductors

The suitability of a semiconductor material for optical applications is determined by its energy band structure. There are two important features of the band structure upon which the material can be judged: the nature of the energy gap and its magnitude. There are two types of semiconductor band gaps, direct and indirect, which are shown schematically in Figure 1-1. A direct gap semiconductor is one in which the maximum of the valence

band and the minimum of the conduction band occur at the same value of **k**, the momentum vector of the wavefunction representing the carriers. An indirect gap semiconductor is one in which the valence band maximum and conduction band minimum occur at different values of **k**. For transitions in which carriers move from one band into the other, it is a fundamental law that momentum must be conserved. In the event of photoexcitation of carriers, in which light (which has very little momentum) is the promoting agent, it is easy to transfer electrons up into the conduction band for a direct gap material. In fact, if the light is of sufficient energy above the band gap, there may be states available in the conduction band at the same momentum in an indirect gap material, which means absorption transitions can be easy as well. When the time comes for the excited electron to recombine, however, there are significant differences between the two types of semiconductors. Generally, the electron will make its way to the minimum of the conduction band before the transition, no matter how much energy it was originally given, and the hole it is destined to recombine with will float to the top of the valence band. In a direct gap material, these two actors will have the same value of **k**, and so their recombination can be made with only a change in energy required, but no change in momentum. This can be achieved by the emission of a photon only, which is a very efficient process. For an indirect gap material, things are not so simple. The electron and hole will have different values of momentum, which means that recombination will require a change of energy, which can be handled with a photon, and also a change of momentum, which requires the presence of a phonon. This added degree of complexity makes the process far less likely, making light emission very inefficient from indirect gap semiconductors.

1.4 Carrier Recombination Mechanisms

When light is shined upon a collection of atoms, if the energy of the photons corresponds to an allowed electronic transition in the system, it will be absorbed. For the case of individual atoms, these transitions occur between the quantized energy levels that the electrons can occupy, as dictated by quantum mechanics. For semiconductors, these transitions occur between bands of energy states, which develop as a result of the interaction of many atoms

in close proximity. In all cases, the energy that is stored in the promoted carriers in these excited states must be returned to the outside world if the system is to return to equilibrium. There are several pathways, grouped into two broad categories, through which this energy can be returned.

1.4.1 Radiative Recombination

Electronic excitations can occur in all materials, and thus all materials can also emit light. The light emission properties of semiconductors are of interest here. If this excitation is the result of the absorption of light, the emission is called photoluminescence. If the excitation is electrical, the emission is referred to as electroluminescence. Other forms of luminescence include cathodoluminescence, which results from the incidence of an electron beam, and chemiluminescence. The radiative recombination events that occur when the carriers excited by these various means come back together and produce light can be differentiated by the origin and location of the initial and final energy levels for the transition. These are shown schematically in Figure 1-2.

Atomic Transitions

It is a fundamental tenet of quantum mechanics that electrons in atoms can occupy only very specific orbitals and that these occur only at particular allowed energies (that is, they are quantized). When electrons in the occupied energy levels are provided with an amount of energy equal to that required to make a transition to a higher level, they will absorb that energy and make the transition. This excitation can be brought about by the absorption of light or it can be electrically stimulated. When the electrons in the higher state (the excited state) return to their original energy level (the ground state), an amount of energy equal to the energetic difference between these levels must be released, and it is often released in the form of a photon. This is the principle upon which neon lights are based - atoms in gaseous form are excited electrically and when the excited electrons return to the ground state, light is emitted. These transitions are very well defined, and so the spectral width of the emitted light is quite narrow.

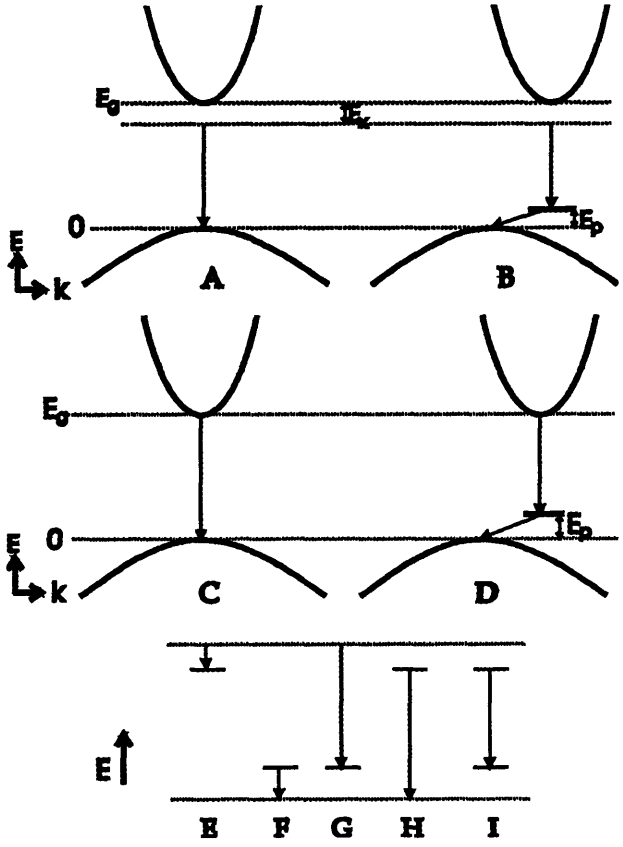

Figure 1-2: Schematic representation of radiative recombination mechanisms in semiconductors. Pictured are: Excitonic recombination in direct (A) and indirect (B) gap materials; band-to-band recombination in direct (C) and indirect (D) materials; shallow transition to donor (E) and acceptor (F) states; deep transitions to acceptor (G) and from donor (H) states; and donor-acceptor (I) transition.

Excitonic Recombination in Semiconductors

When light is absorbed in a semiconductor (photoexcitation), both an electron and a hole are generated. This pair, being oppositely charged, can experience a Coulombic attraction. This coupled electron and hole is known as an exciton, and the two species remain a distance apart known as the exciton radius. The exciton can move freely about the crystal (a free exciton) or it can be associated with a defect or an impurity (a bound exciton). Excitonic recombination is shown schematically, with the use of virtual energy level resulting from the Coulombic attraction, in Figure 1-2 a and b.

In the event that a free exciton recombines in a semiconductor with a direct energy gap, the energy of the emitted photon is given by

$$\Delta E = E_g - E_x$$

where E_g is the energy gap of the material and E_x is the ionization or binding energy of the exciton. This exciton binding energy is a measure of the Coulombic attraction between the electron and the hole. The binding energy is given by

$$E_x = \frac{-m_r e^4}{2h^2\varepsilon^2}$$

where m_r is the reduced mass and ε is the dielectric constant of the material. Thus, the energy of the emitted photon is slightly less than the magnitude of the energy gap between the valence and conduction bands. In an indirect gap material, it is necessary to include a phonon in the transition in order to conserve momentum, further reducing the energy of the emitted photon by the magnitude of the phonon energy. Excitons may also be bound to an impurity or defect in the lattice. In this case, the ionization energy for the bound exciton is

$$E_i = E_x + E_b$$

where E_b is the additional binding energy holding the exciton at the impurity or defect center.

Emission resulting from the recombination of excitons is very narrow spectrally and

appears as a sharp, intense line in a photoluminescence spectrum. While excitons are the lowest energy state for electron-hole pairs, excitonic emission is rarely seen except in the purest materials and at very low temperatures. This is because the exciton binding energy is small, and so excitons tend to break up in the presence of electric fields introduced by defects in the lattice or thermalize when the temperature is sufficiently high.

Band to Band Recombination

As a result of the aforementioned thermalization of excitons, electrons and holes are returned to the conduction and valence bands, respectively. It is possible for the carriers to recombine directly from the bands, a mechanism known as band to band recombination. This is shown schematically in Figure 1-2 c and d. For direct band gap semiconductors, these events result in the emission of a photon with an energy equal to the magnitude of the energy gap of the material. Owing to the law of conservation of momentum, band to band transitions in indirect gap semiconductors emit photons with energy slightly less than that of the band gap, with the difference representing the energy of the required phonon. For a direct gap material, these transitions occur very quickly, with the result being luminescence lifetimes in the nanosecond regime. With indirect gap materials, the necessity of a momentum conserving phonon extends the luminescence lifetime into the microsecond or millisecond range. This provides the opportunity for the carrier to follow some other, nonradiative recombination pathway before it can undergo band to band recombination. The spectral shape of these emissions will be determined by the density of electronic states near the edges of the bands, which determines the number of states available at particular energies from which the carriers will be making the transitions.

Impurity Level Transitions

Radiative transitions can also occur when an electron returns from the conduction band to the valence band through some intermediate state lying within the energy gap, depending on the energetics of that state. This is shown schematically in Figure 1-2 e-i. Such states are generated by impurities (such as dopant atoms, which are a different species from the rest of the material), defects (such as vacancies) or surfaces. Electrons or holes can be

trapped at these defects and, while being trapped, recombine with their oppositely charged counterparts located either in bands or other midgap states. If the energy levels associated with these traps are sufficiently close to the edges of the bands, such as shallow donor or acceptor states, it is possible for these recombination events to result in the emission of a photon. Recombination can occur between two levels that lie in the gap, and such transitions result in light emission that is very narrow spectrally. The magnitude of the energy of these transitions is dependent on the Coulombic interaction between the impurity centers and so it varies with their spatial separation. In general, radiative transitions coupled through an intermediate state are slower than band to band or excitonic recombination because of the extra time required for the carrier to move into the trap, leading to longer luminescence lifetimes.

1.4.2 Nonradiative Recombination

Electrons and holes can also combine nonradiatively, losing their energy by some mechanism other than light emission. In many systems, this pathway is faster than the radiative pathways previously discussed and so it dominates, resulting in very low light emission efficiency. For example, in germanium the radiative lifetime is on the order of 1 second while the minority carrier lifetime is in the millisecond range, which means that the carriers are losing their energy quickly by some other process before they ever get a chance to radiatively recombine. Typically, nonradiative recombination occurs when the energy difference between the excited state and an adjacent level is small, since there are many different ways to dump small amounts of energy into the system. As the energy difference increases, there are fewer energy loss alternatives, and radiative transitions become more likely. These nonradiative energy loss pathways are often difficult to detect as they manifest themselves only as a reduction of the emission efficiency. Nonradiative recombination can occur by several means.

Phonon Emission

One way an electron can reduce its energy is to emit a phonon, a lattice vibration. Individual phonons typically have energies on the order of millielectron volts (meV), which is much smaller than the spacing in energy between the excited state and ground state. For electrons

to reduce their energy by this mechanism when returning to the ground state, many phonons must be created. This mechanism is similar to the thermalization process that electrons undergo when they are excited high into the conduction band and they reduce their energy in order to drop down to the band edge.

Surface and Defect Recombination

Imperfections in the periodic crystalline lattice of a semiconductor can introduce perturbations into the smooth band structure of a perfect material. These perturbations can be manifested as electronic states lying near the middle of the previously forbidden band gap. This "stop over" point in the band gap reduces the magnitude of the energetic transitions that must be made in order to achieve recombination. As noted earlier, while larger energy transitions are generally achieved by radiative recombination, smaller steps are often achieved by nonradiative means. For the case of a surface, the ultimate imperfection in a crystal, a near continuum of states that spans the energy gap can develop. These states are associated with unsatisfied dangling bonds on the surface. This creates a nonradiative bridge from the excited state to the ground state that severely reduces radiative efficiency.

Auger Recombination

The Auger effect is an alternative means for electrons to reduce their energy and return to the ground state without emitting a photon. In the Auger effect, an electron in an excited state transfers its excess energy to another electron in an excited state and then returns to the ground state. The mechanism is shown schematically in Figure 1-3. The electron in the excited state which has received the additional energy may have enough energy to escape from the material completely, or it may be transferred to a higher energy state in the material. For an electron remaining within the material, it is then possible for the high energy electron to dissipate that excess energy through phonon emission until it returns to the band edge, where it can recombine radiatively or nonradiatively. Since this is a two electron recombination process, it is not likely to occur when there are few electrons present in excited states. The Auger process becomes more probable as the degree of excitation increases (through an increase in pump intensity for optical excitation, for example), since there are more

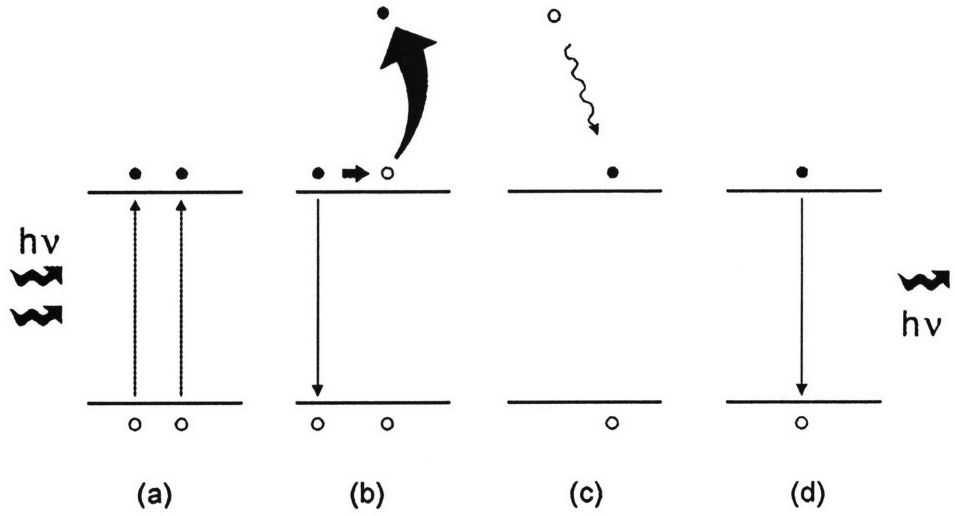

Figure 1-3: Schematic representation of the Auger nonradiative recombination process. In (a) two photons are absorbed, generating two electron hole pairs in the material. One pair recombines and the excess energy is transferred to the other pair(b). The carrier which has received the excess energy returns to its normal excited state through thermalization (c). The electron hole pair then recombines as usual, emitting a photon (d). The overall process produces only 1 photon for every 2 absorbed.

electrons available to participate. In a photoluminescence experiment, it would be expected that Auger recombination should become active at high levels of excitation intensity. This is evident in measurements of the photoluminescence emission intensity as a function of excitation intensity from semiconductors. These experiments reveal a linear increase of integrated emission intensity with increasing pump intensity up until some threshold pump intensity, at which point the integrated luminescence intensity begins to saturate. The saturation phenomenon is due to Auger recombination, with the extra carriers generated by the extra excitation photons recombining nonradiatively and not contributing any additional luminescence intensity.

In order to make commercially useful optoelectronic devices, they need to be integrable with silicon, but silicon has properties that are incompatible with optical applications. This leaves the $64,000 question: How does one make a silicon based or silicon compatible optical material?

1.5 Light Emitting Silicon-Based Materials

A number of methods have been proposed and investigated as a means of overcoming the natural shortcomings of silicon as an optical material. Most of the effort has focused on increasing the light emission efficiency, with the issue of the wavelength left relatively unaddressed. In order to realize an increase in emission efficiency, a means must be devised to bring electrons and holes closer together, which will enhance radiative recombination. This overlap can be increased in silicon systems by a variety of methods.

1.5.1 Impurities

When impurities are introduced into the silicon lattice, the energy band structure is modified by the addition of states lying within the energy gap associated with the impurity. These impurity states can serve both to change the energy of possible carrier transitions and to increase the likelihood for those transitions to occur. This increased transition probability is a result of the relaxation of the momentum selection rules for electronic transitions occurring around this localized impurity. This can be understood by considering the Heisenberg

uncertainty principle, stated as

$$\Delta k \cdot \Delta x \geq \hbar$$

where Δk is the uncertainty in the momentum of the carrier, Δx is the uncertainty in the position of the carrier. The principle states that it is not possible to know the momentum and the position of a carrier with infinite precision. Thus, if a transition occurs at an impurity, which we can know the position of very precisely (Δx is very small), then we cannot know the momentum very well. This knowledge can be transferred to what is known about the transitions between energy states in semiconductors. It is necessary for these transitions to conserve both energy and momentum. For a typical indirect gap semiconductor, transitions between the bands require a lattice vibration to be present in order to conserve momentum, making these transitions unlikely. In the case of a transition involving an impurity state, the uncertainty in the momentum is great enough that the momentum selection rules are relaxed and the transitions become more likely, thus increasing the probability of radiative recombination. There are two common types of impurity centers in silicon, isoelectronic traps and rare earth element dopants.

Isoelectronic traps are states that result from the presence of impurities in silicon which are isovalent with silicon in the diamond cubic lattice.[1] Common examples of this are sulfur doped Si and complexes of four lithium atoms replacing a silicon vacancy. The luminescence properties of isoelectronically doped materials vary depending upon the dopant species, but they typically emit in the infrared portion of the spectrum with an emission efficiency of only a few percent at low temperature and even less at room temperature. These materials tend to have a long radiative transition lifetime, meaning that competing faster, nonradiative transitions can reduce the radiative efficiency.

Rare earth doped silicon takes advantage of the splitting of degenerate electronic states within the rare earth species upon its placement within the crystal field of the silicon lattice. These materials show great promise for light emitters to be coupled to existing fiber optic systems. This is a result of the very sharp emission lines and favorable wavelengths that result from the rare earth dopant. The most popular of these materials is erbium doped

silicon. Here, the luminescence results from transitions between two levels of the Er^{3+} 4f manifold of states. This transition is forbidden in bulk Er, but when the Er atom is placed into the silicon lattice, the crystal field of the silicon lattice removes this barrier to emission. The erbium emission occurs at $\lambda = 1.54\ \mu$m, which is fortuitously at the dispersion minimum for silica optical fibers. Er doped Si materials treated with oxygen have been found to emit efficiently at low temperature, with some loss of efficiency at room temperature. Light emitting diodes integrated on silicon wafers have been successfully fabricated from Er doped Si.[2]

1.5.2 Alloys and Compounds

Alloys of silicon and other isoelectronic elements, such a germanium and carbon, have been shown to emit in the near infrared and blue portions of the spectrum, respectively. In the SiGe systems, the band structure of silicon is engineered through the alloying process or through the growth of $Si/Si_{1-x}Ge_x$ superlattices. These materials are believed to have a pseudodirect gap, and as a result an enhanced radiative transition probability.[3] The alloying leads to the localization of excitons at sites separate from those representing nonradiative recombination pathways, which leads to an increase in emission efficiency.[4] There are a number of issues still to be resolved, such as the role of defects in limiting the emission efficiency and the impact of strain on the band structure.

SiC has been employed in the construction of blue light emitting diodes. In this case, the material retains an indirect gap, but the composition change expands the energy gap into the visible portion of the spectrum, specifically the blue region. The emission efficiency remains low, but this material can be doped to fabricate p-n junctions. Using these junctions, it is possible to electrically pump these devices to very high levels, so that while only a small fraction of the injected carriers result in the emission of visible light, the large number of carriers present produces significant emission intensity.

1.5.3 Polysilanes and Polymers

Highly disordered alloys (SiH_x) and silicon based polymers, such as polysilane $(SiH_2)_x$ and siloxene ($Si_6O_3H_6$) have also been found to exhibit strong visible and ultraviolet emission.[5]

Unfortunately, due to the nature of their microstructure these materials have poor electrical transport properties, making it impossible to fabricate useful electroluminescent devices. These materials are also fairly well removed in nature from traditional microelectronic silicon. This prevents the realization of the growth and processing advantages to be gained from using a silicon based material, making these materials an unattractive alternative.

1.5.4 Amorphous Silicon

Amorphous silicon shows different light emission behavior from that of bulk crystalline silicon due to the impact of alloying and structural disorder on the energy band structure. Typically, hydrogenated amorphous silicon (a-Si:H) contains 5 to 10 atomic percent hydrogen, which serves to tie up dangling bonds in the amorphous network and to expand the band gap of the material. Since the material is amorphous, the atomic arrangement does not have any long range periodicity. The standard energy band construction in bulk semiconductors, which determines the position of the energy levels as a function of k, the wave vector, which is related to particle momentum, develops out of the long range periodicity of the atomic positions. In a material lacking this long range order, the ideas of the E-k dispersion relations and momentum selection rules lose their meaning. These materials still have bands of allowed states separated by a gap of unallowed states which has a magnitude of 1.6-1.8 eV, as measured by optical absorption.[6] The disorder of the material broadens out the edges of these bands into Urbach tails which extend exponentially away from the traditional band edges. The band edge position is termed the mobility gap, which separates delocalized carriers in the bands from localized carriers existing in band tail states.

Emission intensity from bulk a-Si:H has been observed to increase with increasing hydrogen content.[7] The photoluminescence emission energy typically ranges from 0.93 to 1.5 eV and shifts to higher energy with increasing hydrogen content. The higher energy emissions are believe to originate from shallow states lying in the band tails, while the lower energy emissions are the result of recombination between deeper lying, more localized carriers.

Both hydrogenated and nonhydrogenated amorphous silicon (a-Si) have been used to fabricate superlattices that exhibit optical properties indicative of quantum confinement of carriers. Superlattices of a-Si:H/a-SiN$_x$:H have shown increased radiative efficiency and

increasing optical gap energy with decreasing layer thickness.[8] Superlattices of a-Si/SiO_2 have demonstrated efficient visible wavelength light emission that shifts to higher energy with decreasing layer thickness.[9]

1.5.5 Quantum Confined Silicon Nanostructures

Another approach to improving light emission efficiency and tuning emission wavelength by band gap variation in semiconductors, and in silicon in particular, is to use quantum confined structures.[10] In these materials, such as quantum wells, porous silicon, and silicon nanoparticles, the bulk silicon band structure is altered through the reduction of the volume in which electron and hole wavefunctions can exist. This confinement alters the positions of the energy levels and results in greater overlap of the electron and hole wavefunctions. The fundamentals of quantum confinement in semiconductors will be discussed in Section 1.6. The controversial properties of actual silicon nanostructures, including those fabricated from amorphous silicon, will be discussed in Section 1.8.

1.6 Quantum Confinement Effects in Semiconductors

Recall that the light emission deficiencies of bulk silicon were twofold: the emission wavelength was not visible and the emission efficiency was low. Quantum mechanics, which caused these problems in the first place, can alleviate them through quantum confinement effects.

1.6.1 Energy Gap Tunability

One of the most important requirements for fabricating displays based on luminescent semiconductor materials is the need for wavelength tunability in order to produce lifelike images. The displays must be in color, and in order to produce color images it is necessary to at least have light emitters capable of producing red, green, and blue light. In a given bulk semiconductor material, the nature of the material (the elemental species from which it is comprised and the way in which the atoms are arranged) determines the energy gap, and thus the emission wavelength. The gap can be tuned by varying the composition, but this

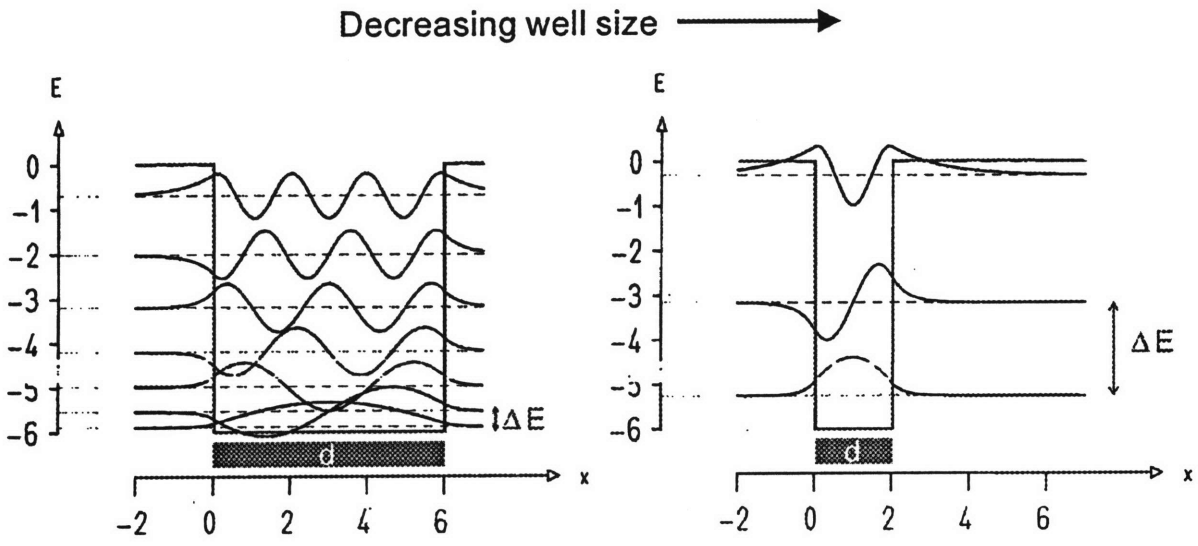

Figure 1-4: Schematic representation of the "particle in a box" problem. The particle wavefunction ψ is plotted for several different quantum levels in the well. Note the change in positions of energy levels as a function of well dimension. Figure generated using Reference [11].

is an unsuitable solution for making displays based entirely on silicon.

Another route that has been investigated for many compound semiconductor systems for tuning the emission wavelength is to capitalize on quantum confinement effects. Here, as the dimensionality is reduced, it is possible to reduce the emission wavelength of the material. The principle behind quantum confinement effects is simple, but one of the great challenges to materials science has been fabricating materials of sufficiently high quality that quantum confinements could be observed rather than being washed out by the impact of defects, impurities, and irregularities in materials fabrication. The impact of reducing the dimensionality of a system on its electronic properties can be visualized by considering the familiar "particle in a box" problem from quantum mechanics, as shown in Figure 1-4. This model consists of a potential energy well with an abrupt transition to a much higher potential energy region at the edges of the well. This roughly represents either a very thin layer of one semiconductor material sandwiched between two outer layers of a different material, or by extension to three dimensions, a small particle of material encapsulated by some different material.

As is true for any electron existing at any point in space, an electron placed within this well can be represented with a wavefunction, a mathematical construct that we arrive at by solving Schrödinger's equation. For the case where this electron exists in empty space, the electron is able to take on any energy values and the wavefunction will still be a solution to Schrödinger's equation. When the electron is placed within the potential well of Figure 1-4, however, some severe boundary conditions have been imposed on the electron, such as that it cannot exist outside of the well region, which results in a situation in which only specific, quantized energies result in wavefunctions that are solutions to Schrödinger's equation. In fact, as Figure 1-4 shows, as the size of the well is decreased, the positions of these levels changes and they become more widely spaced apart. The positions of the energy levels in an infinitely deep potential well are given by

$$E(d) = \frac{\mathbf{n}^2\pi^2\hbar^2}{2md^2}$$

where d is the width of the potential well and m is the carrier mass. This model can be extended to represent a quantum well, which is a thin slab of semiconductor material. Electrons existing in the potential well are electrons in the conduction band of the semiconductor, with the bottom of the well representing the conduction band edge. The same construction can be used to represent holes in the valence band. This model provides an expression for the variation of the energy spacing between the highest occupied and lowest unoccupied ground state levels in a quantum well as a function of size

$$E(d) = E_g + \frac{\pi^2\hbar^2}{2d^2}\left(\frac{1}{m_e} + \frac{1}{m_h}\right)$$

where E_g is the band gap of the material in bulk form, m_e is the electron mass, m_h is the hole mass, and d is once again the well width.

This simple model can be extended to a system confined in three dimensions in a spherically symmetric potential well, creating a structure known as a quantum dot. Once again, the energy gap is dependent upon the size of these dots. In this case,

$$E(r) = E_g + \frac{\hbar}{2r^2}\left(\frac{1}{m_e} + \frac{1}{m_h}\right) - \frac{1.8e^2}{\epsilon r}$$

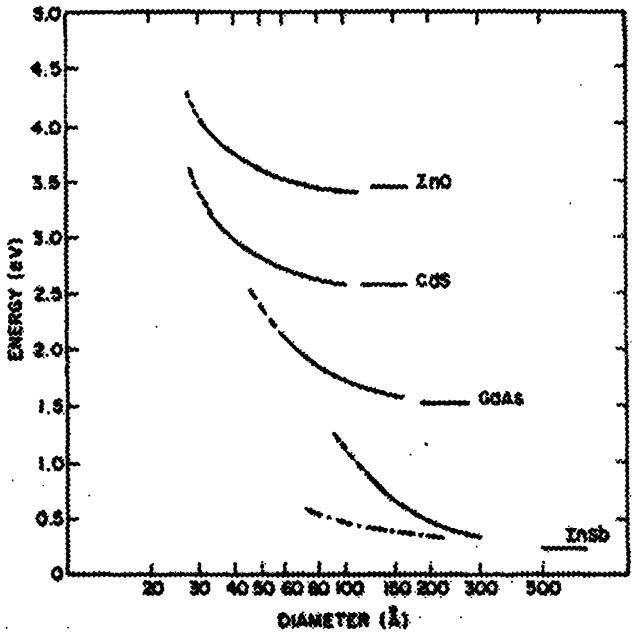

Figure 1-5: Variation of energy gap with particle size for several species of semiconductor nanoclusters. From reference [12].

where m_e and m_h are the effective masses of electrons and holes, r is the particle radius, and the third term represents a Coulombic attraction regulated by the dielectric constant (ε) of the system. For very small clusters, this term can become negligible and the energy varies inversely with the square of the particle radius.[12] The variation of the energy gap as a function of size computed by this technique for quantum dots of several semiconductor materials is shown in Figure 1-5. There is clearly a dramatic increase in the energy gap at reduced sizes in these quantum dots. Therefore silicon, which has a bulk band gap of 1.12 eV (in the infrared), can realize an increase in that energy into the visible portion of the spectrum by employing quantum confined silicon nanostructures.

In quantum confined materials, the exciton binding energy is expected to be greater than that in the bulk. This is a consequence of the fact that as the dimensions are decreased, the energy gap increases, which corresponds to a decrease in the dielectric constant. As shown in Section 1.4.1, a decrease in the dielectric constant will lead to an increase in the exciton binding energy. Thus, in a quantum confined structure excitons can survive thermalization

to higher temperatures than in the bulk. For silicon nanostructures, exciton binding energies are predicted to be on the order of 100 meV.[13] This is larger than the room temperature thermal energy of 26 meV, meaning that excitons can exist in quantum confined structures even up to room temperature. This opens up the possibilities for narrow emission lines and nonlinear optical effects.

The exciton radius can be used to estimate the size range necessary for quantum confinement. In order to start altering the behavior of an exciton, which is the point at which quantum confinement effects set in, it must be confined into a space with dimensions that are smaller than the exciton radius in the bulk. Following this reasoning, the onset of quantum confinement effects will occur for particles with radii in the size range of 4.3 nm for silicon, 11.5 nm for germanium, 5.4 nm for cadmium selenide, and 12.4 nm for gallium arsenide, as these are the exciton radii for those materials.[14]

This is a fairly simplistic model of the situation that exists in nanometer sized semiconductor particles. It assumes that the particles are spherical and that there is an abrupt change in the potential at the surface of the particle, which may not actually be the case. Additionally, this is a continuum model, but real particles are comprised of atoms. In considering bulk material, there are so many atoms that this kind of continuum theory is unaffected, but in nanometer scale particles the number of atoms is small. This results in a large surface to volume ratio, and the surfaces alter the periodicity that many calculations depend on. In short, while the particle in a box model is a good starting place, making quantum dots from real materials may introduce some deviations from simple theory. It may be possible to achieve a more accurate model of the energy gap dependence on size using a more sophisticated approach, such as the effective mass approximation [13], a linear combination of atomic orbitals [15], density functional theory [16], or a tight binding model.[17] Figure 1-6 depicts the variation of energy gap as a function of size as predicted by the linear combination of atomic orbitals method. These results are similar to those computed by most of the methods mentioned.

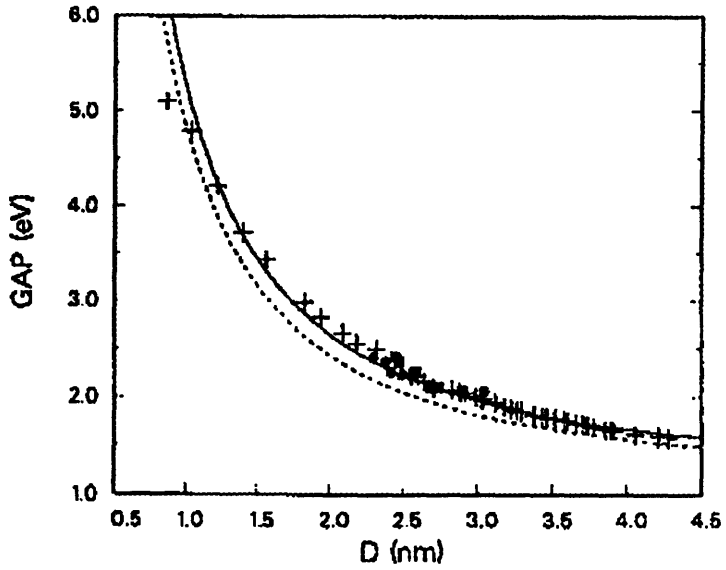

Figure 1-6: Size dependence of the energy gap in silicon nanoparticles as modeled using a linear combination of atomic orbitals approach. From Reference [18]

1.6.2 Increased Emission Efficiency

For any silicon based material that can emit light in the proper portion of the electromagnetic spectrum there is another issue to consider: is there enough light coming from the material to make useful devices? For bulk silicon, the momentum selection rules dictate that radiative transitions across the indirect energy gap are unlikely, resulting in insufficiently intense emission. Luckily, quantum confinement has also been found to increase the light emission efficiency of semiconductors.[19]

This can be understood by applying two models. Phenomenologically, as the volume of material in which electron hole pairs exist is reduced, the degree to which the wavefunctions representing these particles overlap must increase. As the wavefunction overlap increases, so too does the probability that the particles will recombine. By increasing the recombination probability, the emission efficiency is likewise increased.

A somewhat more rigorous approach to explaining the enhanced emission efficiency of semiconductor nanostructures follows along the lines of the discussion of impurity luminescence from silicon. Once again, the Heisenberg uncertainty principle dictates that the

momentum and position of a particle cannot both be known to infinite precision. As before, it is possible to capitalize on reducing the uncertainty in position to "smear out" the momentum of a particle. Here, the electron and hole generated by a photoexcitation event are localized within the volume of the semiconductor quantum dot. These dots are very small, less than 10 nm in diameter, which means that the carrier pairs confined to them are located in a very small region of space. There is very little uncertainty in the position of the particles, which dictates that there is uncertainty in the momentum. This momentum uncertainty is large enough to relax the momentum selection rules and make radiative transitions more likely to occur even in quantum dots of materials that have an indirect band gap in bulk form.

1.6.3 Discrete Density of States

Quantum confinement alters the positions of energy levels and changes the nature of transitions between those levels. One other question that remains to be answered is how many states exist at a particular energy. This is typically thought of in terms of the density of states as a function of energy

$$g(E) = \frac{dN}{dE}$$

where N is the number of allowed states at energy level E. In bulk semiconductors, the density of states has a parabolic form, with an ever increasing number of available states lying at higher energies. The derivation of the functional form of the density of states can be used to determine what it is for a quantum confined semiconductor.

In the case of a free electron, which can be represented by a wave as shown by deBroglie, the energy of the particle can take on any value, so that

$$E = \frac{\hbar^2 \mathbf{k}^2}{2m}$$

where m is the electron mass and $\mathbf{k}$ is the wave vector of the electron (related to the it's momentum). When this electron is placed into piece of material, say a semiconductor, only certain values of $\mathbf{k}$ (and therefore E) are allowed. This results from the requirement that the

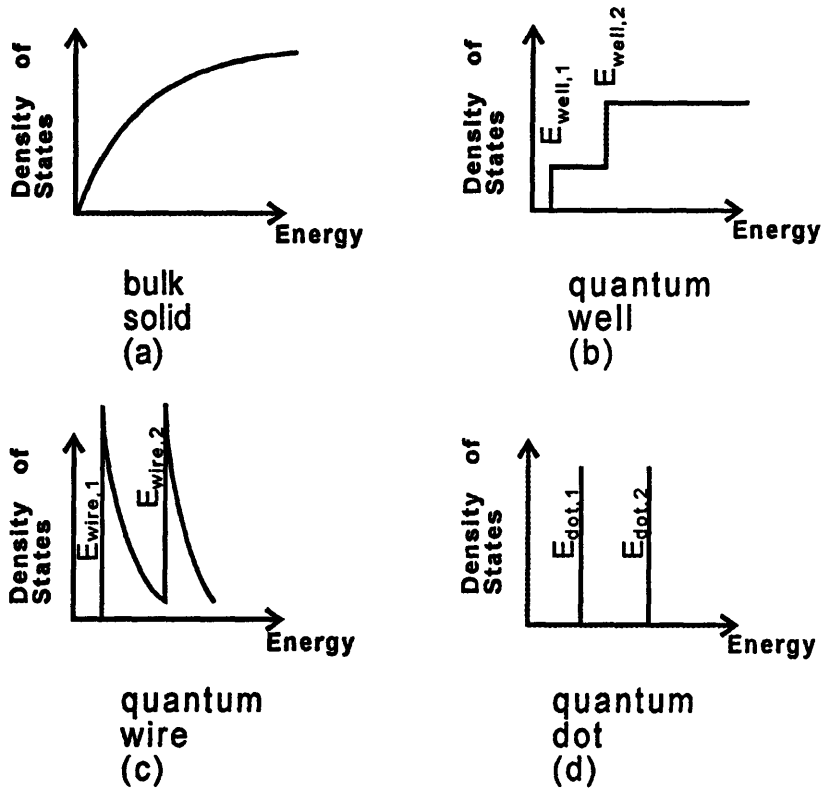

Figure 1-7: Density of electronic states as a function of energy for (a) a bulk semiconductor, (b) a quantum well, (c) a quantum wire, and (d) a quantum dot.

electron obey Schrödinger's equation and the boundary conditions imposed on the solutions to this equation (the electron wavefunction) by the physical limits of the piece of the material. In the case of a macroscopic amount of material, the density of states is given by

$$g(E) = \frac{(2m)^{3/2}}{2\pi^2\hbar^3}\sqrt{E}$$

an expression which includes no dependence on the dimensions of the piece of material, which are "washed out" in the calculation. This function represents a continuous range of allowable states, as shown in Figure 1-7 a.

As the dimensionality of the system is reduced, first making one dimension small (a quantum well), then two (a quantum wire), and finally three (a quantum dot), this continuous range of allowed states begins to change and become dependent on the magnitude of the

small dimension. For a quantum well of thickness d the density of states is given by

$$g(E) = \frac{m}{\pi\hbar^2 d}$$

which represents a step function defined at each allowed energy level for the quantum confined dimension, as shown in Figure 1-7 b. For a quantum wire of rectangular cross-section with dimensions d_1 and d_2, the expression for the density of states is

$$g(E) = \frac{\left(\frac{1}{d_1 d_2}\right)\left(\frac{\sqrt{m}}{\sqrt{2\pi\hbar}}\right)}{\sqrt{E}}$$

which is plotted in Figure 1-7 c. Finally, in a quantum dot the density of states reduces to a series of delta functions of finite height, as shown in Figure 1-7 d. This discrete density of states of a quantum dot is very similar to a molecular system and has often earned them the moniker of "artificial atoms," in that the energy bands that are characteristic of a bulk semiconductor have been completely lost. Recalling that for band to band recombination, the width of the emission spectrum is determined by the density of states, it is evident that one of the advantages of quantum dots should be the potential for very narrow emission linewidths.

There are two important things to note regarding this determination of the density of states of a quantum dot. First, the delta function like density of states is an ideal representation of the quantum dot. Real semiconductor nanoparticle systems made from real materials will exhibit some deviations from this behavior, such as a broadening of the spikes in energy. This results from the detailed surface structure of the particles and variations in particle size within an ensemble of particles. Second, the delta functions in the density of states of a quantum dot are not infinite in height. The total number of allowed states is dictated by the number of atoms in the particle, since these states have their origins in the electronic states of the constituent atoms. If a sufficiently large number of electrons were promoted to a higher level in a quantum dot, it would be possible to completely fill the lowest energy level. This important mechanism in quantum dots is known as state filling, and some of its ramifications for the optical properties are discussed in Section 1.6.4.

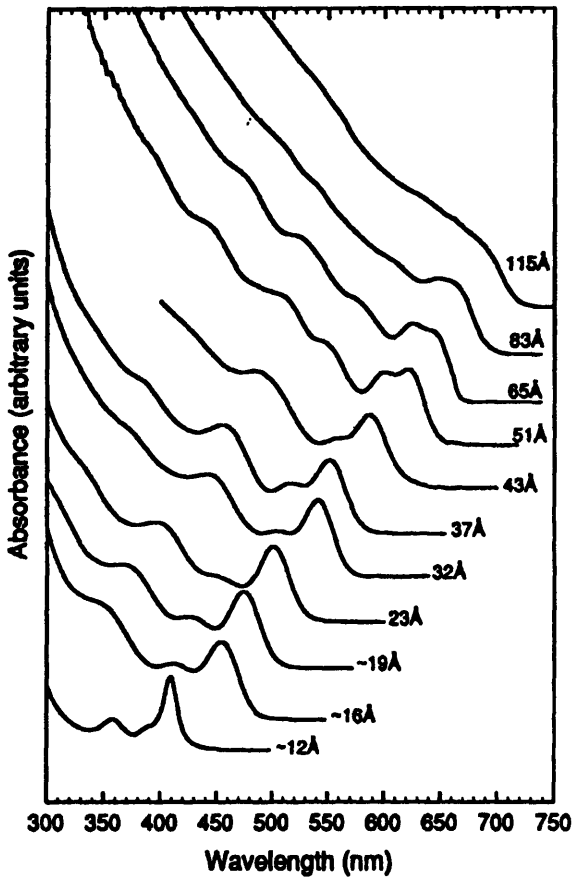

Figure 1-8: Room temperature optical absorption spectra for CdSe nanoparticles of varying size dispersed in hexane. Note the shift of the absorption edge as a function of size and the finite height of the first absorption peak. From Reference [20].

1.6.4 Implications for Optical Properties

The modifications of semiconductor properties enumerated above have several consequences for the photoluminescence emission behavior. The increase in the energy gap between highest occupied and lowest unoccupied states with decreasing particle size will result in a shift in the absorption edge toward higher energy as particle size is reduced. This is evident in the absorption spectra of CdSe quantum dots shown in Figure 1-8. This will also result in a shift of the emission to higher energy with reduction of size, such as that observed in InGaAs quantum wells.[21] Similar trends observed for silicon would shift the bulk infrared emission into the visible portion of the spectrum, and the emission should be tunable throughout the

visible wavelengths by changing particle size. The increase in emission efficiency for quantum confined structures means that not only will the emission be shifted in energy, but there will also be more of it, making it possible to fabricate useful devices since the luminescence will be bright enough to be seen by the human eye. [22]

The finite density of states has ramifications for both the absorption behavior and the photoluminescence emission of quantum confined materials. As is evident in the absorption spectra shown in Figure 1-8, the discrete levels lead to narrow absorption peaks of finite height. This means that it is possible to saturate the absorption of the quantum dots, since any light intensity above that represented by the height of the absorption peak cannot be absorbed and will simply be transmitted. The absorption saturation also effects the photoluminescence spectra of quantum confined materials. Typically, this luminescence is excited by high energy photons, such as ultraviolet light. These photons excite carriers into higher energy states which subsequently find their way to the lowest state that is unoccupied in the ground state of the quantum dot. In the bulk, these carriers would be making their way to the conduction band edge via thermalization. From this lowest level, the electrons undergo a radiative recombination event. Under sufficiently high excitation intensity, it is possible to promote more electrons than can be accommodated in the lowest unoccupied ground level of the quantum dot. These carriers will take up residence in higher levels, from which they can de-excite via radiative recombination events. Since the carriers are recombining from higher energy levels, the light they emit is of higher energy, or shifted to the blue. As a consequence of the filling of this discrete density of states, under high intensity photoexcitation quantum confined materials will exhibit a blue shifting of the photoluminescence emission spectrum.[23]

1.7 Synthesis and Properties of Semiconductor Nanostructures

The theory of quantum confinement effects is a very elegant one, but it is also of importance to ask if it is actually possible to fabricate quantum confined structures. The answer is yes. Quantum wells, quantum wires, and quantum dots have all been synthesized with varying

degrees of success. Given that the dimensions of these structures lie in the nanometer size range, they are generally referred to as semiconductor nanostructures. It is of interest to examine the various techniques used to synthesize the quantum well and quantum dot varieties of semiconductor nanostructures.

1.7.1 Quantum Wells

The first quantum confined semiconductor structures studied were quantum wells. The need for confinement in only one dimension means that very thin films of material clad on both sides by a material of different energy gap will exhibit quantum well behavior. To grow quantum wells, it is necessary to synthesize very uniform, pure films of controlled thickness that could be lattice matched to cladding layers. Lattice matching between the quantum well layer and its neighbors is necessary to eliminate any structural defects that might introduce nonradiative recombination pathways and mask the quantum confinement effects. Advances in materials engineering have led to the development of synthesis techniques for making quantum wells.

Quantum wells were first grown from GaAs clad with AlGaAs using molecular beam epitaxy (MBE) in 1974.[24] These structures exhibited absorption spectra having the step like profiles predicted by theory, with the energy of the steps being size dependent. In the intervening years, many other compound semiconductor materials from the II-VI and III-V families have used to fabricate quantum wells. These materials have been synthesized using the MBE technique developed for this purpose, as well as improved chemical vapor deposition processes. Quantum well devices have become commonplace, even appearing in consumer electronics such as compact disc players. These devices still have one major drawback, though: they are not integrable with silicon microelectronics.

More recently, effort has gone into developing a fabrication technique to grow silicon/silicon germanium heterostructures, in which the SiGe layers serve as quantum wells clad by the Si. These materials have been grown by MBE [25] and CVD.[26] Like the II-VI and III-V compound quantum well materials, the SiGe alloy heterostructures exhibit size dependent optical properties. This advance is promising for the fabrication of silicon-integrated opto-electronics for optical interconnects. Unfortunately, the band gap energy of SiGe alloys is

even smaller than that of silicon, making these materials of unsuited for display applications.

An important advance in the quest for light emitting silicon useful for displays has been the fabrication of silicon quantum wells and quantum well heterostructures. These materials have been grown using a number of processing techniques. Attempts have been made to produce a-Si:H/a-SiN$_x$:H heterostructures, but these have generally produced silicon layers containing nanometer sized particles, rather than uniform silicon layers, and they will not considered here in a discussion of quantum wells.[8] A more successful approach has been to grow Si/SiO_2 heterostructures, with some researchers experimenting with amorphous silicon layers while others have grown crystalline films. These heterostructures have been produced by oxidation of the surface layer of SIMOX wafers (wafers with a surface silicon layer and a buried oxide region).[27] Amorphous silicon/oxide heterostructures have been fabricated via MBE growth of silicon on UV/ozone grown oxide layers [9, 28, 29] and magnetron sputtering.[30] In all cases, visible luminescence is observed from the silicon nanostructures. Some of the researchers report on shifts of the luminescence wavelength with changes in the thickness of the silicon layer, which would indicate quantum confinement based luminescence. The growth mechanisms for fabrication of the cladding layers are not as sophisticated as those used for the compound semiconductor quantum wells, so up to this point the performance of the silicon quantum wells is below that for those commercially available materials.

1.7.2 Quantum Dots: Chemical Synthesis Techniques

Quantum dot growth technology is somewhat further back on the learning curve than compound semiconductor quantum well technology. The most advanced of the dot growth techniques is the chemical synthesis techniques used to grow some II-VI and III-V semiconductor nanoparticles. This approach employs the chemical reaction of organometallic reagents to form compound semiconductor particles. The original work involved using an inverse micelle method to grow CdSe and CdS particles capped with organic capping groups.[31] The particles are formed as molecules from solution attach themselves to the nucleation sites. This reaction requires the application of heat, so the removal of this heat results in arrested precipitation of these particles, which have a fairly uniform size distribution. In an extension of

this work, Murray has developed a technique for size selective precipitation of these clusters, to narrow the size distribution even further.[20] Quantum dot samples of CdSe have been found to have extremely monodisperse size distributions, to a level of <5%. This uniformity produces very clear optical features that would be expected from the narrow resonances predicted for quantum dots, as can be seen in Figure 1-8. This technique has been extended to work in CdTe and CdS in the II-VI family [20], and to GaAs [32], InP [33], GaP, and $GaInP_2$ [34] in the III-V family.

Structural issues

An interesting, and potentially troubling, problem arises when fabricating these small particles. Depending on the processing conditions, nanocrystallites with both wurtzite and zincblende structures have been produced, and it seems that this structural change is dependent on the particle size. For example, in the CdS nanoparticle system, 4 nm particles have been synthesized having the zincblende structure, while 2.1 nm particles have been observed to have the rock salt structure.[35] CdS and CdSe particles 3 nm in size have been synthesized with a cubic structure, which can be converted to the bulk hexagonal structure with annealing, indicating either a metastable structure at low size or a strong correlation between the particle size, surface, and structure.[36] CdSe particles have been observed to undergo a transition from the wurtzite to rock salt structure under high pressure, with the required applied pressure increasing with decreasing particle size, indicating a strong link between particle size and structure.[37]

The origin of the structural instability lies in the large surface to volume ratio of the small particles as well as their finite size. As the pieces of material become smaller, more and more of the atoms are located on the surface. By changing the arrangement of the atoms in the particles, it is possible to reduce the number of surface atoms and the number of unsatisfied bonds that these atoms have. The structural transition results in a reduction of energy, and is thus thermodynamically favorable and will occur if the opportunity presents itself. Problems may arise from differences in the electronic properties of the same material having different structures, since the electronic properties arise partially from the ordering of the atoms.[38]

Similar structural instabilities have been observed for germanium and silicon, indicating that elemental as well as compound semiconductors are susceptible. Germanium films grown using a cluster beam evaporation technique have been found to have a tetragonal structure, not the bulk diamond structure.[39] Ge microcrystallites grown by plasma enhanced chemical vapor deposition (PECVD) have been identified which have a new structure unrelated to the bulk diamond atomic arrangement.[40] Perhaps of even more concern is the situation observed for silicon. Microcrystalline silicon films can be deposited by PECVD and by controlling the deposition conditions it is possible to vary the crystallite size. For growth conditions designed to produce crystallites of less than 3 nm, the material produced is not crystalline but amorphous. It has been suggested that this transition is due to the increased surface to volume ratio of the crystallites and is thus size dependent.[41] A pressure induced transformation along the lines of that reported for CdSe particles has also been observed for silicon. Crystalline silicon nanoparticles exposed to high pressure undergo a transformation to amorphous silicon.[42] This is unlike the transition for bulk silicon, which takes on a BC8 structure under applied pressure. These results suggest that amorphous phases and disorder are likely to be important in the consideration of small silicon particles, as will be shown in Section 1.7.5.

1.7.3 Compound Semiconductor Quantum Dots: Other Growth Methods

Compound semiconductor quantum dots can be produced using the MBE and CVD techniques developed for quantum wells. During the development of the quantum well growth techniques, materials researchers discovered that the very thin films did not always grow uniformly. Often, the material coalesced into small islands which then grew together to form thin films. Recently, researchers have realized that if they stop growth during the initial islanding state and then cap the particles with another layer for confinement and passivation, they can produce quantum dots. This approach has been used to grow numerous species of quantum dots, such as InGaAs/GaAs [43], InAs [44], InP [45], and GaInP.[46] Usually, materials are chosen which have a large exciton radius, so that the islands can be larger while still forming quantum confined systems. These materials have shown evidence of quantum confinement, with luminescence wavelength shifting with island size. Another

vestige of quantum confinement observed in these materials is state filling at high excitation intensities, wherein luminescence begins to emerge from higher excited states when a high energy, high intensity excitation source is used.

Other approaches for producing nanoparticles of compound semiconductors include the production of GaAs by the exploding wire method [47], electrochemical anodization of GaP to produce porous GaP [48], and the growth of CdS, CdSe [49], InP [50], CuCl, and CuBr [51] nanoparticles in porous glass. Optical properties attributed to quantum confinement have been observed in most of these systems, but the growth techniques are not as well refined or integrable as the chemical synthesis or MBE approaches.

1.7.4 Porous Silicon

Much of the current interest silicon nanostructures as a materials system to be used to address the need for silicon based light emitting materials was inspired by the discovery of efficient visible photoluminescence from porous silicon in 1990.[52] Porous silicon is formed by the etching of crystalline silicon wafers using a dilute solution containing hydrofluoric acid (HF). The typical approach uses an anodic etch,[53] but it is possible to fabricate porous silicon using a stain etch technique in which an HF/HNO_3 solution is simply exposed to the wafer surface.[54] In the anodic etching process, the bulk wafer begins to dissolve under anodic bias through the removal of silicon atoms upon reaction with HF and holes, as represented in the chemical reaction

$$\mathrm{Si} + 4\mathrm{HF} + (4-n)h^{+} \rightarrow \mathrm{Si\,F_4} + 4\mathrm{H}^{+} + ne^{-}$$

where h^+ represents holes and e^- represents electrons. The requirement of a hole supply to carry this reaction out means that p^+ doped wafers are usually used to make porous silicon and the need for charge transfer suggests why the anodic etching technique is far more efficient than the stain etch for producing porous silicon. It is possible to use low level p-type wafers or even n-type silicon as the source material by employing some external hole source such as illumination. Current densities for the formation etch are in the 1-30 mA/cm^2 range. A variety of electrolytes have been employed, including 25% HF,[55] HF:Ethanol,[111]

HF:Ammonium Fluoride,[57] and HF:Methanol:Water.[58]

The exact mechanism by which a pore structure forms in the silicon due to this etch is subject to some debate. The most widely accepted theory proposes that portions of the wafer surface are selectively etched because of the presence or absence of positive charge carriers in those regions of the wafer. Once the etching process has begun, some areas of the wafer will become constricted in size. One model posits that these constricted areas will have a larger band gap than the bulk due to quantum confinement, and that the energetics exclude holes from these regions.[59] The holes then travel to the unetched regions alongside the constrictions and continue the etching process, resulting in an ever magnifying preferential etching that produces long constricted wires of residual silicon. Another model proposes that a space charge layer exists at the wafer surface, which enhances the tunneling of holes to the bases of the pores, increasing the etch rate at those sites.[60]

The formation process results in a complex sponge of interconnecting layers of silicon nanostructures. Freshly prepared porous silicon films have been found to have hydrogen passivated surfaces, as one would expect for a material formed using HF. As films are exposed to air, the hydride layer is replaced by a surface oxide. Characterization by transmission electron microscopy (TEM) and scanning electron microscopy (SEM) has found that layer thickness can be up to hundreds of microns, consisting of crystalline silicon regions mixed with pores.[61] The pore size has been measured to range from $\sim$100 nm in macroporous material to $<$2 nm in mesoporous material. The silicon that remains has been described as an array of quantum wires or quantum dots comprised of crystalline or amorphous silicon, with some features lying within the size where quantum confinement effects would be expected. These features exist in a broad array of sizes, which makes it difficult to correlate the observed optical properties to a particular size of silicon nanoparticle. Also, the microstructural features are highly dependent on the formation conditions, initial material, and post-fabrication processing, resulting in many conflicting reports from different researchers and making it difficult to draw conclusions from the body of data.

Another issue related to the inconsistency of porous silicon materials involves the doping levels required to achieve efficient etching. Depending on the desired etching conditions, doping levels up to 10^{18} cm^{-3} have been used.[52, 62, 63] At this doping level, if the silicon

wafer is etched into particles containing 1000 atoms, each particle would on average contain one dopant atom. This dopant could dramatically change the electronic properties of the particle in which it is enclosed. The dopant issue has been largely ignored in the porous silicon community, but it could be the source of much of the variability of the data.

1.7.5 Silicon Clusters

Silicon clusters have been produced using a number of techniques and the materials formed have very different microstructural characteristics. Some of the earliest studies of silicon particles were performed on clusters formed by gas evaporation techniques.[64] Silicon source material was heated, evaporating silicon atoms from the surface. These atoms came together to form clusters and were collected on substrates. In general, the particles synthesized by this technique that have been studied are up to 200 nm in diameter, which would be too large for them to exhibit quantum confinement effects. The characterization of these particles has focused on their structure, with TEM the most widely used technique. These larger silicon particles have been found to have a multiply twinned structure, wherein they consist of several regions of the same structure in different orientations, which come together at twin boundaries.[65] This microstructure is believed to minimize the surface energy of the particles.[66] These particles have also been seen to be dynamic in structure, with the twin boundaries moving over time, which is believed to be induced by the energy provided by the electron beam in the microscope.[67] Raman spectroscopy of these particles reveals evidence for the presence of crystalline silicon in the larger particles, upwards of 50 nm in diameter. Smaller particles in the 12 nm diameter range show spectral signatures more similar to amorphous silicon than crystalline silicon. This has been attributed to a strong contribution to the signal from the surface regions.[68] These observations of evidence for non-bulk structure in silicon clusters are consistent with the observation of non-bulk structure in Ge clusters.[40] While particles are too large to exhibit quantum confined photoluminescence, they do suggest that structural instability or phase changes may be present in small silicon systems and may play a role in any luminescence that might be achieved.

Another approach to studying silicon particles is to consider very small particles, rather than the "large" ones gas evaporation produced. These particles consist of only a very small

number of atoms, less than 100, and might not be expected to have bulk structures at all. Particles in this size range have been studied both experimentally and theoretically. In order to study small clusters of metal atoms, the group of Smalley developed a pulsed laser ablation supersonic expansion cluster source.[69] With some modification, this became the source of choice for studying small silicon clusters.[70] Numerous researchers have studied clusters from 1 to 70 atoms produced using pulsed laser ablation supersonic expansion.[71, 72, 73] These clusters have been studied both in the gas phase and when collected onto substrates. Vibrational spectroscopic measurements made on silicon clusters of less than 10 atoms isolated in a frozen inert gas matrix reveal that these clusters do not have bulk silicon-like arrangements of the constituent atoms.[74] It was also observed that these clusters, if allowed to agglomerate, would form amorphous silicon.[75] Larger clusters in the 20-30 atom size range have been found to undergo a size dependent morphological change. By passing clusters through a time of flight gas collision chamber (drift tube), it was shown that at a certain size, clusters exhibited a change in cross section for collisions with gas atoms that was not commensurate with the slight change in size. Rather, the morphology was changing from more elliptical to more spherical as cluster size grew.[76] Studies of clusters from this size up to 70 atoms reveal indirect evidence for size independent absorption, which suggests that these disordered particles don't show quantum confinement effects.[77]

The structural observations about small particles are confirmed by theoretical modeling. For studying the smallest of particles, less than 10 atoms, it is possible to use accurate *ab initio* molecular orbital calculations to determine the equilibrium structures.[78] In order to reduce the number of unsatisfied bonds in a cluster, it was found that the atoms rearrange and pack more densely, thereby reducing their energy and becoming more stable.[79] Ball and stick representations of these atomic arrangements are shown in Figure 1-9. The vibrational modes occurring in the calculated structures for clusters of less than 7 atoms can be compared to those measured for actual clusters synthesized by laser ablation, and experiments have confirmed that the clusters have the predicted structures.[81]

Larger clusters have proven more difficult to model, due to the prohibitive size of the *ab initio* calculations when more than 10 atoms are considered. Differing approximations have been chosen to address larger clusters, but these produce different results. Density

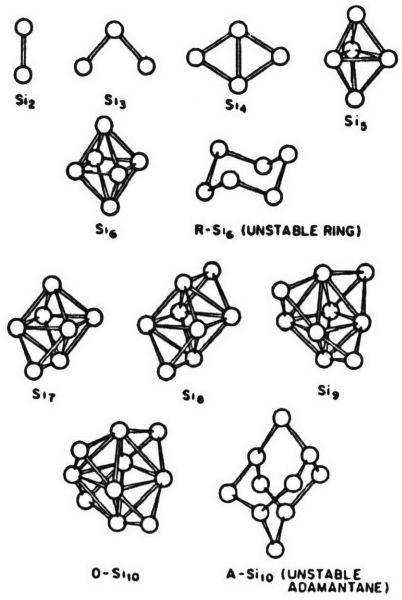

Figure 1-9: Ball and stick models of the clusers Si_1-Si_{10} demonstrating the non-bulk arrangements of the constituent atoms. From Referrence [80].

functional theory using the local density approximation produces results consistent with the *ab initio* calculations for particles of less than 10 atoms [82] and predicts non-bulk like structures for clusters of 20 and 21 atoms, as shown in Figure 1-10.[83] A combined tight binding density functional scheme predicts that all equilibrium cluster structures are close packed, with a transition to bulk-like open structures occurring at cluster sizes of 100 to 1000 atoms.[80] A generalized valence bond approach arrives at geometries based on a 17 atom bulk-like core with the remaining atoms creating a surface resembling reconstructed bulk silicon surfaces.[84] Modeling of several alternative structures using a semiempirical SINDO1 method reveals that particles with less than 13 atoms prefer to be noncrystalline, a face centered cubic structure is preferable to diamond in particles with 19-34 atoms, and above 35 atoms the diamond structure is preferred to hexagonal close packed.[85] This also finds that more close packed structures are preferred to hollow, fullerenic geometries.[86] In contrast, a stuffed fullerene model has been used to predict hollow geometries (atoms are mostly located on the surface of the cluster) which are stable, as shown in Figure 1-11.[87] The pseudopotential based Car-Parrinello technique predicts that mid-size clusters consist

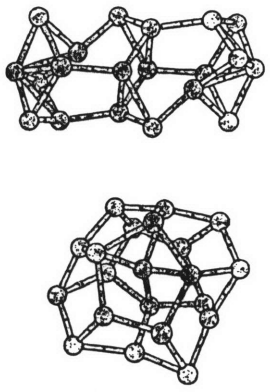

Figure 1-10: Ball and stick models of the lowest energy geometries for Si_{20} and Si_{21} as determined by a density functional theory/local density approximation approach. From Reference [83].

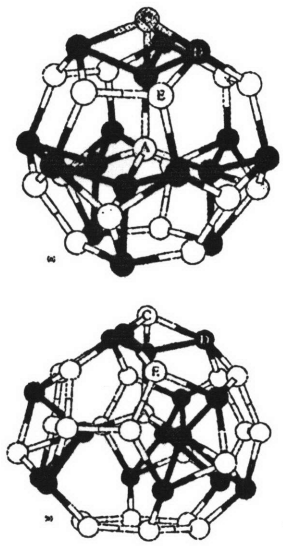

Figure 1-11: Structures of (a) Si_{33} and (b) Si_{39} obtained using the stuffed fullerene model. From Reference [87]

of two shells of atoms, an outer fullerene-like cage and an inner shell of a few atoms tying up dangling bonds.[88] First principles total energy calculations predict elongated structures, with more bulk-like silicon bonding, at smaller sizes, with a transition to more spherical fullerenic type structure at larger sizes.[89] It is clear that there is no consensus regarding the atomic arrangements in silicon clusters. The calculations suggest that small silicon clusters might take on just about any structure, which must always be taken into account.

One other approach to silicon particles has tried to address the intermediate sizes between the gas evaporated particles and the clusters previously studied by laser ablation. This involves the breakdown of silicon gases to form clusters. Researchers at Bell Laboratories have generated silicon nanocrystallite colloids by a high temperature aerosol process and subsequent bubbling through ethylene glycol. Oxidized silicon nanoparticles are formed by the pyrolysis of disilane in a high pressure flow of helium, with a subsequent oxidation in O_2. This process produces particles of many sizes, in the range of 1.5 to 4 nm, which have been separated somewhat using size exclusion chromatography and size selective precipitation.[90] These particles have been observed to emit visible light under photoexcitation. Electron microscopy shows crystalline particles whose size varies depending on the processing. Extended x-ray absorption fine structure (EXAFS) results confirm that crystalline silicon exists, although they also provide evidence for some degree of disorder. The wavelength of the emission shifts depending on the particle size, suggesting that quantum confinement plays a role in the luminescence.[91]

Several other approaches to fabricating silicon nanoparticles in this size range have been tried, including spark ablation [92], chemical synthesis techniques that are not as well developed as those for CdSe [93], laser breakdown of disilane [94], and plasma enhanced chemical vapor deposition.[95] Materials built up of these nanoparticles have all exhibited efficient visible photoluminescence, which makes them candidates for silicon based optoelectronic materials.

1.8 Light Emission from Nanostructured Silicon Materials

Efficient, visible photoluminescence has been observed from porous silicon, amorphous and crystalline silicon quantum wells, and silicon nanoparticles. The visible emission has been centered around two major luminescence bands: a blue band lying between 2.5 and 2.8 eV, and a red band lying between 1.2 and 2.2 eV. In general, the blue band has been found to have a fast decay time and is strong in materials that have been oxidized. The red band emission has been observed to have temperature dependent emission energy, intensity, and decay time.[96] A closer look at the data shows that within these general trends, the measured emissions have shown considerable variety of intensity, lifetime, and temperature dependence, especially as a function of materials processing. This has led to considerable debate as to the identity of the luminescing species and luminescence mechanism. Much evidence exists to support and refute several different proposed models, and while some of the more "fringe" theories have been discounted and are not discussed here, no clear and final consensus has been reached. The four major theories that still persist are:

1. Emission from recombination through defects in the oxide layer or at the silicon/oxide interface,
2. Emission from amorphous silicon regions in the materials,
3. Emission from band to band like recombination in quantum confined nanostructures,
4. Emission from quantum confined nanostructures through intermediate "surface states," also called a smart quantum confinement model.

1.8.1 Oxide theories

The oxide layer at the surface of porous silicon and silicon nanoparticles has been proposed as the source for the blue band emission. This emission appears to increase in intensity with oxidation of the nanostructures and correlates with increases in the intensity of Si-O related infrared absorption signal.[58, 97] This behavior is consistent with observations of visible photoluminescence from silicon dioxide.[98] Additionally, the fact that the blue band emission has been found to have a very short luminescence lifetime, in the nanosecond range, and is insensitive to oxidation steps designed to reduce the average crystallite size point to an

oxide related luminescence.[99] Some researchers argue, however, that the blue band emission actually originates from quantum confined semiconductor nanostructures. Some researchers argue that these same fast lifetimes are a result of direct recombination within the silicon cores, as opposed to the slower recombination through oxide surface states that are claimed to be responsible for the red band emission.[100]

Oxide interface states and related defects have also been targeted as the origin of the red band luminescence. Calculations have shown that an oxygen terminated silicon sheet, which would be similar to the surface of porous silicon or silicon nanoparticles, would show direct gap behavior and emit at 1.7 eV.[101] The temporal dependence of the luminescence has also been pointed to as evidence for defect emission. The slower, nonexponential decay of the red band PL suggests that this might be due to carriers tunnelling from silicon cores into defects in the oxide and recombining there.[102] Electron spin resonance (ESR) experiments point to the presence of active oxygen-centric defects which correlate with photoluminescence intensity. These non-bridging oxygen hole centers (NBOHCs) are known to emit light in the red portion of the spectrum and have been observed to shift in emission wavelength in the presence of hydrogen.[103]

Other evidence discounts the role of oxide defects in the photoluminescence emission. Porous silicon after formation is mainly hydrogen passivated, with no oxide on the surface, and yet this material exhibits strong luminescence. The NBOHC theory is inconsistent with a number of observations about porous silicon, most notably in that it cannot account for all of the luminescence wavelengths that have been observed from porous silicon and that resonantly excited photoluminescence shows evidence of phonon assisted transitions, which are not expected for oxide luminescence.[104] Finally, the oxide theory is inconsistent with observations that the luminescence peak can be shifted by changing the mean particle size.[105]

1.8.2 Amorphous or Disordered Silicon

Amorphous silicon has long been known to efficiently emit visible light. There is some evidence from structural characterization that disordered regions exist within the network that makes up porous silicon.[106] The nonexponential decay of the red luminescence band in

porous silicon is reminiscent of that observed from amorphous silicon, suggesting that these amorphous regions might give rise to the luminescence.[107] Recently, quantum wells comprised of multilayers of thin amorphous silicon layers clad with silicon dioxide have been fabricated which show wavelength tunable emission, where the decreasing well thickness leads to a blue shift of the photoluminescence emission spectrum.[9] EXAFS studies of porous silicon and silicon nanoparticles have revealed evidence of both crystalline and disordered material in visibly emitting systems. Heat treatments designed to drive off all of the hydrogen from porous silicon have not destroyed the luminescence, indicating that hydrogenated amorphous silicon is not giving rise to the luminescence.[91] The evidence suggests that while quantum confinement seems to be active, it may work in concert with amorphous silicon.

It is quite reasonable to expect that materials synthesized by techniques that build up silicon nanoparticles from single atoms would have very small clusters with non-bulk crystal structure present within them, and that perhaps these small particles provide the necessary combination of disorder and quantum confinement effects to be producing luminescence similar to that seen from amorphous silicon quantum wells.

1.8.3 Quantum Confinement Model

In Section 1.6, it was demonstrated that quantum confined silicon nanoparticles could be expected to exhibit efficient visible photoluminescence. Many researchers have attributed the observed behavior to this simple, expected mechanism. The quantum confinement model is supported by evidence that the photoluminescence emission of porous silicon can be shifted in wavelength through a variety of chemical processing steps.[109] There is also a body of work correlating the size of silicon nanoparticles with the luminescence emission wavelength.[110] TEM and SEM characterization have shown evidence of features that fall within the size range expected for quantum confinement effects in silicon.[61] A strict quantum confinement model is supported by resonantly excited photoluminescence measurements, which exhibit phonon replicas that suggest that the luminescence transition is occurring in the cores of silicon nanoparticles.[104, 105]

While there is much evidence to support the quantum confinement model, its detractors point to the fact that it has been difficult to fit the size dependence of emission wavelength

data to a simple model of quantum confinement. While some of the possible reasons for deviation from this theory were noted in Section 1.6, the disagreement raises some doubt. Additionally, some porous silicon researchers have observed a red shift of the luminescence upon treatments that should reduce particle size, which is in direct conflict with quantum confinement.[111] Some of the other properties of the luminescence, namely the nonexponential decay of the red band emission, the anomalous temperature dependences of the emission observed by some researchers [112], and the wavelength dependent lifetime point to a more complex luminescence mechanism.

1.8.4 Smart Quantum Confinement/Surface State Model

A modification of the quantum confinement theory has been proposed to explain the differences between expected and actual results. This is often termed either the surface state model or the "smart quantum confinement" model.[108] This model also postulates that quantum confinement effects control the positions of the allowed energy levels, but additionally introduces the concept of an intermediate state, usually associated somehow with the surface of the nanoparticle, through which carrier recombination occurs. In this system, the blue emission band reflects excitonic emission from the core of the silicon particles, while the lower energy red emission arises from recombination through the surface states. In many ways this model appears to be similar to the oxide defect model, with carriers generated in silicon particles moving to localized states at the surface, with the exception that the surface states postulated here are believed to be intrinsic to the semiconductor quantum dot and not extrinsic features like defects in an oxide coating. The advantage of the smart quantum confinement model is that it can explain both luminescence bands as being related to the silicon cores of the nanoparticles. The same size dependent emission results that support the strict quantum confinement model also bolster the surface state model. Its weakness lies in evidence that the intensity of the blue emission increases with increasing oxide content (as determined by infrared absorption), since this model attributes the blue emission to the silicon cores, the concentration of which does not increase with increasing oxidation.[113] Also, the photoluminescence emission of both oxide and hydride passivated silicon nanostructures has been shown to exhibit similar properties, such as the emission lifetime and presence

of phonon replicas, which would indicate that the nature of the surface passivating species does not alter the luminescence.[105] Since this theory depends strongly on the nature of the particle surface, it would be expected that surface modifications would lead to changes in the photoluminescence.

1.9 Statement of Thesis

It is clear that silicon based optoelectronic materials capable of emitting light in the visible portion of the spectrum are of great technological importance. Materials exhibiting this behavior have been synthesized by creating silicon nanostructures, in hopes of exploiting quantum confinement effects to achieve the desired results. Crystalline and amorphous silicon quantum wells have been shown to exhibit size dependent photoluminescence spectra which are attributed to quantum confinement effects. Along the way, however, much doubt has crept in regarding the true origin of the light emission. The use of amorphous silicon for quantum wells suggests that structural disorder in the material may contribute to the luminescence efficiency by relaxing the momentum selection rules. Oxidation of these quantum well systems can result in the emergence of photoluminescence from defects within the oxide layer. Both porous silicon and silicon nanoparticles, which are quantum dot systems, have been found to exhibit visible photoluminescence. Difficulties in obtaining size information and correlating it with PL behavior have precluded the assignment of a luminescence mechanism. Experimental evidence suggests that many of the theoretical predictions of energy gap as a function of size for small silicon particles may be incorrect, and that the particle sizes of interest are smaller than what was once believed necessary for quantum confinement. This push toward smaller sizes brings into play the question of structural instability in very small silicon particles. Often these small particles take on more close packed structures than the bulk silicon crystal structure, which can introduce disorder into the particles and produce something that may look much like amorphous silicon. Experimental results indicate that porous silicon may have some local disorder. The role of oxide defects in these quantum dot systems must also be determined.

It is also clear that debate continues regarding the pathway by which carriers recombine to

generate the emitted light in nanoscale silicon materials. Some argue that emission is due to a band to band-like recombination from the lowest normally unoccupied state to the highest normally occupied state, a pure quantum confinement model. Others contend that the excited carriers pass through some intermediate state, often called a "surface state". Several different theories have been put forth regarding the actual identity of this intermediate state.

It is the goal of this document to demonstrate that visible light emission in nanostructured silicon materials is due to quantum confinement. The importance of this mechanism over other surface state mechanisms will be evident from the photoluminescence properties of the material. The temperature and excitation intensity dependence of the photoluminescence emission will be examined and will be explainable only via a quantum confinement mechanism. Studies of the luminescence from large oxidized silicon particles and small amorphous silicon particles will show that these species have no role in the luminescence from silicon nanoparticle films. The correlation between particle size and photoluminescence and the consistency between these results and the quantum confinement model for energy gap as a function of particle size will make it clear that quantum confinement effects are the origin of the visible photoluminescence.

Chapter 2

Experimental

Films of silicon nanoparticles were synthesized using a pulsed laser ablation supersonic expansion cluster source. The microstructure of these films was studied using x-ray diffraction, transmission electron microscopy, scanning transmission electron microscopy, and x-ray photoelectron spectroscopy. Various approaches were used to separate out particles of different sizes found to be produced by the cluster source. The visible photoluminescence properties of the films were studied as a function of excitation intensity, sample temperature, and the temporal nature of the excitation source.

2.1 Nanoparticle film synthesis

Films of agglomerated silicon nanoparticles embedded in a native oxide matrix were synthesized using pulsed laser ablation supersonic expansion.[114] Silicon particles ranging from single atoms to micron sized particles were deposited onto a variety of substrates. The standard system was modified to study the impact of particle size and structure on the photoluminescence behavior of the deposited films.

2.1.1 Pulsed Laser Ablation Supersonic Expansion Source

The silicon nanoparticles studied were produced using a pulsed laser ablation supersonic expansion source. This source is modeled after one originally developed for the synthesis of small, gas phase metal clusters by the group of Smalley.[69] This approach has been

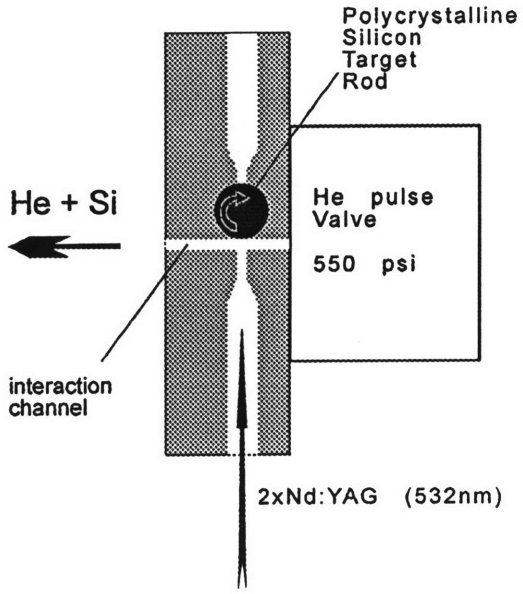

Figure 2-1: Schematic representation of the stainless steel source block. The silicon source rod and helium/silicon interaction channel are contained within the source block.

successfully used by other researchers to produce and study semiconductor clusters.[72, 73] A rotating polycrystalline silicon rod, 99.9999% pure, 0.25 inch diameter, and 3 inches long, is placed inside a stainless steel source block, as shown in Figure 2-1. A pulsed, frequency doubled Continuum Model NY60 Nd:YAG laser was focused to a 1 mm diameter spot at the surface of the target rod. The laser operates in a pulsed, Q-switched mode, with a repetition rate of 20 Hz and a pulse duration of 7 nanoseconds. The ablation laser delivers a power of 3 to 10 milliJoules per pulse (mJ/pulse) to the target rod at a wavelength of λ=532 nm, which corresponds to a power density of 15-50 W/cm^2.

The target rod and the stainless steel block are located in a vacuum chamber pumped by a Varian VHS-10 diffusion pump backed by a Leybold Heraeus Trivac D30A mechanical pump. The chamber is held at a background pressure of 10^{-7} torr. The laser vaporizes the surface of the target rod to generate a silicon plasma. The target rod is located adjacent to a high speed pulsed solenoid valve (General Dynamics Series 9) which opens at a user

determined fixed time synchronized to the ablation laser pulse. This valve gates the flow of pressurized helium (He) gas (99.999% pure) past the rod. The helium gas line is at high pressure (~550 psi) and thus the gas expands rapidly into the evacuated chamber. The helium entrains the silicon plasma and carries the atoms into a 1 mm diameter, 8 mm long interaction channel. In the channel, the carrier gas atoms collide with the silicon atoms in the plasma and cool them. These cooled silicon atoms act as heterogeneous nucleation sites where further collisions with silicon atoms from the plasma lead to the formation of clusters. The carrier gas and silicon clusters then expand into the vacuum system in a supersonic expansion. The gas expansion raises the chamber pressure to $\sim 10^{-4}$torr. At this pressure, there is no further interaction between the clusters and carrier gas and thus the particle sizes remain unchanged. In the gas phase, the clusters remain hot, with temperatures expected to be ~500 K.[115]

The pulsed nature of this technique leads to the formation of twenty individual gas phase packets of silicon clusters and helium carrier gas per second. These are separated in time by 50 milliseconds, so that the individual packets are completely independent of each other. In the packets, the clusters separate according to size due to a phenomenon known as velocity slip, which has been exploited in order to achieve size selection of the clusters in other systems.[116] Since the particles are accelerated through the vacuum system through momentum conserving collisions with the helium carrier gas, the smallest particles (having the least mass) will attain the largest velocity and travel in the front of the cluster packet, while the largest particles will move more slowly and travel in the rear. The packet's time of flight has been measured using a Beam Dynamics Model FIG–1 fast ion gauge (FIG) located in an adjacent secondary, differentially pumped vacuum chamber, as shown in Figure 2-2. The FIG is a fast version of the familiar Bayard-Alpert ionization gauge, measuring the pressure fluctuations caused by the presence of the clusters in the gas phase and the carrier gas with microsecond resolution. Knowing the distance between the source block and the FIG, as well as the relative timings of the ablation pulse signal and the fast ion gauge signal, allows for the determination of the cluster velocity distribution and kinetic energy. The fastest clusters within a packet travel at 2100 m/s, while the slowest clusters travel at 1600 m/s.

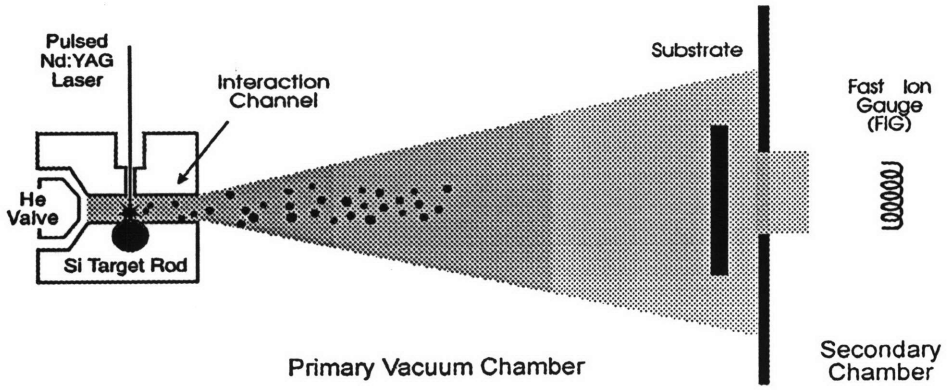

Figure 2-2: Schematic representation of pulsed laser ablation supersonic expansion nanoparticle synthesis system.

Particles formed by this source grow as a result of collisions involving single silicon atoms. These collisions occur for the short time, on the order of tens of microseconds, during which the clusters are located in the interaction channel. This is a highly nonequilibrium and chaotic process. As a result, clusters of many different sizes are produced, ranging from atomic silicon up to clusters microns in size. These largest particles may be the result of the ejection of micron sized pieces from the target rod during the initial ablation process. The presence of particles within this size range has been confirmed by electron microscopy and mass spectrometry.

The distribution of particle sizes produced by laser ablation sources has been predicted to have a lognormal form, given by the function

$$F(x) = \frac{1}{x}\frac{1}{\sqrt{2\pi\sigma^2}}\exp\left(-\frac{(\ln x - \mu)^2}{2\sigma^2}\right)$$

where x is the number of particles at a given size, σ is the statistical median, and μ is the standard deviation of the distribution.[117] This distribution predicts an exponential tailing off in number of particles at larger sizes. Prior work on silicon particles synthesized by laser ablation indicates a maximum in the distribution at sizes of less than 30 atoms.[118] Clusters of the size believed to be visibly emitting (50-1000 atoms) should fall within the exponential tail. Some cluster sizes are expected to be coordinately saturated and have a low probability

of further growth even while still in the formation channel. These "magic number" sizes will be more stable and will occur more frequently, resulting in sharp peaks in the cluster size distribution (such as C_{60}). In general, little work has been done to try to characterize the larger clusters ($\geq$ 50 atoms) in the distribution of silicon clusters produced by pulsed laser ablation supersonic expansion sources.

Some rough control over this broad size distribution has been realized by altering the ablation parameters. By increasing the amount of helium gas present at the time of ablation, more interaction can be achieved and thus more cooling collisions will occur, resulting in a larger mean particle size. This can be realized by changing the relative timing of the valve and ablation laser. Increasing the length of the interaction channel also results in more collisions and a larger mean particle size.[119] The effects of these deposition parameters on nanocluster size has been correlated with time of flight analysis and photoluminescence spectroscopy.[120] Mean particle size has also been altered by post deposition chemical processing and correlated with photoluminescence emission wavelength.[121] Both studies have pointed to the role of quantum confinement in the photoluminescence. Much of the work of this thesis has been directed at further narrowing this size distribution and identifying the species responsible for light emission. The approaches to size discrimination that were investigated are reviewed in Section 2.2.

2.1.2 Materials

Source

The target rods for the pulsed laser ablation supersonic expansion experiment are 0.25 inch in diameter and 3 inches long. For the fabrication of silicon nanoparticles, they are 99.9999% pure polycrystalline silicon, but silicon can be substituted with other materials in order to make different kinds of particles. Since the ablation process removes material from the source rod, it is necessary to move the target around in order to move the ablation spot, thereby preventing the target from being quickly destroyed. In this system, the target motion is achieved by attaching the rod to a rotating threaded screw so that the ablation spot effectively moves around and up and down the rod, resulting in a threading pattern being ablated into the source rod. The threaded screw is driven by a MicroMo 2233F012S54

22/2K 308:1K179 motor and gearhead assembly. The extent to which the rod travels up and down is determined by a set of mechanical switches.

Substrate

The substrates used were chosen for their suitability for characterization techniques and post deposition processing. Traditionally, work on these materials has involved wet chemical processing and hydrofluoric acid exposure, which led to the use of 0.06" thick Teflon substrates. Silicon wafers and niobium sheet, 0.13 mm thick, were also used. For the electron microscopy, samples were prepared by direct particle deposition onto Cu grids coated with either pure amorphous carbon, holey carbon, or carbon+Formvar support films.

For fabrication of a standard sample, the substrate was place at a distance of between 9 and 12 cm from the stainless steel source block, directly in the path of the supersonic expansion. The substrates used were a variety of sizes and shapes. For this study, the substrates used were typically individual pieces of Teflon, silicon wafer, or niobium, ranging from $1cm^2$ to 2 cm^2, mounted on a larger support substrate such as a glass slide or plastic slide. The TEM grid substrates were also supported by either slides or silicon wafers. Some of the samples studied were produced by placing larger pieces of Teflon or entire silicon wafers into the particle beam and then cutting or breaking the larger substrate into smaller pieces.

For the various attempts at size discrimination, the position of the substrate was changed to allow for the size selection apparatus placed between the source and the substrate. Substrate materials were the same as used for standard samples, with only some slight changes in overall substrate geometry to allow for more complex mounting schemes. The placement for the substrates in each of these experiments will be addressed in detail in Section 2.2.

2.1.3 Post-deposition processing

In order to realize any luminescence efficiency from a nanoparticle film it is necessary to passivate the surfaces of the particles.[122] This is generally true for all semiconductor nanoparticle systems, owing to the large surface to volume ratio in these very small particles. Silicon provides a simple natural surface passivation technique, through its native oxide, SiO_2.

Aging

For many of the standard samples, and for all of the size selection attempt samples, the only processing performed was atmospheric aging. Samples were removed from the vacuum chamber and exposed to ambient air in order to oxidize of the particle surfaces. The oxidation process was carried out as the samples were stored either open or enclosed within fluoroware or plastic containers. The luminescence of aged samples was monitored during the course of the aging process, and it was found that the luminescence behavior reached a final spectral peak wavelength, which remained unchanged with additional aging, after three days.[121]

HF Dips

For some of the standard samples studied in the excitation intensity portion of this work, samples were exposed to a hydrofluoric acid dip. The films were dipped in 48 $^{w}/_{o}$ HF for 60 seconds, with stirring of the solution occurring during the duration of the dip. Some films were then rinsed in deionized water and blown dry with nitrogen gas, while other films were not exposed to the water but dried directly following the HF dip. This HF dip removed the native oxide present on the particles as well as the outer layer of silicon atoms. Dipped samples were subsequently re-exposed to ambient air and allowed to oxidize.

2.1.4 Large Particle Behavior

In an attempt to rule out some of the theories of luminescence that have been proposed, the photoluminescence properties of some larger silicon particles were studied. Samples having a relatively narrow size distribution of large particles (which contain no particles less than 10 nm in size) were provided by two sources. Dr. John Haggerty at MIT supplied powders synthesized by laser decomposition of silane.[123] The particles were in powder form, with the grains of powder representing agglomerations of particles approximately 30 nm in diameter. The particles had been exposed to air prior to delivery, and therefore had a native oxide layer. In order to rule out the role of oxide defects as a source of the photoluminescence, the oxide layer was removed from these particles by HF treatment and they were allowed to reoxidize in the same atmosphere used to age the pulsed laser ablation produced particles. These larger particles were also subjected to oxidation treatments in an oxidation furnace

to try to reduce particle size into the desired range, as well as to produce even more oxide layer from which potential defect luminescence could arise.

A second supply of larger silicon particles was supplied by Dr. Darren Castro. These particles were fabricated using a forced flow reactor. These particles were also in powder form, with the grains of powder representing particle agglomerations. The particles within these powders were 10 nm in diameter and were embedded within a native oxide, as confirmed by transmission electron microscopy.[124] The photoluminescence properties of both sets of large particles were studied in the same way those of the laser ablated films were, as will be described in Section 2.3.

2.2 Approaches to size discrimination

Since the goal of this thesis is to identify the light emitting species and attempt to confirm that the emission has a quantum confinement origin, it was of interest to study not just the entire ensemble of particle sizes, but also particles of a particular size or within a narrow size range. This would reveal if the emitting species falls within the size range expected to exhibit quantum confinement effects, or if the emission is perhaps due to defects in the oxides of large particles or due to agglomerations of the very smallest disordered particles, which are essentially amorphous silicon. In this study, a number of different techniques were investigated to try to achieve this size discrimination.

2.2.1 Mechanical Size Selection Utilizing Velocity Slip

As described in Section 2.1.1, the particles emerging from the interaction channel are accelerated through the vacuum system by collisions with the helium carrier gas. Since these collisions must obey the law of conservation of momentum, the smallest particles (having the least mass) will attain the largest velocity and tend to segregate to the front of the cluster packet travelling through the vacuum chamber, while the largest particles will move more slowly and travel in the rear. The packet's time of flight has been measured using a fast ion gauge (FIG) located in an attached secondary, differentially pumped vacuum chamber. Knowing the distance between the source block and the FIG, as well as the relative timings

of the ablation pulse signal and the fast ion gauge signal, allows for the determination of the cluster velocity distribution and kinetic energy. This measurement shows that the cluster packet reaches the fast ion gauge position over a finite time interval, meaning that the front of the cluster packet and the rear are travelling at different velocities. The fastest clusters within a packet travel at 2100 m/s, while the slowest clusters travel at 1600 m/s.

It is attractive to think about using the velocity differences between the large and small particles as a means of separating them. Mechanical velocity selectors were first employed to select out monoenergetic neutron beams.[125] Designs placed slots in a moving barrier which moved in such a way so as to produce a clear path only to particles with the desired velocity. Many researchers have considered applying this approach to velocity selection of particle beams [126] and it has been applied successfully to bismuth cluster beams used for cluster beam deposition experiments.[127]

The principle behind this technique is simple, as shown schematically in Figure 2-3. Consider a single point in space located along the particle beamline. At some instant in time the leading particle in the cluster packet will be present at this point. An instant in time later, the particles in some forward portion of the packet will have passed this point in space, while those in the rear segment of the packet will still have not passed. At a third instant, all of the particles will have passed the point. If an experiment is designed in which a mechanical shutter is moved into place between the first and third instants in time, at the second instant, then a film can be deposited which consists of only the fastest (i.e. the smallest) particles in the distribution. It could also be designed so that the shutter would be in place during the presence of the first half of the packet and would move away for the second half, thus allowing the deposit of a film of only the largest particles. By complicating the experiment further and include two shutters at different positions in space, it is possible can trim the distributions from both ends, thereby selecting out a window of particle sizes somewhere in the middle. This approach is illustrated schematically in Figure 2-4.

While simple in theory, enacting this scheme into experimental practice is somewhat more difficult. The hardware employed is shown schematically in Figure 2-5. Two chopping wheels, 5.715 cm in diameter and 0.02 inch thick, were employed. Each wheel had two chopping holes, 7.94 mm in diameter, located 2.29 cm from the center of the wheel, 180°

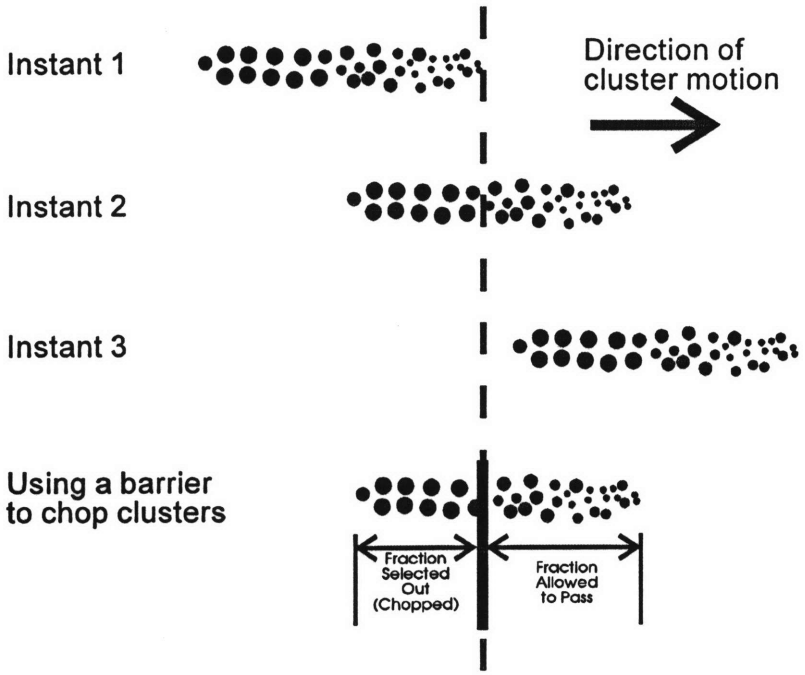

Figure 2-3: Schematic representation of how the introduction of a mechanical shutter can be used to size separate a cluster packet in which velocity slip has taken place. At instant in time 1, the fastest clusters are reaching the point in space represented by the dotted line. At the second instant, some of the clusters have passed this point while others have not yet done so. At the third instant, all of the clusters have passed. By introducing a mechanical shutter at the second instant, it is possible to collect only the fastest portion of the cluster packet.

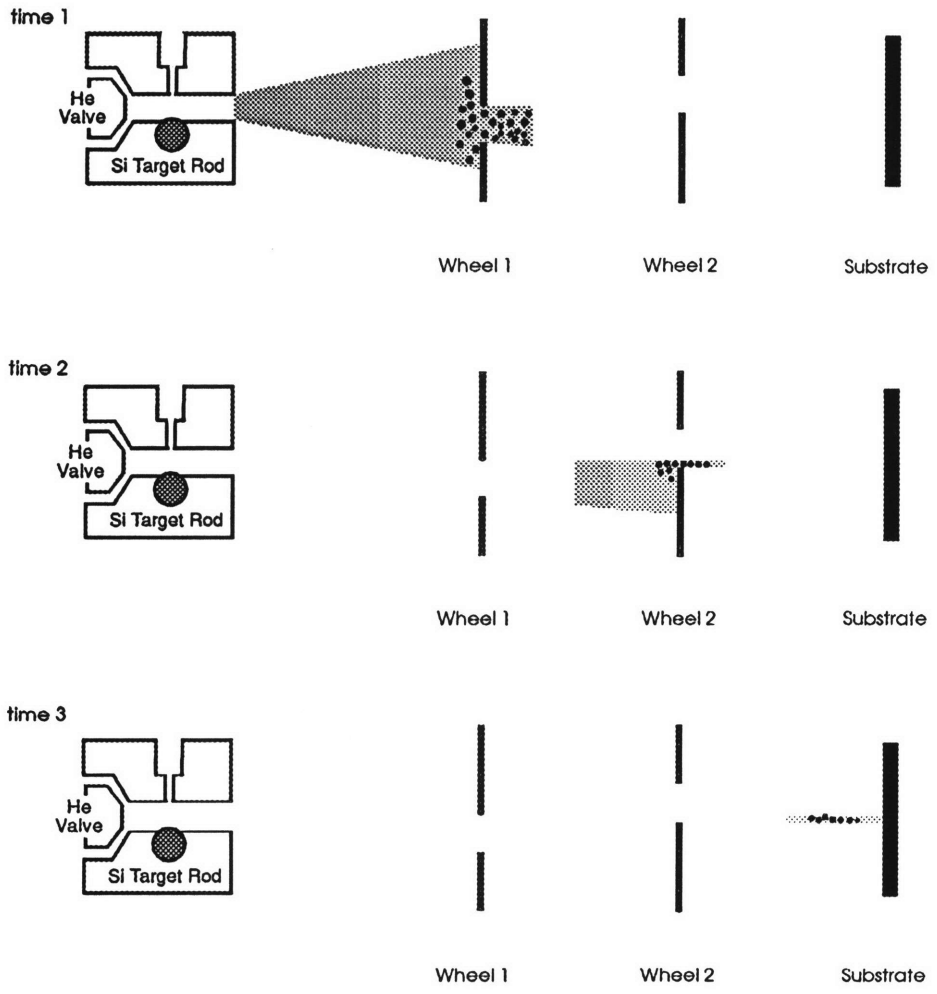

Figure 2-4: Schematic representation of how two mechanical shutters can be used to select gas phase clusters. The three images represent three instances in time as the particles traverse the system from left to right.

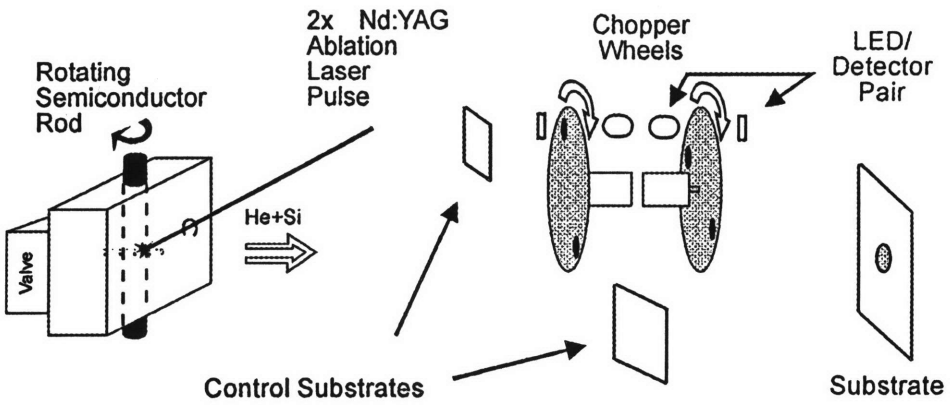

Figure 2-5: Schematic representation of the chopper wheel system employed for mechanical velocity selection experiments.

apart along the wheel circumference. The first wheel was located 12 cm from the source block. The second was located 11.3 cm from the first wheel, a total 23.3 cm from the source. The wheels were positioned so that the center line of the chopping holes was coincident with the cluster beamline when the holes were at the bottom of the wheel rotation, as determined by aligning a HeNe laser along the beamline. Both wheels were powered by MicroMo 1624T006S+X0650 motors mounted on an aluminum mounting rig. The wheels were affixed to the motor spindle using a pair of set screw collars for each wheel. One collar was placed on each side of the wheel, with the friction between the wheel and the collars transferring the force from the spindle to the wheel. The collars were secured to the spindle using their set screws. Also mounted on this rig were infrared LED/photodetector pairs which allowed the turning of the wheels to be converted into an electrical signal. Each wheel had a separate photodiode and detector, so the turning of the pair of wheels produced two electrical pulse trains. A pulsed signal was generated when no light was detected when the body of the wheel blocked the LED and light was detected when the hole was present at the LED position.

These electrical signals were used to achieve synchronization of the entire experiment. Ordinarily, the pulsed laser ablation supersonic expansion experiment timing is synchronized off of a standard 20 Hz internal clock signal in a Stanford Research Instruments DG535 digital delay generator. This frequency was required by the design of the ablation laser, which could

only operate at a maximum frequency of 20 Hz. At a set time after this internal trigger, a signal is sent to a timing box which generates a pair of signals that are sent to the ablation laser. The first signal initiates the charging of the laser capacitor banks and the second fires the Q-switch, which allows the laser light to be released from the laser. At another set time after the internal trigger, a different signal is sent from the DG535 to the electronic circuit that drives the helium solenoid valve. The duration of this pulse controls the length of time the valve is opened. The relative timing of the laser pulse and the helium pulse can be controlled by changing the settings on the DG535 which determine the times at which these pulses are generated. For a typical experiment, the valve pulse signal and the ablation laser firing signal are separated in time by 20-120 μ sec.

In the chopper wheel experiment, this setup was modified somewhat. The pulse train generated by the turning of the wheel closest to the source block, the first wheel, was used as the trigger pulse. A turning rate of 20 Hz (actually 10 turns/second, given the two hole arrangement) was far too slow to hope to achieve any cluster beam chopping, so the wheels were operated at a higher speed of either 100 Hz (200 Hz signal) or 160 Hz (320 Hz signal) and a computer generated counter was used to break this down to a useful 20 Hz signal. The front wheel speed was constantly monitored by a computer program which determined if the frequency was varying. It determined this two ways, from the frequency parameter generated when the wheel signal was input into a LeCroy model 9450A digital oscilloscope and by directly counting the pulses from the wheel signal. If the frequency varied, the computer changed the drive voltage, which was the amplified output of a Lab PC+ analog to digital conversion card, in order to restore the proper turning rate. The frequency down-converted wheel 1 signal served as the trigger pulse for the experiment. The rest of the ablation portion of the experiment went as previously described, except that it was synchronized off of wheel 1. The time delay between the trigger and ablation process was chosen so that the clusters would be present at the wheel at the time the hole was in the vicinity of the cluster beamline. The exact value of this timing was varied as part of the size selection experiments.

The second chopper wheel was synchronized to the first. This was also achieved through computer control along with the use of a Stanford Research Systems SR510 lockin amplifier.

The computer monitored the initial frequency of wheel 2 and modified the offset output of the lockin, which drove wheel 2. When the speed of wheel 2 matched that of wheel 1, the lockin amplifier was activated in lockin mode in order to synchronize the wheels. The computer continued to monitor the speed of wheel 2 and, in the event that the wheels became unlocked, turned off the ablation laser, returned the wheels to synchronization, reactivated lockin, and restarted the laser. The lockin amplifier allowed the variation of the phase between the electronic signals generated by the wheels, so that the positions of the holes relative to each other could be varied. It was also possible to run the wheels turning the same direction and opposite directions. Both wheel rotation schemes were investigated.

For sample deposition, a substrate was placed along the beamline 10.5 cm behind the second wheel, a distance of 33.8 cm from the source block. The extra distance behind wheel 2 was required so that the sample could be moved into and out of the cluster beamline, allowing for cluster synthesis to be characterized using the FIG. To monitor the impact of the chopper wheel presence on the sample, a control sample was placed above the beamline in front of the first wheel, 11.5 cm from the source block, 2.5 cm above the beam line. Another control sample was placed below the beamline on a shield that was placed below and in between the two wheels. This sample was located 16 cm from the source block, 1 cm below the beamline. These controls allowed for the comparison of luminescence from samples which did and did not undergo the mechanical size selection experience.

2.2.2 Particle Deflection Using a Crossed Gas Beam

The principle behind the velocity slip of clusters in the cluster beam can also be employed to develop another apparatus for size selection. Size discrimination of neutral clusters in beam experiments has been achieved using an elastic scattering crossed beam approach. In this approach, a gas jet is introduced into the experiment and is directed perpendicular to the cluster beam. The clusters travelling through the vacuum chamber intersect the gas jet and undergo collisions with the gas atoms. Due to conservation of momentum in these collisions, lighter, smaller particles are knocked off of the beamline to a greater extent than heavier, larger particles. Separation of particles of different sizes using this technique has been observed for Ar_x clusters [128] and Na_x clusters.[129] By placing a substrate in the

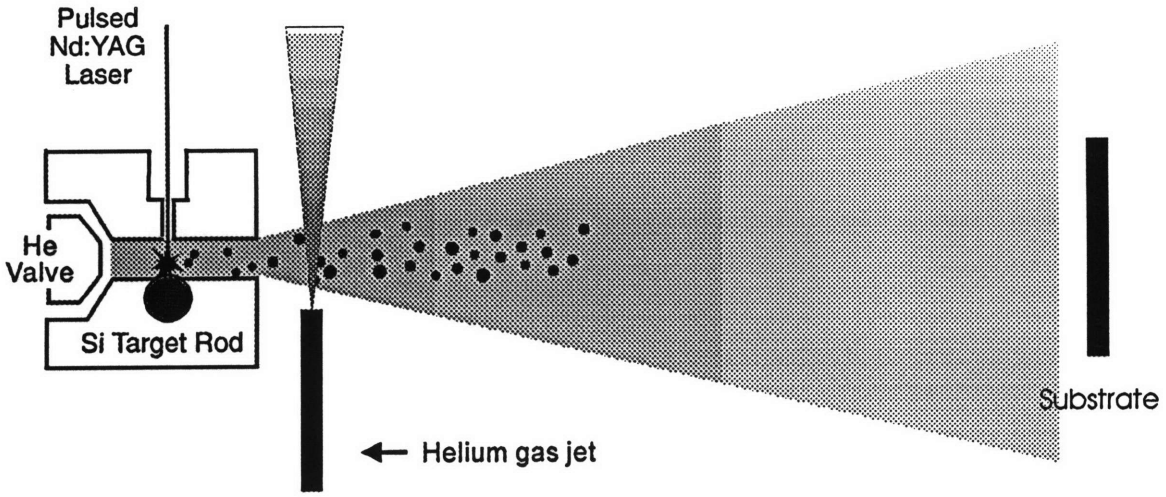

Figure 2-6: Schematic representation of the experimental setup used for the crossed gas beam experiment.

path of this altered expansion, particles of different sizes should be deposited in different locations on the substrate, allowing the luminescence behavior of differently sized particles to be studied individually.

In the experiment, a jet of helium (standard grade) gas was directed perpendicular to the cluster beam. The setup is shown schematically in Figure 2-6. The jet was created by soldering closed the end of a 1/4 inch diameter copper tube and drilling a 0.25 mm diameter hole in the plugged end. This small aperture extension was connected to a continuous source of helium at a pressure of 1 psi. The flow was regulated by a needle valve and was increased until the maximum pumping speed of the diffusion pump in the vacuum chamber had been reached. This jet was located 1 cm from the source block and was located 5 mm from the beamline. It was directed parallel to the floor of the chamber. For collection of the clusters passing through this gas jet, a large substrate was placed 20.5 cm beyond the jet, a total of 21.5 cm from the source block. A large substrate, typically an entire 3-4 inch silicon wafer or a 2 inch by 4 inch piece of Teflon, was chosen to collect clusters possibly knocked significantly off of the beamline. As much distance from the jet as possible was allowed in order to increase the spatial separation of clusters before deposition.

2.2.3 Light based deflection of particles

The idea that light carries momentum and can therefore exert forces on objects extends back to Kepler and Newton. It was confirmed by Maxwell, but the magnitude of the momentum was found to be small, meaning that conventional light sources could only exert very small forces on macroscopic objects. It was not until high intensity light sources such as lasers were developed that any practical applications for these light forces could be considered. The optical forces resulting from the momentum of laser light are capable of strongly affecting the dynamics of small particles ranging from micron sized macroscopic particles down to atoms. This has allowed for the trapping and levitation of small particles, and the deflection and patterning of atomic beams.[130]

The principle behind this technique is simple. The light output from a laser has a nonuniform spatial intensity profile, with higher intensity light being found at the center of the beam and lower intensity toward the outer edges. A macroscopic particle sitting within this beam has physical dimensions, meaning that different regions of the particle will experience different intensities of light, as a result of the intensity profile. For a particle off center of the laser beam, the forces on the side near the center of the beam and near the edge of the beam can be considered. Due to the fact that there is more light near the center of the beam, the force resulting from this light is greater. This can be broken down to result in two forces, one which acts axially along the laser beam and one which draws the particle into the center of the beam. The situation is similar for an atom in a laser beam. There is a scattering force that drives the atoms in the direction of the light and a gradient force that pulls them into or out of regions of high intensity light.

Different researchers have taken advantage of both the axial force and the gradient force in applying radiation pressure. Ashkin has observed the net motion of macroscopic particles and atoms in the direction of an applied laser beam, noting that the "absorption and isotropic reradiation by spontaneous emission of resonance radiation striking an atom results in an average driving force or pressure in the direction of the incident light."[131] He further exploited this axial light force in the design of a more sophisticated optical arrangement to guide atomic beams in a circular path.[132] More recent work has concentrated on the application of the gradient light force for atomic deposition and lithography. Here, mirrors

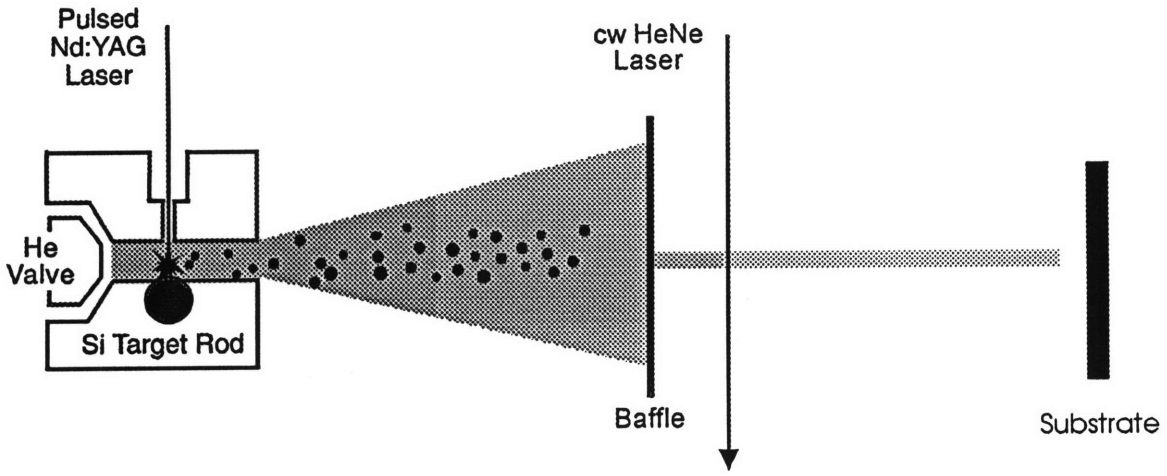

Figure 2-7: Experimental setup employed for the light force based particle deflection study.

are introduced to generate a standing wave in the path of an atomic beam. The standing wave geometry creates regions of high light intensity and low light intensity. The wavelength of the light is chosen to be tuned to the absorptions of the atomic species being used. Gradient light forces focus the atoms in the beam into regions of high or low intensity. By choosing the atomic species carefully, the wavelength of the light can be chosen to produce very narrow lines of atoms. This technique has been applied to beams of sodium atoms [133] and chromium atoms.[134] By applying multiple beams and interference techniques, it is possible to generate two dimensional patterns of atoms based on gradient light forces. This has been demonstrated for chromium atoms [135] and neon atoms.[136]

The goal is to employ the axial force resulting from light to knock the particles away from the cluster beamline, with the distance they move away depending on the particle mass. The experimental setup for deflecting particles with light was similar to that used for the gas jet deflection experiment, as is depicted in Figure 2-7. In this case, a beam of light was directed perpendicular to the cluster beam. This setup was similar to the original experiment of Ashkin [131], designed to apply a force to the particles in the direction of the light beam. This geometry, while simple, should result in a distribution of particles of different size away from the cluster beam, with smaller particles having greater displacement

as a result of the light force and the law of conservation of momentum. The light source was a SpectraPhysics model 105-2 HeNe laser, powered by a Uniphase model 215-1 power supply. This laser operates at $\lambda = 543$ nm and was used at an output power of 10 mW. It was focused to a spot of 2 mm in diameter. The beam was directed perpendicular to the cluster beam and incident upon it 10.5 cm from the source block. The collection substrate was placed 21.5 cm from the source block, 11 cm beyond the incidence of the laser beam. A baffle was employed in order to narrow the cone of the cluster source into a more well defined beam, so that only those clusters impacted by the laser beam were deposited. This baffle was located 10 cm from the source block and had a 2 mm diameter aperture located on the cluster beamline.

2.2.4 Quadrupole mass filter

The final approach to size discrimination employed was to install a quadrupole mass filter in the deposition system. The goal here was to deposit films consisting of silicon particles of a single size and study the luminescence behavior of films having different particle sizes. Electric quadrupole mass filters utilize strong focusing principles similar to those in high energy accelerators.[137] The quadrupole mass filter is constructed of four electrically conducting parallel hyperbolic cylindrical surfaces, as shown schematically in Figure 2-8. Opposite filter electrodes are connected together, and to one pair is applied a potential $\Phi(t) = U + V\cos(\omega t)$, where U is a D.C. voltage and V is the peak amplitude of a radio frequency voltage operating at the frequency f, where $\omega = 2\pi f$. To the other pair of electrodes is applied the same potential, but of opposite sign. This arrangement is illustrated in Figure 2-9. Under these conditions the equipotential surfaces are symmetric hyperbolic cylinders and the potential on the z-axis (which runs along the length of the filter) is zero. If an ion is injected at the end of this assembly with a motion generally parallel to the z-axis, the R.F. and D.C. fields which are perpendicular to the z-axis will cause it to undergo transverse motion. The differential equations describing this motion have solutions containing either an exponential factor or an oscillatory factor, depending on the charge to mass ratio of the ion. With the proper choice of U and V, a given charge to mass ratio will have stable trajectories, that is certain ions will have paths that oscillate about the z-axis and finally emerge from the

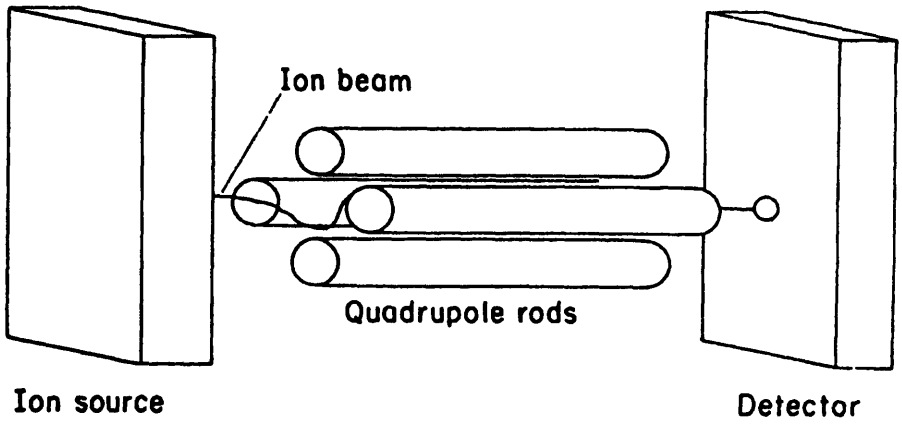

Figure 2-8: Schematic representation of the design of a quadrupole mass filter. Ions enter the region surrounded by the four electrical poles, are acted upon by the applied electric fields, and may exit at the end where the detector is located. From Reference [138]

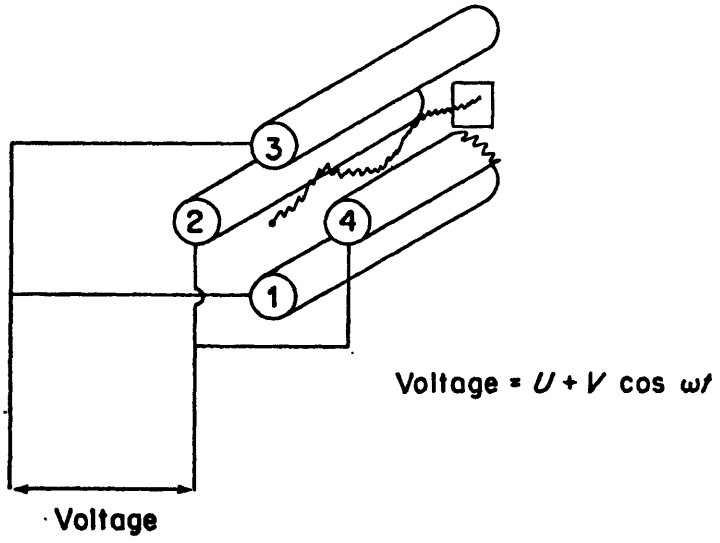

Figure 2-9: An illustration of the voltages applied to the poles of a quadrupole mass filter and the impact of these voltages on an ion having the proper mass to pass through the filter. From Reference [138].

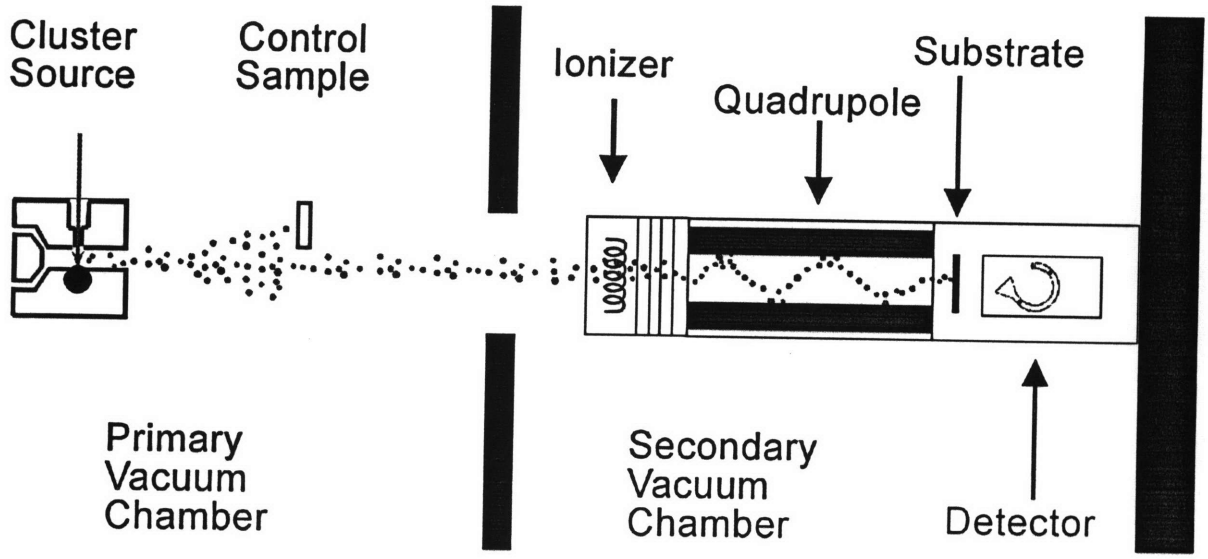

Figure 2-10: Schematic representation of the quadrupole mass filter as it is installed in the pulsed laser ablation supersonic expansion experiment.

opposite end of the mass filter. Ions with other charge to mass ratios will have unstable solutions, corresponding to paths that take them away from the z-axis and ultimately lead to collisions with the electrodes. In this way, the filter eliminates all ions except those having the desired mass, assuming all ions are singly charged.

The quadrupole mass filter was installed in the secondary differentially pumped chamber. It was attached to the back wall of the chamber, which runs parallel to the face of the source block, perpendicular to the cluster beam, as shown in Figure 2-10. The quadrupole was installed so that its axis was coincident with the cluster beamline. The quadrupole system used was an Extranuclear Laboratories/Extrel QPS system equipped with an electron multiplier collector and 031-3 preamp electrometer controller, a 041-3 electron impact ionizer controlled by 020-25 ionizer control unit, and a # 14 High Q Head powered by an Extrel quadrupole control and R.F. power source. These control units allowed for the control of the ionizer current, ion focusing optics to direct clusters into the quadrupole, control of the pole potentials for particle selection, and control of the detector voltage for extracting particles from the quadrupole and detection. Modifications were made to the circuitry of the High Q Head in order to expand the range of mass settings achievable before power supply overload.

The quadrupole mass filter employed had a rod diameter of 0.75 inch, resulting in an effective quadrupole radius (the radius of a circle inscribed within the poles, a critical parameter for quadrupole performance) of 0.822 cm. The quadrupole rods were 20 cm long. The entire assembly of electron multiplier enclosure, quadrupole, and electron impact ionizer was 38 cm long, and mounting this on the back wall of the chamber placed the entrance to the ionizer approximately 60 cm from the source block. A slot was cut into the electron multiplier enclosure to allow the insertion of a substrate into the post quadrupole region, where clusters capable of traversing the quadrupole were collected. This placed the substrate 88 cm from the source block. Typical substrates used were silicon wafers, as these allow for the deposits to be easily detected by eye. For photoluminescence, Teflon substrates were employed to ease photoluminescence measurements, owing to the differences in optical properties of the substrates. For comparison to a non-size selected sample, a substrate was placed 1 cm off of the cluster beamline 13 cm from the source in the primary chamber while the quadrupole selected films were deposited. Under typical operation of the quadrupole and ionizer assembly, the filter was tuned to the masses of clusters containing 1-9 silicon atoms and the resolution was varied from 70% to 100%. The quadrupole R.F. source was operated at a frequency of 1.29 MHz. The ion optics settings, used to extract the ions from the ionization region and focus them into the quadrupole, were: ion energy 19.1 V (for extracting the ionizing electrons from the filament), extractor voltage 10 V, lens 1 voltage -85 V, lens 2 +75 V, and lens 3 -155 V.

Modeling of Ion Behavior in the Quadrupole Mass Filter

To more completely understand the impact of the quadrupole mass filter on the clusters reaching the deposition area, the behavior of the clusters in the presence of the quadrupole was modeled. The commercially available ion optics modeling software package SIMION 3D was used.[139] A standard plug-in for modeling quadrupole mass spectrometers was also employed. This package allowed for the study of the impact of several different spectrometer parameters on the ability of particles of various sizes to traverse the quadrupole region. SIMION 3D models the electrostatic fields and forces created by a collection of shaped electrodes given certain symmetry assumptions. It uses a finite difference technique called

over-relaxation to perform the modeling. This determines the electric field in regions within defined potential arrays that do not lie in the electrode regions. The motion of ions within these potential arrays is computed based on the coulombic interactions. The quadrupole plug-in requested user input values of the operation frequency, resolution, and mass to which the filter was tuned and then automatically determined the proper values of the potentials on the poles. The software allowed for the study of ions of various masses. The ion kinetic energy was also a variable parameter, enabling the replication of the initial velocity that the silicon clusters had as a result of the supersonic expansion synthesis process.

2.3 Photoluminescence Spectroscopy

The light emitting properties of the samples were studied using photoluminescence emission spectroscopy. Standard samples containing all sizes of nanoparticles and those having undergone size selection processes were studied. The luminescence emission was also studied as a function of sample temperature and excitation pump intensity, and using light sources of different wavelength and temporal profile. This data provided insight into the role played by certain particles in the luminescence and into the recombination mechanisms present and active in the silicon nanostructres.

Photoluminescence emission spectroscopy measures the light emitted by materials after excitation with photons. A light source producing photons of higher energy than the absorption threshold of the material is used to excite carriers from the energetically lower lying filled states into higher, unoccupied states. These excited carriers eventually return to their ground state, often reducing their energy by emitting photons. These emitted photons are collected and the number of photons, or intensity of the light, is measured as a function of emitted photon energy, or light wavelength.

2.3.1 Light Sources and Optical Configurations

For the samples studied herein, photoluminescence measurements were performed using three different light sources. The sources were chosen based on their wavelength, intensity, and temporal profile.

Visible and UV CW Excitation from Xe Lamp

Samples were pumped with low intensity excitation light from a 450 Watt Xenon lamp, operating as a part of a SPEX Fluorolog Model FL212 Spectroflourometer. This instrument is located in the MIT Center for Materials Science and Engineering Optical and Surface Characterization Central Facility. Samples were excited using two different wavelengths, λ_{ex}=355 nm (UV) and λ_{ex}=488 nm (visible). These wavelengths were selected from the Xe lamp emission by a double grating excitation monochromator with two 2400 gr/mm gratings blazed at 250 nm. This arrangement allowed for the positioning of a power meter in the path of the beam to allow the measurement of the peak output power. The output power of this source was 0.65 mW at λ=355 nm and 0.14 mW at λ=488 nm, as measured using a Scientech 372 Power and Energy Meter. After passing through the wavelength selection monochromator, the incident beam was focused onto the sample in a $\sim$0.1 cm^2 spot. This beam was directed normal to the sample surface. Samples were clamped into a sample holder to ensure position at the focal point of the source light beam.

Visible CW Excitation from Ar^+Laser

In order to more fully study the impact of excitation pump intensity on the luminescence intensity, it was necessary to probe the luminescence with higher excitation intensities than the Xe lamp could provide. High intensity visible wavelength excitation was provided by a Spectra-Physics Model 168B-06 Ar^+ laser. This laser was operated at λ=488 nm, coincident with the wavelength chosen for study using the Xe lamp. Before incidence on the sample, the beam was passed through a short pass filter, which eliminated the residual light produced by the Ar^+plasma in the laser. After reflecting off a mirror, the beam was passed through a diverging lens to increase the spot size, and directed at the sample surface. The area of the excitation spot was $\sim$1cm^2. A power meter could be placed at this position in the optical line in order to monitor the excitation intensity, as was required for the excitation intensity dependent luminescence study. The maximum output power used was 800 mW. For the room temperature luminescence measurements, the sample was clamped into a sample holder such that the pump beam was incident on the film surface at approximately 85° to the surface normal. Typical luminescence spectra were recorded for a period of 1 minute.

Pulsed Ultraviolet Excitation

In probing the recombination pathway, it was of interest to study the luminescence after excitation from a very short, intense pulse of light. This was achieved using a pulsed Continuum Model NY61 Nd:YAG laser. The laser frequency was tripled to produce a wavelength of λ=355 nm. The maximum excitation power employed was 10 mJ/pulse, with typical measurements made using an excitation power of 1 mJ/pulse. Typical luminescence spectra were collected for a period of 3 minutes, meaning that samples were excited by 3600 laser pulses. The pulse duration of the laser was 7 nanoseconds. The area of the excitation spot was $\sim$1cm^2. Before incidence on the sample, the beam was passed through a short pass filter, which eliminated the residual λ=532 nm and λ=1064 nm light produced by the laser. After reflecting off a mirror, the beam was passed through a diverging lens to increase the spot size, and directed at the sample surface. A power meter could be placed at this position in the optical line in order to monitor the excitation intensity, as was required for the excitation intensity dependent luminescence study. For the room temperature luminescence measurements, the sample was clamped into a sample holder such that the pump beam was incident on the film surface at approximately 85° to the surface normal. The length of time for collection was kept as short as possible, as it was found that the ultraviolet laser pulses degraded the films over time.

2.3.2 Collection optics and detectors

Two different arrangements of light collection optics and detectors were used, the standard arrangement incorporated into the SPEX fluorometer and a stand alone optical line constructed for use with the laser sources.

Fluorometer

For these experiments, the luminescence light was collected via a front facing path, wherein light was collected along a path 23° from the sample normal. The light was bounced off a series of mirrors and then travelled through a long pass filter chosen to eliminate any stray excitation light that might find its way into the collection optics. For the λ=355 nm excitation, a 418 nm long pass filter was employed, and for the λ=488 nm excitation, a 495

nm long pass filter was used. This filtered beam was then passed through a 0.27 meter, f/4 imaging spectrometer with a 300 gr/mm grating blazed at 630 nm. Spectra were collected with the spectrometer center wavelength set at 700 nm, which allowed collection of light in the wavelength range from 533.2 to 863.2 nm. The luminescence signal was detected using a liquid nitrogen cooled CCD detector with 200-1050 nm sensitivity. The grating and CCD combination exhibited a nonuniform response across the wavelength range studied. The photoluminescence spectra were corrected for this nonlinear response using a standard correction curve established by the supervisors of the central facility. The spectral range of collection was selected to enable use of such as standard curve.

This detector was connected to a SPEX model DM3000 detector controller, which was then interfaced to a computer running SPEX spectrometer control software. This software package allowed for the determination of sample detection times, and data collection and processing. Mathematical processing of the data to obtain corrected spectra was also performed using the control software. The software was also used to convert the raw data files into ASCII format for exporting into data analysis and graphing software. These ASCII data files were imported into Genplot version 1.01, a scientific plotting program. Spectra were typically averaged using a 32 point averaging scheme for smoothing. Integrated intensities were calculated by performing a simple integration over the wavelength range of interest. Since the photoluminescence spectra were rarely symmetric, the peak emission wavelengths were most easily determined by either simple observation of the peak structures or by differentiation of the smoothed data to find the point at which the derivative of intensity as a function of wavelength passed through zero.

Laser Excitation Sources

For the experiments in which photoluminescence was excited by either the Nd:YAG or Ar^+laser, the collection optics differed from those of the fluorometer. A baffle with a small aperture was placed near the sample to reduce the amount of reflected light from the excitation source that entered the collection optics. The collection optics consisted of either a 418 nm or a 505 nm long pass filter (depending on the excitation wavelength) to eliminate any stray excitation light, a 62.9 mm focal length, 2 inch diameter collecting lens, and a

62.9 mm focal length, 2 inch diameter focusing lens with an antireflection coating. After collection and focusing, the photoluminescence emission light was passed through a 4 mm aperture placed 15 mm in front of the 75 micron entrance slit to a spectrometer, in order to match the f-number of the detection system optics.

The spectrometer was an EG&G PARC Model 1235 Digital Triple-Grating Spectrograph. Attached to the exit port of this 0.28 m focal length spectrograph was a EG&G Model 1453A 1024 element silicon photodiode array detector. This detector is sensitive to light with wavelength in the range of 200 to 1100 nm. The detector array was cooled to -20 °C using a water cooled thermoelectric cooler to reduce dark counts. The spectrometer and detector combination has a significant nonlinearity in its spectral response to different wavelengths in the range of interest. This nonuniformity was corrected for by calibrating the detector to the known emission from an Oriel Model 6333 quartz tungsten halogen white light source. Spectra were also automatically corrected for the presence of background light.

The silicon array detector was connected to a EG&G Model 1471A Detector Interface. This interface was networked to a computer via an IEEE-488 General Purpose Interface Bus (GPIB). The computer was equipped with OMA Vision optical multichannel analyzer data acquisition and analysis software. This package allowed for the establishment of spectral correction functions, the determination of sample detection times, and data collection and processing. The software was also used to convert the raw data files into ASCII format for exporting into data analysis and graphing software. These ASCII data files were imported into Genplot version 1.01, a scientific plotting program. Spectra were typically averaged using a 16 point averaging scheme for smoothing. Integrated intensities were calculated by performing a simple integration over the wavelength range of interest. Since the photoluminescence spectra were rarely symmetric, the peak emission wavelengths were most easily determined by either simple observation of the peak structures or by differentiation of the smoothed data to find the point at which the derivative of intensity as a function of wavelength passed through zero.

2.3.3 Excitation Intensity Study

The luminescence pathway was studied by probing the excitation intensity dependence of the luminescence intensity. The excitation intensity of the various light sources was controlled in different ways. For the Xe lamp source, a series of neutral density filters were introduced into the pathway of the incident beam. The filters were a metal neutral density set manufactured by Newport. Nominal densities of the filters were 0.1, 0.3, 0.5, and 1.0 optical density at 633 nm. These nominal densities were corrected for the density fluctuations as a function of wavelength using calibration scans of density as a function of wavelength provided by Newport. The intensities of both of the laser sources were varied by changing power settings on the instruments themselves. The intensity used for the luminescence pump was measured using a Scientech 372 Power and Energy Meter.

2.3.4 Temperature Dependent Photoluminescence

It was also of interest to vary the sample temperature between 4 K and 300 K during the excitation intensity study and while studying the visible photoluminescence under constant excitation conditions. To achieve this, samples were placed in an Oxford Instruments Model CF1204 continuous flow cryostat. Both liquid nitrogen and liquid helium were used as cryogens. While in the cryostat, the samples remained under a helium environment to prevent condensation on their surfaces at low temperature. The cryostat was equipped with windows for easy optical access to the sample being studied. The samples were mounted on a specimen holder whose position could be controlled to allow for retention of an optical alignment during a set of experiments.

2.4 Structural and Compositional Characterization

The structure and composition of the silicon nanoparticle films was characterized using a variety of techniques, including transmission electron microscopy (TEM), scanning transmission electron microscopy (STEM), x-ray photoelectron spectroscopy (XPS), and x-ray diffraction (XRD). Sample preparation was slightly different for each of the techniques depending on the requirements of the characterization tool.

2.4.1 X-ray Diffraction

X-ray diffraction measurements were conducted in both conventional and glancing angle geometries in order to determine the structural characteristics of the nanoparticle films. The conventional experiments were performed using a Rigaku RU-300 Rotating anode x-ray generator, while the glancing angle work was performed using an RU-200 unit, both in the x-ray diffraction central facility at the MIT Center for Materials Science and Engineering. The RU-300 was operated at 60 kV and 300 mA, while the RU-200 was operated at 60 kV and 200 mA. The source produced Cu Kα x-rays at $\lambda = 1.54$ Å. The incidence angle for the glancing angle experiments was varied from 1° to 8°.

For the x-ray experiments, it was desirable to reduce the background signal resulting from the substrate. For this reason, the substrates chosen were oriented silicon wafers and polycrystalline niobium. These materials have sharp diffraction peaks which can be easily identified and ruled out as being from the thin films, unlike amorphous substrates. By choosing a glancing geometry, it was possible to further reduce the substrate contribution to the signal, with the optimum glancing angle determined by trial and error. In this case, it was also possible to study especially thick films deposited on Teflon and plastic slide substrates. All of these samples were produced in the standard manner, wherein the substrates were placed in the path of the cluster expansion. The positions of the diffraction peaks were compared to standard patterns for silicon and the peak breadths were studied for the conventional geometry to look for signs of broadening associated with small grain size.[140] The glancing experiments were performed with an unfocused x-ray source, preventing the study of peak broadening effects.

2.4.2 Transmission Electron Microscopy

Both conventional and high resolution transmission electron microscopy were performed on nanoparticle films in order to observe the particle size distribution and the particle structure. All microscopy samples were prepared by placing a coated Cu grid in the path of the nanoparticle beam and allowing the particles to land on the support film. The particles are thin enough for the electron beam to pass through, so no further sample preparation was necessary. Films used included pure amorphous carbon, carbon+Formvar, holey carbon

films, and lacy carbon films. The highly porous films were generally poor for this study, as they are designed to hold large particles within the pore structure and even the largest particles in this study were far smaller than the holes and simply passed through the grids.

Conventional transmission electron microscopy was performed using a JEOL 200CX TEM with either a tungsten filament or a higher brightness LaB_6. Images were obtained using diffraction contrast imaging up to magnifications of approximately 600,000X. The microscopes were operated at an accelerating voltage of 200 kV. Electron diffraction patterns were also studied. These experiments were geared at determining the presence and sizes of larger particles in the samples and determining their structure. Dark field microscopy was performed using the diffracted beams from crystalline particles and using the diffraction rings produced by amorphous material. The goal of these studies was to determine if amorphous particles were present within the films or if all of the diffraction signal resulted from the carbon support films.

High resolution electron microscopy was performed using an Akashi/Topcon EM002B HREM operating at 200 kV. This microscope is equipped with a high brightness LaB_6 filament. Images were obtained using phase contrast imaging up to magnifications of approximately 6,000,000X, allowing imaging of atomic planes in the particles. The high resolution experiments were directed at analysis of smaller particles as well as structure determination of both large and small particles and a closer examination of the particle surfaces.

2.4.3 Scanning Transmission Electron Microscopy

Compositional analysis of the silicon nanoparticle films was performed using analytical electron microscopy/STEM. As for TEM, the samples were prepared by placing grids with support films in the path of the cluster beam. STEM was performed using a Vacuum Generators HB603 STEM. Compositional analysis was performed using x-ray analysis and x-ray mapping. As the electron beam is rastered across the sample, x-rays characteristic of the material of which the sample is comprised are generated. These x-rays were collected and their energy distribution studied. Correlating the beam position during rastering with the x-ray distribution generates a compositional map of the sample. Several regions of the samples were probed in order to generate x-ray maps, including those with obvious particle

formations and those without, in order to determine the composition of the particles and of the sample as a whole.

2.4.4 X-ray Photoelectron Spectroscopy

X-Ray photoelectron spectroscopy (XPS) was used to characterize the composition of the films and to study the structure of the silicon in the films. XPS measurements were carried out at the Harvard University Materials Research Laboratory using a Surface Science SSX-100 X-ray photoelectron spectrometer. This instrument features a monochromatized Al Kα x-ray source, which allowed for the study of both core level and valence band spectra.

XPS Basics

XPS is an experimental technique that employs the absorption of energy from an x-ray source by a solid coupled with the subsequent ejection of a photoelectron. The kinetic energy of the ejected electron differs from the energy of the absorbed x-ray by an amount equal to the binding energy of the electron. This binding energy is the energy required to remove an electron to infinity with no kinetic energy, and is basically an ionization energy. The ejected photoelectrons are collected and sorted by energy using an electron spectrometer. XPS is primarily a surface technique, sampling to a depth of 1-2 nm. This is a result of the fact that photoelectrons ejected from deeper in the film lose most of their energy escaping from the film or fail to escape at all. A core level XPS spectrum reveals information about the binding of electrons in the surface atoms of the film, or the bonding.

It is also possible to remove electrons from the valence band of the material. These electrons will have a very low binding energy, necessitating the use of a monochromatized x-ray source lest the information be washed out in the breadth of the source. It is possible to plot out the density of states in the valence band by measuring the number of electrons emitted at very low energy for a range of low binding energies. The valence bands measured in XPS are sensitive to the details of chemical bonding which can provide evidence of amorphization on a length scale much smaller than that addressed with electron diffraction.[141] A valence band XPS spectrum can thus reveal information about the structure of a silicon nanoparticle film by comparison the known spectra of crystalline and amorphous silicon.

Experimental Details

For this study, the x-ray source was a 300 W, Mg Kα (1253.6 eV) monochromatized x-ray beam. The take-off angle measured between the surface and the detector was 45°. The XPS system was held at a base pressure of less than 5×10^{-9} torr. Survey spectra were acquired in multiplex mode, typically looking at the Si 2s, Si 2p, C 1s, and O 1s peaks. Valence band spectra were also measured by monitoring the electron counts at low binding energy. This instrument was capable of handling almost any sample, so standard samples designed for photoluminescence characterization were used. These samples were approximately 3 cm^2 pieces of Teflon substrate with nanoparticle films deposited on them.

Since the films were deposited on insulating materials, there was a buildup of charge on the film as the sample lost photoelectrons. The positively charged surface leads to a change in the measured binding energy of the ejected photoelectrons. This correction varied along with the charge buildup and thus could change over the course of the experiment and the surface of the sample. Since this charging will impact all of the ejected photoelectrons equally, it is possible to correct for this effect by normalizing the XPS spectra to the adventitious carbon peak at 284.6 eV. This peak is present on all samples and is believed to be due to carbon that adsorbs onto the film surface during deposition or the sample transfer process. It is distinctly different from that for the carbon in the Teflon substrate, which can also be observed.

Chapter 3

Results and Discussion

Evidence will be presented that demonstrates that quantum confinement effects are responsible for the visible photoluminescence from silicon nanoparticles. These results will also rule out the alternative sources for the visible emission discussed in Section 2.2, luminescence from defects in the oxide coating, luminescence from amorphous silicon, and luminescence via a surface state mechanism. First to be studied were the luminescence and microstructural characteristics of a "standard" film, which is a film deposited using the pulsed laser ablation supersonic expansion source without the introduction of any particle size selection apparatus. Standard films contain particles of many different sizes, as will be shown. For comparison, samples consisting entirely of large (>30 nm) particles, provided by Dr. Haggerty, will be probed to determine the role of these large particles in the visible photoluminescence. The results of various size discrimination efforts will be presented in order to determine the role of particle size in the luminescence. In total, these results will show that the visible photoluminescence from the silicon nanoparticle films does not arise from the largest particles, indicating that defects in the oxide layer are not the source of the photoluminescence. The results will also demonstrate that the luminescence is not coming from very small, amorphous silicon nanostructures, ruling out structural disorder as the source of the luminescence. The luminescence emission will be shown to exhibit many characteristics indicative of quantum confinement effects, and it will be shown that films displaying visible photoluminescence contain particles of the proper size to produce quantum confinement induced luminescence at the wavelengths observed.

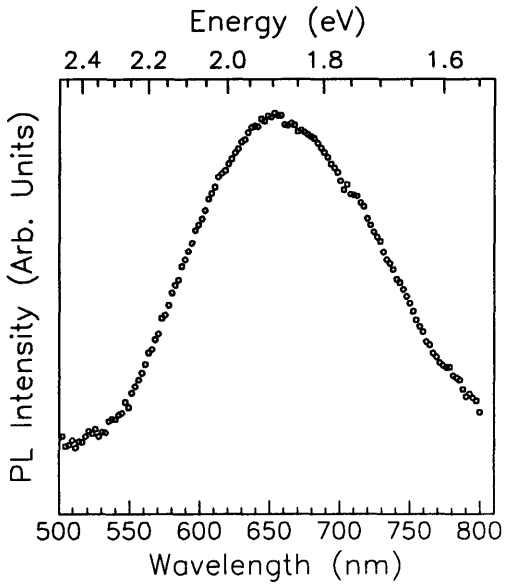

Figure 3-1: Typical photoluminescence spectrum from a silicon nanoparticle thin film. Luminescence was excited using a pulsed 3x Nd:YAG laser, $\lambda = 355$ nm.

3.1 Photoluminescence Properties of Standard Films

Figure 3-1 shows the visible photoluminescence spectrum for a standard silicon nanoparticle thin film deposited on a Teflon substrate and aged in air. The spectrum was acquired using a 3x Nd:YAG excitation source operating in pulsed mode at $\lambda = 355$ nm. The spectrum is peaked at ~660 nm or 1.9 eV and has a broad emission peak, with a full width at half maximum of ~0.5 eV. This emission spectrum represents an orange light emission behavior for films exposed to UV excitation from a Nd:YAG laser, a Xenon lamp, or a hand held UV lamp or exposed to blue excitation from a Xe lamp or Ar^+ laser. The photoluminescence emission is not present when studying bare substrates, indicating that it arises from the films. The luminescence appears to be stable indefinitely, as samples deposited five years ago show no change in luminescence.

The fact that any luminescence is observed is indicative of novel optical properties in a silicon based material. The visible wavelength of the emission implies that the source

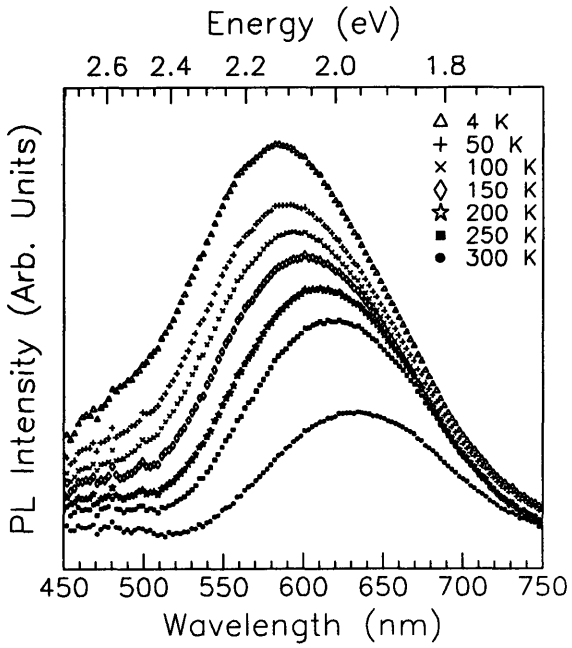

Figure 3-2: Photoluminescence spectra from a standard film measured at a series of temperatures. Luminescence was excited using a pulsed $\lambda = 355$ nm excitation source.

is not bulk crystalline silicon. The significant intensity belies a source different from the indirect gap band to band recombination from bulk crystalline silicon. The similarity to the emissions from porous silicon suggests a similar mechanism. The stability and reproducibility of the emission rules out the accidental deposition of some foreign emitter on the film during synthesis.

3.2 Temperature Dependence of Photoluminescence Emission

Comparison of the photoluminescence properties of silicon nanoparticle films to those of other known silicon light emitters can help to identify the origin of the photoluminescence. To achieve this goal, the temperature dependence of the photoluminescence was studied. Figure 3-2 shows a number of photoluminescence spectra for a single sample measured at a

number of different temperatures. Two features are observed. First, the spectra are observed to shift to higher energy as the temperature is reduced. This behavior is expected for a semiconductor and its magnitude is attributed to the enhanced electron-phonon coupling that occurs in small particles.[121] This suggests that the light emission is due to small silicon particles, rather than oxide defects or amorphous silicon.

The second feature exhibited by the temperature dependent spectra is an increase in emission intensity by a factor of approximately 2 as the temperature is decreased from room temperature to 4 K. This general trend occurs in most semiconductors and is a result of the suppression of lattice vibrations, which normally provide nonradiative recombination pathways via phonon emission events. At low temperature, these transitions are not available and radiative transitions are favored, resulting in enhanced emission intensity. The weakness of the temperature dependence in silicon nanoparticle films is evidence of the enhanced exciton binding energy predicted for quantum confined systems.[13] This has been predicted to be $\sim$175 meV in $\sim$3 nm diameter silicon nanoparticles, which is well above room temperature thermal energy. Therefore, excitons which in the bulk material would rapidly dissociate are able to exist to much higher temperatures in nanoparticle systems. This weak temperature dependence has been observed in other quantum confined semiconductors, including CdSe nanocrystals [142] and $Si_{1-x}Ge_x$ quantum wells.[143] This is in distinct contrast to the very strong temperature dependence of the emission intensity observed for amorphous silicon photoluminescence. For amorphous silicon, the peak PL emission intensity has been found to increase as much as four orders of magnitude as the temperature is decreased from 200 K to 60 K.[144] The absence of such a dramatic temperature dependence of the emission intensity suggests that amorphous silicon is not responsible for the visible photoluminescence observed from silicon nanoparticle films.

3.3 Excitation Intensity Dependence of Standard Film Photoluminescence

It was of interest to try to determine the luminescence mechanism by probing the luminescence pathway. To do this, the luminescence behavior of the films was studied as a function

of excitation intensity, temporal profile of the excitation source, and sample temperature. For a quantum confined system, both Auger recombination and state filling mechanisms are present. These will compete to control the observed luminescence behavior. The relative importance of each mechanism will depend on the kinetic conditions under which the carrier generation and recombination occurs. These conditions may be tailored to promote one pathway relative to the other by varying the rate at which exciting photons are absorbed by the nanoparticles under study.

The result of an increase of the excitation intensity on a sample of silicon nanoparticles will be the creation of multiple excitations in some particles. When Auger recombination kinetics dominate, these multiple excitations (one electron-hole pair plus any additional carriers) will give rise to nonradiative Auger recombination, as described in Section 1.4.2. So long as additional photons are absorbed by a nanoparticle at a rate slower than existing electron-hole pairs are consumed through this nonradiative path, little or no additional emission intensity will be observed.[145] Auger-limited emission has been repeatedly observed by researchers studying porous silicon using continuous excitation sources.[146] Auger lifetimes of 0.1 to 100 nsec have been calculated for silicon nanoparticles.[147]

The state filling mechanism is very different in that it can only be exhibited by highly excited quantum confined systems. Under intense excitation, the first excited state can become saturated and transitions from the higher excited states will begin to be observed. These transitions from higher energy states result in the emission of higher energy light.[22] This saturation and blue-shift can occur only when photons are absorbed at a rate greater than energy is released through some other path. The magnitude of the energy difference resulting from the saturation phenomenon can be estimated using the particle in a box construction developed in Section 1.6. Using this model, the shift arising from the difference between the first and second energy levels for silicon particles in the size range of 2-4 nm is 0.1-0.2 eV.

State filling has been observed from other quantum confined systems. For InGaAs/GaAs quantum dot systems, the intensity from the first excited state saturates with increased excitation intensity while intensity from transitions from the second state emerges.[43] InAs quantum dots also have been shown to exhibit this behavior, but the broader size distribution

relative to the InGaAs/GaAs dots allows only the observation of a saturation of the PL intensity at the low energy end of the spectrum with an increasing intensity to the higher energy end.[44] This behavior has also been observed from InP [45] and GaInP [46] quantum dots, CdSe nanoparticles in SiO_2, [148] and porous silicon in PMMA.[149]

Tailoring of the excitation conditions to preferentially promote one pathway must vary the rate at which exciting photons are made available to the silicon nanoparticles for absorption. The state-filling mechanism will be active only when sufficient time for the Auger process is not allowed. That is, additional photons are presented for absorption before the Auger process can occur, resulting in enough excited electrons to fill up the lower levels and begin occupation of the higher levels. This situation will be accessible through the use of an intense, short time duration pulsed excitation laser. Conversely, the Auger pathway will be optimized when sufficient time is allowed for the nonradiative recombination to occur before the next photon is incident. This route is optimized through the use of a continuous (cw) excitation source.

The Auger and state-filling mechanisms show distinctly different temperature dependences. A temperature dependence study under the two excitation conditions can be used to confirm the dominance of one mechanism relative to the other. The Auger recombination rate is known to decrease with decreasing temperature.[150] The state filling mechanism, however, is not directly affected by temperature change. If it can be shown that the state filling mechanism exists in the materials, this is evidence that quantum confinement is at the root of the visible photoluminescence.

3.3.1 Continuous Source Low Excitation Intensity Behavior

The first study of the excitation intensity behavior of the luminescence was done using continuous sources of both 488 nm and 355 nm excitation light. In both cases, the photoluminescence spectra were generated using the SPEX Fluorolog instrument in the MIT CMSE central facility. Figures 3-3 and 3-4 show the dependence of the integrated luminescence intensity on the excitation intensity. In both cases, it is clear that the emission intensity increases linearly with the pump intensity. This behavior is to be expected for the low excitation intensity regime. It is simply explained by the fact that as more photons

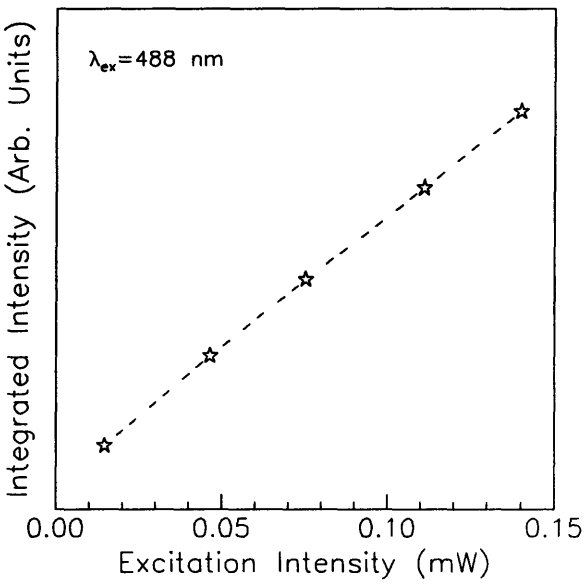

Figure 3-3: Dependence of integrated photoluminescence emission intensity on excitation intensity. Excitation source was $\lambda = 488$ nm light from Xe lamp.

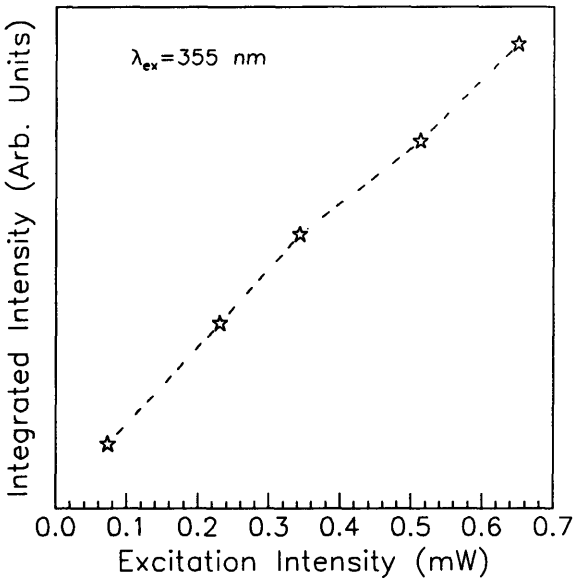

Figure 3-4: Variation of integrated photoluminescence intensity with excitation intensity. Excitation source was $\lambda = 355$ nm light from Xe lamp.

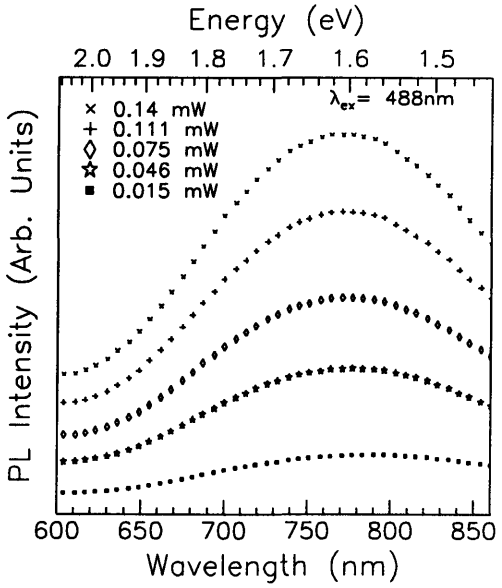

Figure 3-5: Photoluminescence spectra measured for a variety of excitation intensities. Excitation source was λ=488 nm light from Xe lamp.

are impinging on the sample, more electron-hole pairs are created and their recombination results in more photons emitted. The total number of electron-hole pairs generated at these pump levels is not sufficiently high to fill up all of the available slots in the first excited state. This number is also not high enough to increase the probability of Auger nonradiative recombination events occurring. The absence of these effects leads to a very simple linear behavior.

Figures 3-5 and 3-6 show the spectral distribution of the emissions as a function of excitation intensity for the λ=488 nm and λ=355 nm excited luminescence, respectively. It is clear that the spectral shape of the emission does not change with increasing excitation intensity for low excitation levels. This is also consistent with the generation of more electron-hole pairs with greater excitation, but the absence of more complex mechanisms such as state filling or Auger recombination. It is possible that the increased excitation in this intensity range is both generating multiple excitations in some particles and including new particles

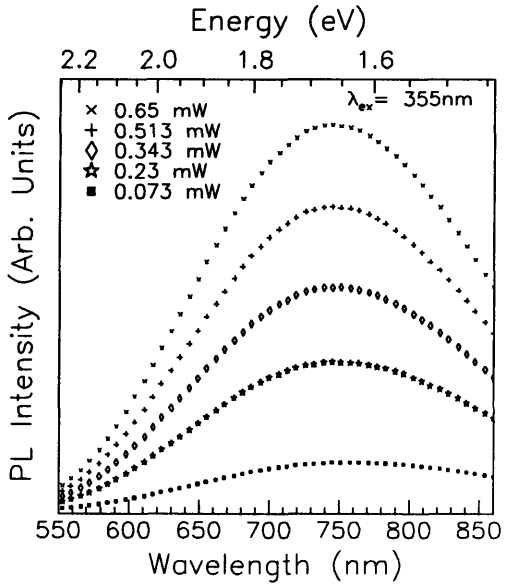

Figure 3-6: Series of photoluminescence spectra measured for different excitation intensities. Excitation source was λ=355 nm light from Xe lamp.

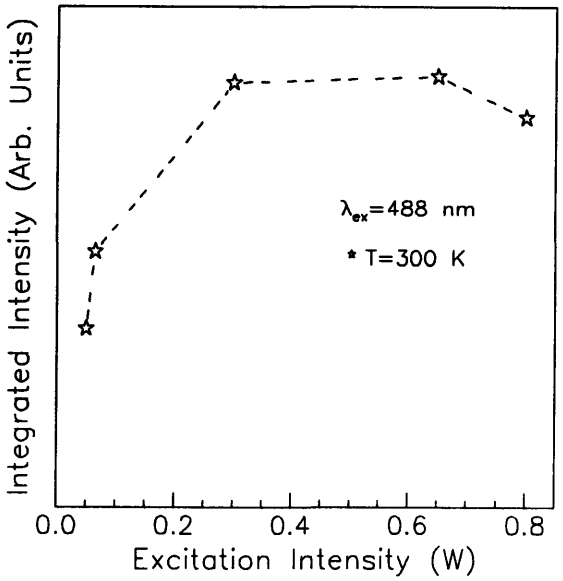

Figure 3-7: Dependence of integrated photoluminescence intensity on excitation source intensity at room temperature. Excitation source was an Ar^+ laser operating at λ =488 nm.

for which there were not sufficient photons under lower excitation levels. It is of interest to note from the similarity of the behavior of both the λ=355 nm and λ=488 nm excited samples that there appears to be no excitation wavelength dependence to the luminescence, so it is expected that the same behavior for will occur both wavelengths if the nature of the light source is altered, either by increasing the intensity or changing the temporal profile. This behavior is central to the results of the rest of the excitation intensity study.

3.3.2 Continuous Source High Excitation Intensity Behavior

To study the impact of even higher excitation intensity continuous light, photoluminescence was excited using the λ=488 nm line from an Ar^+ laser. The dependence of the integrated photoluminescence intensity on this increased excitation intensity from a continuous source is shown in Figure 3-7. At lower excitation intensity, the same linear trend reported before continues, but at high excitation intensities, the integrated luminescence emission intensity

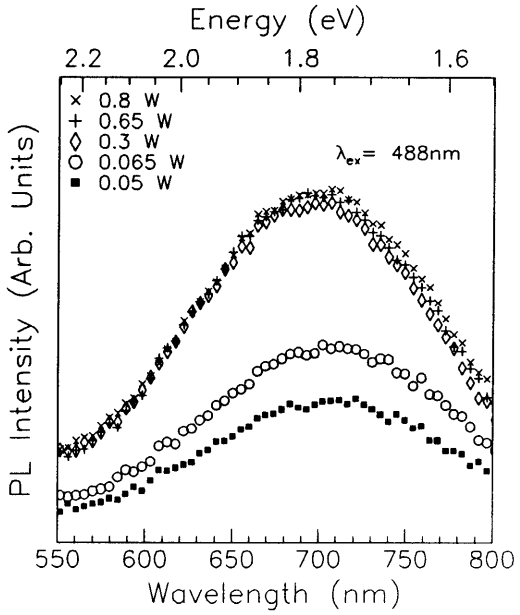

Figure 3-8: Series of room temperature photoluminescence emission spectra from a silicon nanoparticle film excited with cw λ=488 nm light of varying intensity.

saturates. This saturation is in fact spectrally uniform, as can be seen in Figure 3-8. This behavior indicates that at some threshold number of photogenerated carriers, the ability to access additional radiative recombination pathways is cut off. This is the type of behavior expected for an Auger-limited system at high excitation intensity, because in such a system at some high excitation intensity, the number of carriers will have increased to the point at which the Auger recombination mechanism suddenly has a significant probability of occurring.

This mechanism assignment can be confirmed by looking at the temperature dependence of the excitation intensity dependence of the emission. Figure 3-9 shows the integrated intensity of the photoluminescence emission as a function of excitation intensity at low temperature. Under the reduced temperature conditions, the emission intensity no longer saturates. Instead, it returns to the linear dependence observed at low excitation intensity. Figure 3-10 shows the temperature dependence of the integrated PL emission intensity for a

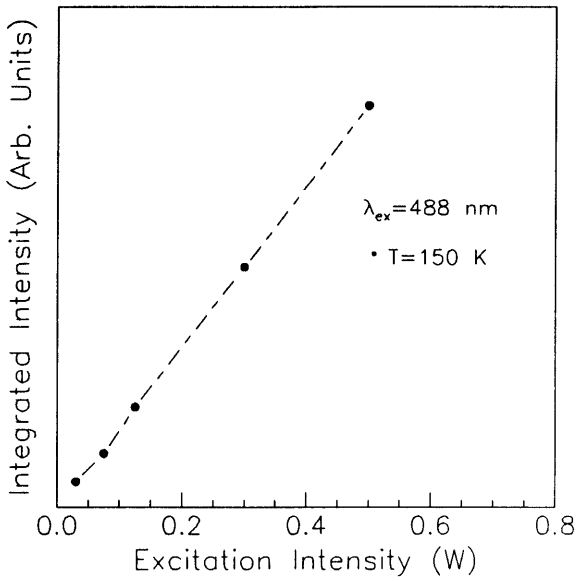

Figure 3-9: Dependence of the integrated photoluminescence intensity on excitation intensity at T=150 K. Excitation source was Ar^+ laser, λ=488 nm.

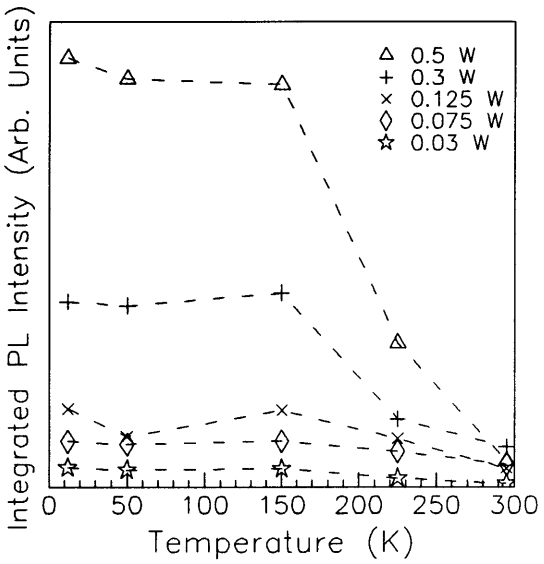

Figure 3-10: Integrated PL intensity as a function of temperature for a series of excitation intensities. Emission intensity is observed to saturate at high temperature but increases with pump intensity at low temperature. Excitation source is continuous $\lambda = 488$ nm laser.

variety of excitation intensities. The integrated emission intensity experiences a saturation phenomenon at room temperature which disappears as the temperature is reduced. The saturation at room temperature and the strong temperature dependence indicate an Auger-limited mechanism, since the Auger recombination mechanism is known to be temperature dependent. This is in stark contrast to the temperature independent behavior expected for quantum confined state filling.

One might imagine that it would be possible to use the techniques employed in Auger Electron Spectroscopy to detect whether or not Auger recombination is actually occurring under continuous excitation in the silicon nanoparticle films. Unfortunately, this is not the case. In traditional Auger Electron Spectroscopy (AES), electrons are directed onto a sample of material and the energy distribution of electrons emitted from the sample is measured.

Some of the ejected electrons are found to have energies that are characteristic of the separation between the core electronic levels of the elements contained within the sample.[151] For most elements, electrons are emitted in the range of hundreds of electron volts, for which detection techniques have been refined. In the case of photoexcited electrons in silicon nanoparticle films undergoing Auger recombination, the extra energy provided to the Auger electron in the recombination process is approximately 2 eV. The small magnitude of this energy poses detection problems in that typical AES detection systems are not designed for operation in this small energy regime. Also, it is known for bulk silicon that the electron affinity, which represents the energy required to remove an electron with energy at the conduction band edge from the material, is 4.05 eV.[152] Assuming this energy is not modified very dramatically for small silicon clusters, the extra energy provided by the Auger recombination process is not sufficient to result in the ejection of electrons from the material. Thus, even if the detection system could be modified to look for very low energy, there are not going to be any electrons to find, and it is not possible to directly observe any products of the Auger recombination process.

3.3.3 Pulsed Source High Excitation Intensity Behavior

In order to try to promote state filling limited photoluminescence, it was necessary to provide photons to the sample in a shorter period of time than is necessary for Auger recombination to occur. To achieve this, a pulsed λ=355 nm source, a 3x Nd:YAG laser operating in Q-switched mode with a pulse width of 7 nsec, was employed. Figure 3-11 shows the room temperature dependence of the integrated emission intensity on the excitation intensity from the pulsed source. Here, the integrated emission intensity initially increases linearly with pump intensity, as for the continuous λ=355 nm and λ=488 nm continuous Xe lamp sources. At higher excitation intensity, the increase in emission intensity becomes less strong than it was a low pump intensity. That is, the slope of the line decreases. This could be described as a situation in which the emission intensity is somewhat saturated, but note that the emission intensity continues to increase with increased excitation intensity, unlike what is observed for the high intensity cw excitation. More insight into this phenomenon can be gained by considering the spectral profile of this emission, as shown in Figure 3-12. As the excitation

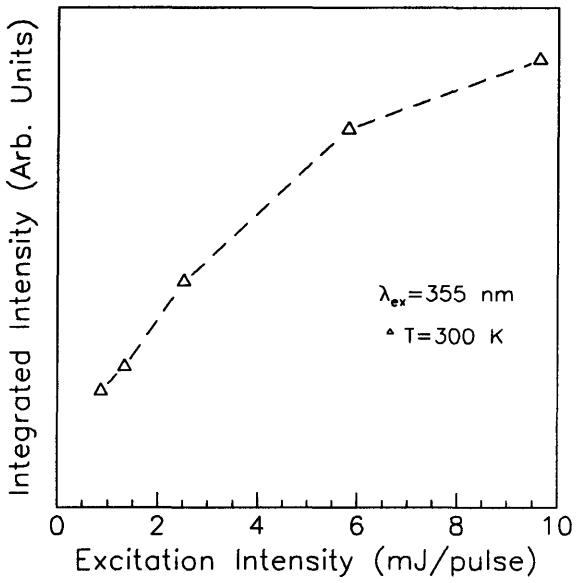

Figure 3-11: Excitation intensity dependence of integrated photoluminescence intensity at room temperature. Excitation source was a pulsed Nd:YAG laser operating at λ =355 nm.

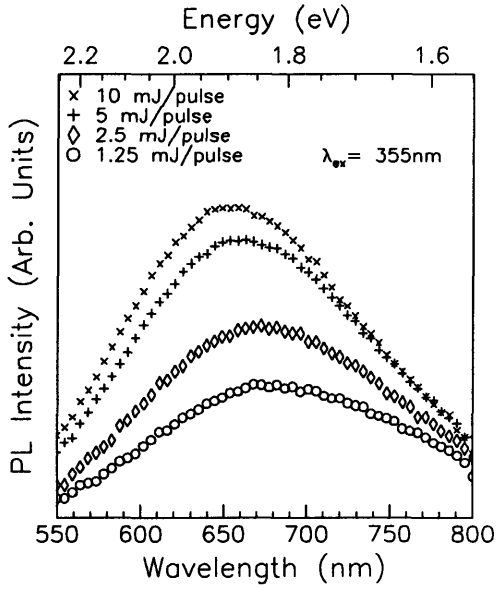

Figure 3-12: Series of room temperature photoluminescence emission spectra from a silicon nanoparticle film excited with pulsed λ=355 nm excitation light of varying intensity.

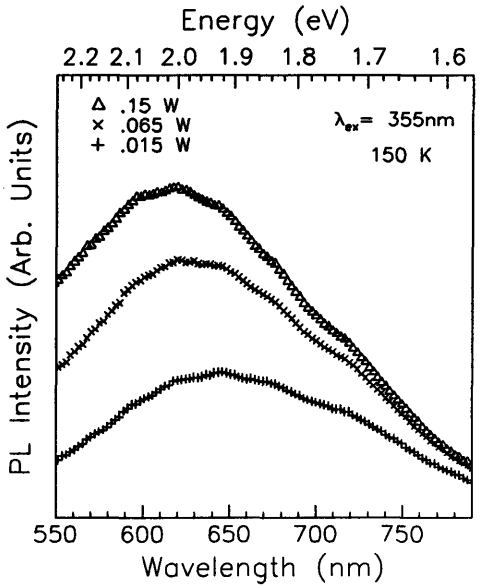

Figure 3-13: Series of photoluminescence spectra from a silicon nanoparticle film excited using a pulsed λ=355 nm excitation source of varying power. Spectra were measured from a sample at reduced temperature.

intensity is increased, the emission intensity is seen to increase as well, and the peak of the emission spectrum is found to shift to higher energy. This behavior is not consistent with Auger recombination, but is indicative of quantum confined state filling. Here, emission in the low energy portion of the spectrum is saturated because all of the lowest excited states are filled. With increased excitation, transitions begin to occur from the higher energy states, adding intensity to the higher energy portion of the spectrum. Ideally, this behavior would manifest itself in the development of completely separate peaks resulting from the different levels, but the broad size distribution of particles in these samples means that these levels will lie at different energies in different particles, which broadens the emission from each line and results in only a general shifting of the overall emission peak. The magnitude of the peak shift is consistent with the separation of energy levels in a three dimensional particle in a box model of the quantum dots, further supporting this argument.

Once again, the distinctly different temperature dependences of the recombination mechanisms can be used to confirm the mechanism assignment. Figure 3-13 shows another series of emission spectra excited by the pulsed source, this time at reduced temperature. Exactly the same behavior is observed as was the case at room temperature. The temperature independence of the excitation intensity dependence of the photoluminescence points toward a state filling mechanism, which should have no temperature dependence. The absence of a strong temperature dependence indicates that Auger recombination is not controlling under these excitation conditions. These results indicated that both Auger recombination and state filling exist in the films, with dominance of one mechanism or the other determined by the excitation conditions. The fact that state filling exists at all is evidence that the visible photoluminescence has its origin in quantum confinement.

3.4 Microstructure of Standard Films

The consistency between the observed luminescence properties and what would be expected for emission from quantum confined silicon nanostructures points to this as the origin of the emission. One piece of this puzzle is still missing, however. In order to claim that the photoluminescence is due to quantum confinement, it must be demonstrated that the light emitting species is silicon nanoparticles and that these particles are in the proper size range for quantum confinement effects to occur. To confirm this, the microstructure of the films was studied.

3.4.1 X-Ray Diffraction

Conventional geometry x-ray diffraction patterns were collected from samples on various substrates. These patterns show evidence of diffraction from atomic planes of silicon, but these peaks are obscured by diffraction from the substrate materials, be they crystalline or amorphous. To compensate for this, a glancing angle geometry was employed. A glancing angle x-ray diffraction pattern, collected from a silicon nanoparticle thin film on a niobium substrate with a glancing angle of $\alpha = 1°$, is shown in Figure 3-14. It is clear from the peaks present in the pattern that crystalline silicon exists in the film and is giving rise to

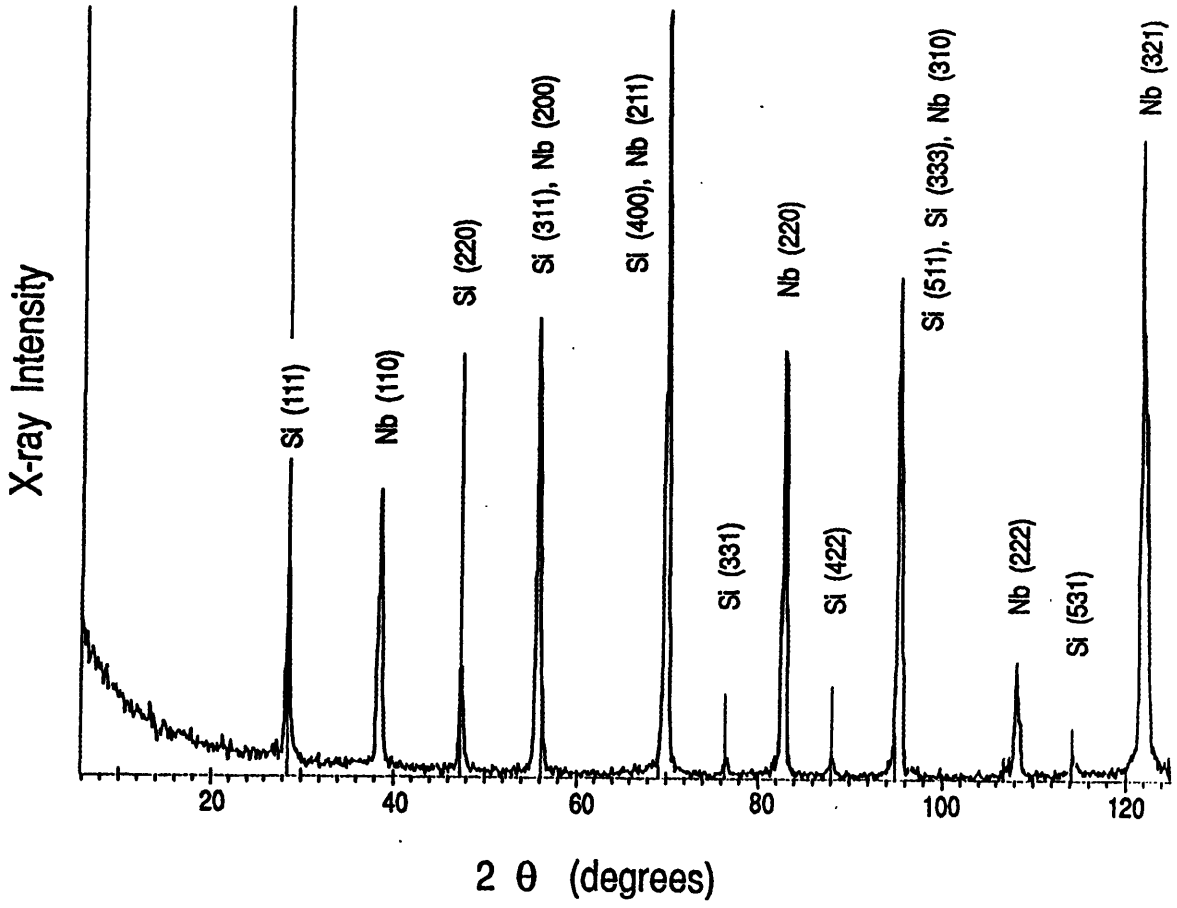

Figure 3-14: Glancing angle x-ray diffraction pattern for silicon nanoparticle film on niobium substrate. Glancing angle was $\alpha = 1°$. From Reference [114]

the diffraction. The peak widths of the silicon diffraction peaks appear to be somewhat broader than what is expected for a silicon wafer. Ordinarily, this peak broadening could be utilized to estimate the grain size for the diffracting species. Unfortunately, the glancing angle geometry does not permit the study the broadening of the peaks, as it lacks a focused x-ray beam, which is required to allow the use of the Scherer formula to compute grain size. The x-ray diffraction data indicates that crystalline silicon does exist in the films, and it appears to be coming from finite sized particles (which result in peak broadening).

3.4.2 Transmission Electron Microscopy

To fill in the gaps in microstructural information left by x-ray diffraction, transmission electron microscopy (TEM) was used to study the films at a finer scale. TEM studies of the films reveal that a wide variety of particle sizes are present in the samples. As can be seen in Figure 3-15, there are some very large particles, approximately 100 nm in diameter, some large particles approximately 50 nm in diameter, and many smaller particles in the 10 nm diameter and smaller size range. Approximately 20% of the observable particles are smaller than 5 nm in size, 50% are in the 5 to 20 nm size range, 20% are in the 20 to 50 nm size range, and 10% are greater than 50 nm in diameter. It is clear that the larger particles are crystalline from electron diffraction, as shown in Figure 3-16 and it is likely that these particles are what are producing the x-ray signal measured in XRD.

High resolution electron microscopy confirms the crystallinity of the larger particles, as shown in Figure 3-17. The microscopy samples were prepared by placing the TEM grids with support film directly in the path of the cluster beam and then removing the grid and deposited film from vacuum into the air. The samples were then placed into the microscope and studied, with no further sample preparation. It is evident that the large particles have a disordered layer at the surface, which is likely the surface oxide that developed when the particle was removed from vacuum. High resolution microscopy also allows for the imaging of even smaller particles. Figure 3-18 shows a high resolution electron micrograph of a particle approximately 3 nm in diameter. The lattice fringes resulting from the atomic planes within the nanocrystallite are clearly visible, and indexing of the planes reveals that they are Si {220}. Particles of all sizes above 3 nm were observed. It is expected that particles smaller

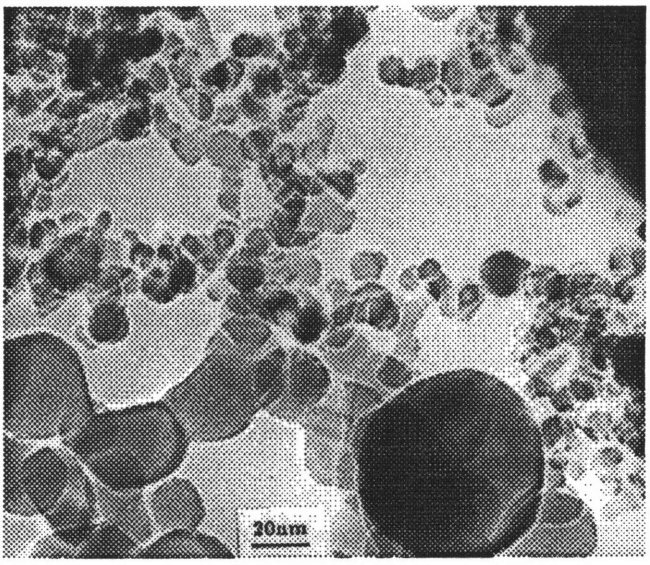

Figure 3-15: Transmission electron micrograph demonstrating the variety of particle sizes present in a silicon nanoparticle thin film.

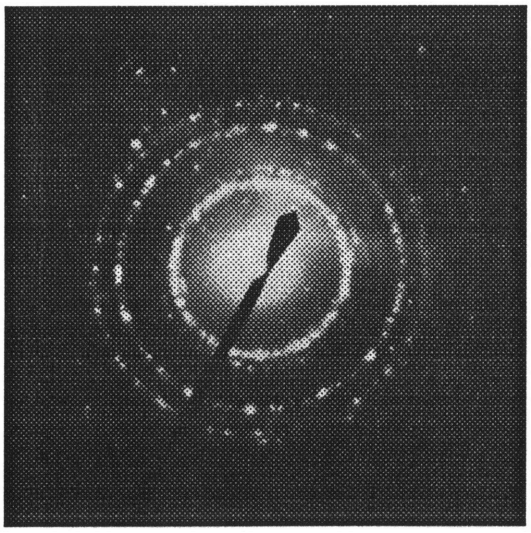

Figure 3-16: Electron diffraction pattern from an array of particles. Sharp diffraction spots indicative of crystalline material are observed. The polycrystallinity of the array turns these spots into the spotty rings that are seen.

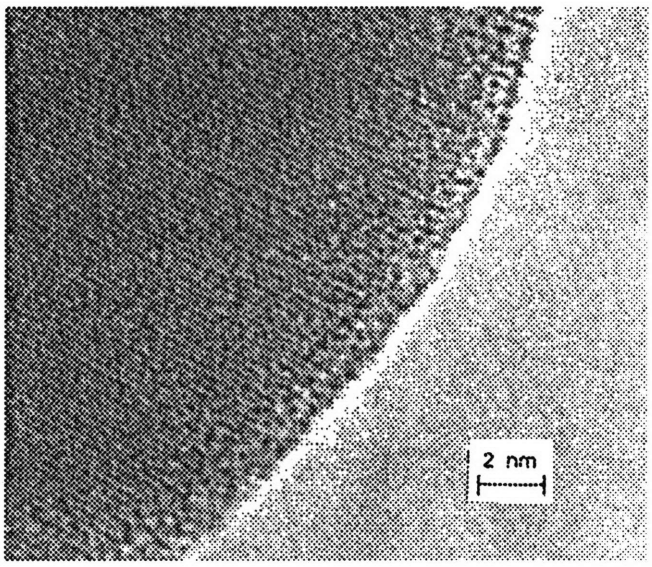

Figure 3-17: HREM image of a portion of a larger silicon nanoparticle. The particle exhibits lattice planes indicative of crystallinity, with a disordered surface region as expected for a silicon oxide layer.

than 3 nm exist, but the very weak contrast between the silicon particles and the amorphous carbon background made it difficult to image these species.

It is clear that the silicon nanoparticle films consist of crystalline particles of a range of sizes. What is not clear is if there is also any amorphous or disordered silicon also present in the films, which should be expected given the non-bulk structures expected for the very small particles generated by pulsed laser ablation supersonic expansion.

3.4.3 X-Ray Photoelectron Spectroscopy

Valence band x-ray photoelectron spectroscopy (XPS) is sensitive to chemical bonding, allowing the technique to provide structural information on a scale smaller than electron diffraction. In order to look for evidence of amorphous silicon in the silicon nanoparticle films, valence band XPS was employed. Figure 3-19 shows a valence band XPS spectrum of a film of silicon nanoparticles. There are three features in this spectrum, peaks at approximately 3, 7, and 9 eV, with the peak at 7 eV being not very pronounced and almost a shoulder on the 9 eV peak. This spectrum is similar to those observed by other researchers

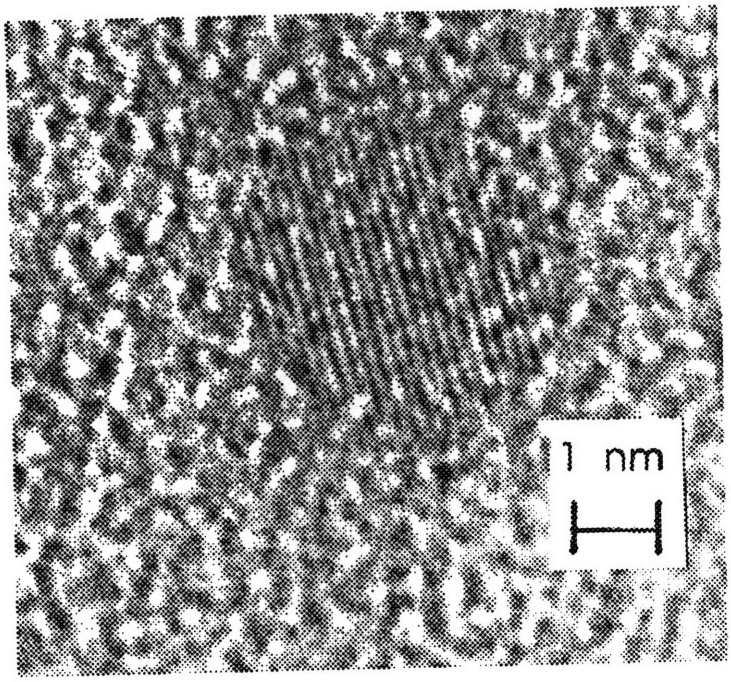

Figure 3-18: High resolution transmission electron micrograph of a ~3 nm diameter silicon nanoparticle. Lattice planes are visible whose spacing corresponds to Si {220}. From Reference [114].

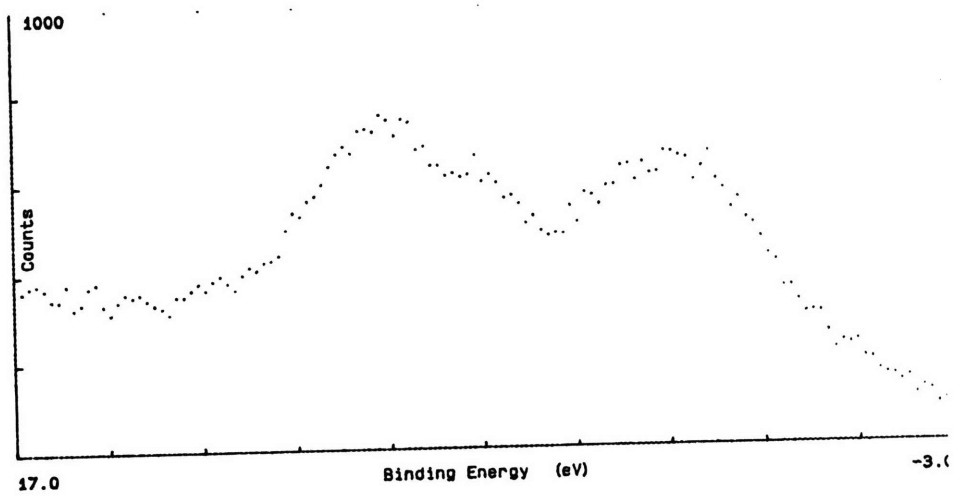

Figure 3-19: Valence band XPS spectrum of a silicon nanoparticle thin film on Teflon.

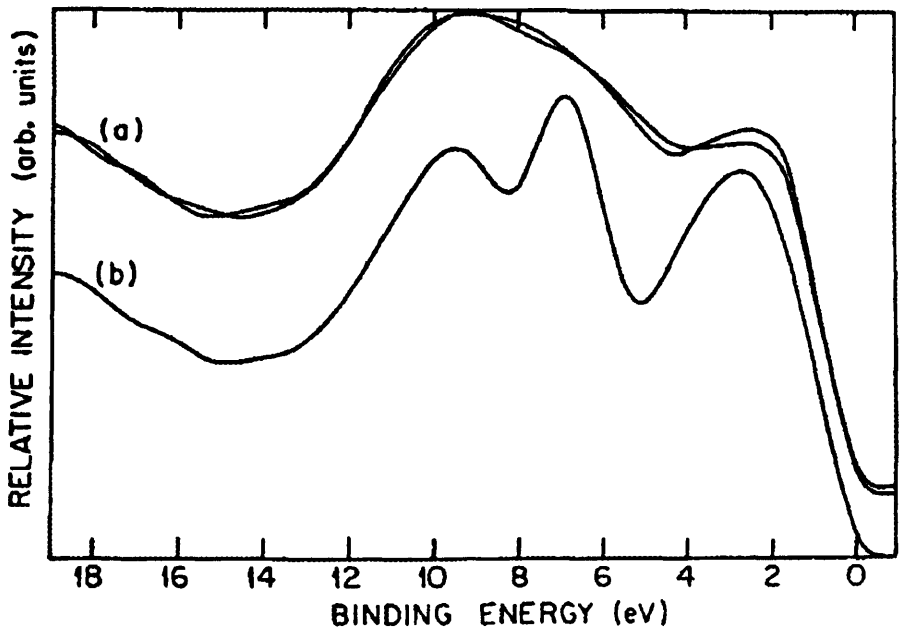

Figure 3-20: Valence band x-ray photoelectron spectra measured for (a) amorphous silicon and (b) crystalline silicon. The three distinct peaks in the crystalline spectrum become two broader peaks in the amorphous silicon spectrum. From Reference [154].

for porous silicon.[141, 153] The spectrum looks to lie in between the spectra for crystalline silicon and amorphous silicon. As shown in Figure 3-20(b), the crystalline silicon valence band XPS spectrum exhibits three very distinct peaks near 3, 7 and 10 eV. The 7 eV peak is strong, with at least as much intensity as the 10 eV peak. In the valence band XPS spectrum of amorphous silicon shown in Figure 3-20(a), the two peaks near 7 and 10 eV from the crystalline silicon spectrum become a single broad peak, with the 7 eV peak serving as a shoulder to the single peak. As can be seen in Figure 3-19, the spectrum measured from the nanoparticle film appears very similar to the spectrum observed from amorphous silicon, with slightly more definition to the 7 eV peak. For amorphous silicon, the broad peak develops due to the presence of odd-membered rings of Si atoms in addition to the six-membered rings of which the crystalline silicon is comprised.[155, 156] This can lead to two interpretations of the XPS valence band spectrum. First, it is possible that the films consist of a mixture of crystalline and amorphous silicon. The amorphous material may result from the

deposition of very small clusters, which are known to have non-bulk atomic arrangements, and somewhat larger particles which may be amorphous in structure. In this case, it is difficult to determine which material is emitting the light. Second, it is possible that the "amorphous" signal is a result of the increased surface to volume ratio for nanometer sized particles. With many atoms residing on the surface of a nanoparticle, there are likely to be numerous odd membered rings of silicon atoms. While this situation occurs in the bulk, the fraction of surface atoms is so low as to be almost insignificant. This component may become important in nanoparticles. More information is needed in order to choose between these interpretations.

3.5 Size Discriminated Films

Standard samples have been shown to contain silicon particles of various sizes, from larger (~100 nm) particles down to particles of less than 10 atoms. XPS results suggest that of both crystalline and amorphous silicon are present in the films, with the latter either in the form of the very small particles or a characterization artifact from the nanoparticle surfaces. What is not known is which of these things is responsible for the visible photoluminescence, making it impossible to confirm the quantum confinement mechanism assigned as a result of the photoluminescence studies. To succeed in doing this, the identity of the particles that are emitting the light must be determined. This can be achieved by separating out the effects of differently sized particles.

3.5.1 Photoluminescence Study of Large Particles

The photoluminescence of the larger silicon particles provided by other researchers was also studied. The luminescence of these entities can be expected to be representative of the luminescence from the larger particles in the size distribution produced by the pulsed laser ablation supersonic expansion source. As such, these particles can be used to determine whether oxide related luminescence, either through interfacial layers or defects within the oxide, is contributing to the luminescence, since particles of all sizes will have oxide layers. Both the 10 nm particle powders supplied by Dr. Castro and the 30 nm particle powders

supplied by Dr. Haggerty were found to show no visible photoluminescence whatsoever. This was true regardless of processing: samples whose oxide layer was etched and allowed to regrow as well as samples exposed to an oxidation furnace to reduce silicon core size and increase the amount of oxide were nonluminescent.

These results lead to two conclusions. First, the larger particles that are present in the samples are not making any contributions to the photoluminescence emission. Second, since the large particles are not emitting, the source of the photoluminescence is not related to the silicon oxide. These larger particles are too big to exhibit quantum confinement effects, so it is expected that they will not emit if quantum confinement causes the luminescence. The collections of large particles a high surface area and thus a large amount of oxide just as the small ones do, so if the large ones do not exhibit photoluminescence due to defects in the oxide, it is unlikely that the small ones will. Having thus "separated out" the large particles from the ensemble of possible light emitters, the photoluminescent species still has not been identified. There is no similar simple approach to "separate out" the smaller particles in the films. To do this, particles of different sizes must actually be physically separated.

3.5.2 Mechanical Velocity Selection

The first approach to size selection that was pursued was a mechanical velocity selector, as described in Section 2.2.1. Two approaches were discussed, a single mechanical barrier introduced into the middle of the cluster packet and a dual barrier system to chop from both ends of the packet. Figure 3-21 plots the photoluminescence from a film deposited beyond a single chopper wheel and the corresponding control sample, which was deposited without any chopping. The emission spectra from these films are very similar in appearance. Figure 3-22 shows the photoluminescence emission spectrum measured for a sample deposited from particles which passed through both chopper wheels of the mechanical velocity selector and from a control sample deposited at the same time but away from the wheels. This emission spectrum is typical of the emission observed from all of the "chopped" samples. Comparison of the photoluminescence spectra for the chopped and unchopped films reveals that for both chopping schemes, the chopped and unchopped emissions look basically alike. This behavior is typical of all of the films deposited using the mechanical chopping wheels, regardless of

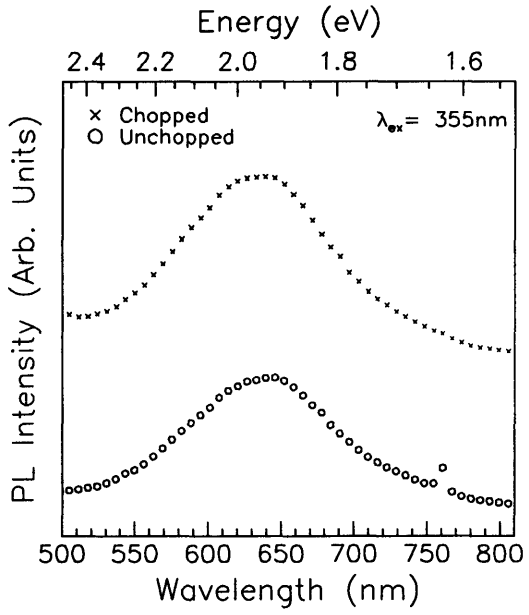

Figure 3-21: Photoluminescence spectra from a sample deposited using a single wheel chopping scheme and from an unchopped sample. The top spectrum is offset for clarity.

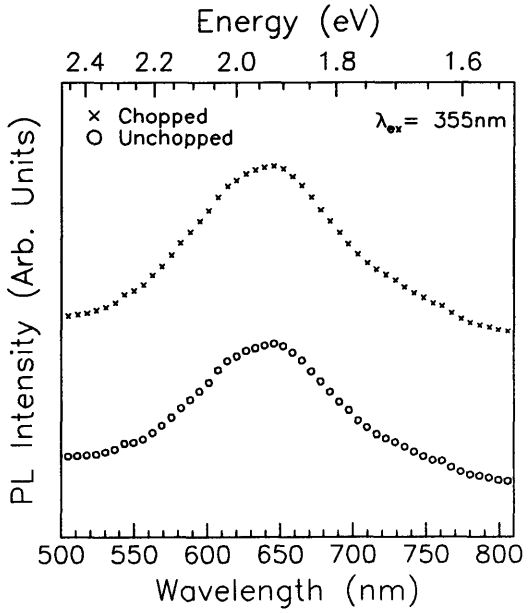

Figure 3-22: Photoluminescence spectra from a film deposited using the two chopper wheel size selection scheme and from an unchopped sample. The top spectrum is offset for clarity.

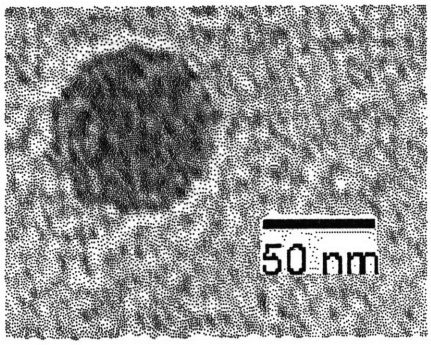

Figure 3-23: TEM micrograph of a silicon nanoparticle deposited through the mechanical velocity selecting chopper wheels.

the wheel settings (i.e. direction of wheel motion, timing of wheel positions with respect to ablation). The spectral shifting expected for films consisting of quantum confined light emitters of different sizes is absent. This suggests that either the light emission is independent of particle size or the mechanical velocity selector is not separating out particles by size.

Transmission electron microscopy was employed to answer this question. Figure [?] shows a TEM micrograph of a particle deposited into a film after traversing both of the mechanical chopper wheels. The deposition conditions were chosen so that the wheels should chop out the largest particles in the size distribution. It is clear from the size of the particles present in the chopped films that size discrimination did not occur.

One reason that may have led to the failure of the chopper wheels is the inability to introduce the barrier fast enough to achieve chopping. The supersonic expansion produces clusters with very high velocity, necessitating very high rotation rates for the wheels in order to move the blade edge through the cluster packet before it had completely passed through. Recall that the fastest clusters were moving at 2100 m/s and the slowest were moving at 1600 m/s. It takes a chopper wheel turning at a rate of 100 Hz a time of 28 μsec to rotate 1°, which represents a total distance of 0.4 mm. During this time interval, the slowest clusters can travel 4.5 cm. The wheel thickness is 0.02 inch, or 0.5 mm. It is evident that during the time that it takes for the wheel to turn 1°, the clusters have long since moved beyond the chopper wheel. This means that it is impossible for the chopper wheel to perform any size selection. Even if the distance that the wheel must move is reduced, it is very difficult to

catch the clusters before they travel far down the beamline. Only for wheel motions on the order of the particle size, in the range of hundreds of nanometers of total wheel displacement, is it possible to move the wheel in place before the entire cluster packet has passed the wheel by. This is true for even the highest wheel turning rates that the motors used could achieve.

Even in the case of the wheel displacements of only nanometers, in which it should be possible to place the barrier within the cluster packet, experimental limitations made size based chopping impossible. Due to the dynamic process of keeping the wheels electronically locked and turning at the same speed, there were some variations between each ablation event. The first wheel was capable of turning at a somewhat faster or slower rate, which led to some variation. This fluctuation was small, however, in comparison to the changes in "phase" between the first and second wheels. The lockin amplifier constantly varied the drive voltage to the second wheel in order to keep the wheels locked together. This slight fluctuation resulted in changes in the relative positions of the chopping holes on both wheels. This "jitter" in the second wheel was on the order of 20 μsec. That is, the edge of the chopping hole on the second wheel was found to reach the beamline at a different time for each ablation pulse, and in some cases the difference was as much as 20 μsec for different laser pulses. It was just shown that in this time period, the clusters can travel more than 4 cm. Thus, the variation in chopper blade position as a result of the jitter in the second wheel renders it useless for size selection. For some ablation pulses, the wheel will allow all clusters to pass, while for others it may allow none. This situation could explain the TEM observation of large particles in numbers far smaller than those found in unchopped samples. Numerous attempts were made to try to reduce the system jitter, but all were unsuccessful and eventually, this approach was abandoned.

3.5.3 Gas Jet Particle Deflection

The first attempt to capitalize on particle separation resulting from collisions with helium gas failed, so a second attempt exploit this phenomenon in another way was made by using the crossed gas jet approach. Unfortunately, the photoluminescence of the crossed gas jet deposited samples showed no deviations from that observed from a standard film. This approach failed either due to the independence of luminescence on particle size or the failure

of the approach to achieve sufficient size separation to observe the changes. The latter explanation is quite likely due to a number of experimental limitations. The gas jet employed was not operated at nearly as high a pressure as the cluster source gas jet, so it is likely that the helium atoms did not have sufficient momentum to transfer to the silicon clusters upon collision. The pressure used was limited by the experimental setup, which prevented the introduction of large amounts of gas due to the maximum pumping speed of the diffusion pump evacuating the primary chamber. This limitation was also likely to have resulted in an insufficient number of helium atoms being present to undergo collisions with the clusters to achieve size separation. The maximum possible separation of clusters on the substrate was limited by the dimensions of the vacuum chamber. Since the helium atoms impart momentum perpendicular to the cluster beam to the clusters, the clusters will move off the beamline with velocities related to their mass. Given a large distance to travel along the beamline, or consequently a longer time to move off of the beamline, a large cluster separation could be achieved. The vacuum system is finite in size, however, and the separation of the clusters is limited by its dimensions. It is possible that the chamber was not large enough to allow the clusters to separate by size on a length scale that could be observed experimentally.

3.5.4 Radiation Pressure Based Particle Deflection

It was of interest to employ this same principle of imparting momentum perpendicular to the cluster travel in a means that could circumvent some of the experimental limitations of the gas jet approach. To do this, laser light was used to knock the clusters off the beamline. As observed for the gas jet deflection experiments, however, the photoluminescence spectra of these samples were no different from those from typical nanoparticle films. Once again, this behavior may be due to particle size insensitivity of the luminescence or due to experimental limitations. The size of the chamber remains a problem, as particles knocked off of the beamline may not be able to separate by size far enough for the differences in luminescence behavior to be seen before they are deposited. The output power from the HeNe laser is also a limiting factor. The output power reflects the number of photons delivered to the beamline. If the laser used, which was not designed for high power applications, could not provide enough photons to interact with all of the clusters then no size-dependent knockout

could have been achieved. The operating wavelength is also an important factor. If the particles do not absorb the photons impinging upon them, then no momentum transfer will occur. The HeNe laser was chosen because it has a wavelength of $\lambda = 633$ nm, a wavelength that lies within the photoluminescence emission spectrum of the silicon nanoparticles. This may not represent the most efficient wavelength for absorption in the particles, which would reduce the effectiveness of the experiment.

3.5.5 Quadrupole Mass Filter Based Size Discrimination

The final attempt at mass selection applied a technique that others have used successfully in the past to size separate silicon nanoparticles formed by pulsed laser ablation supersonic expansion. A quadrupole mass filter was placed in the cluster beam path and a substrate was placed beyond the quadrupole in order to synthesize films of size selected silicon particles. The idea behind this experiment was to tune the quadrupole to a particular mass corresponding to a particle containing a specific number of silicon atoms and deposit a film with only those particles being allowed to pass through the filter. The mass chosen was to be varied and samples containing a series of particle sizes deposited. The photoluminescence from these single size particle samples would then be studied. This would permit the separation of each different size of particle and the study of the emission from that species, so that the relationship between cluster size and film photoluminescence could be determined.

3.6 Size Selected Films Using Quadrupole Mass Filter

It was not possible to carry out the initially proposed quadrupole filter experiment for a variety of reasons. First, it was determined that the maximum mass that the quadrupole could be tuned to allow to pass was Si_{10}. This range did not permit the study of films of singly sized particles in the size range of $\sim$3 nm ($\sim$700 atoms), which was of particular interest as suggested by theories of quantum confinement in silicon nanoparticles. It was, however, sufficient to study the role of the very small particles having non-bulk structure in the visible photoluminescence. If films deposited from these clusters were to emit light, then it would be obvious that these amorphous silicon nanostructure are the source of the

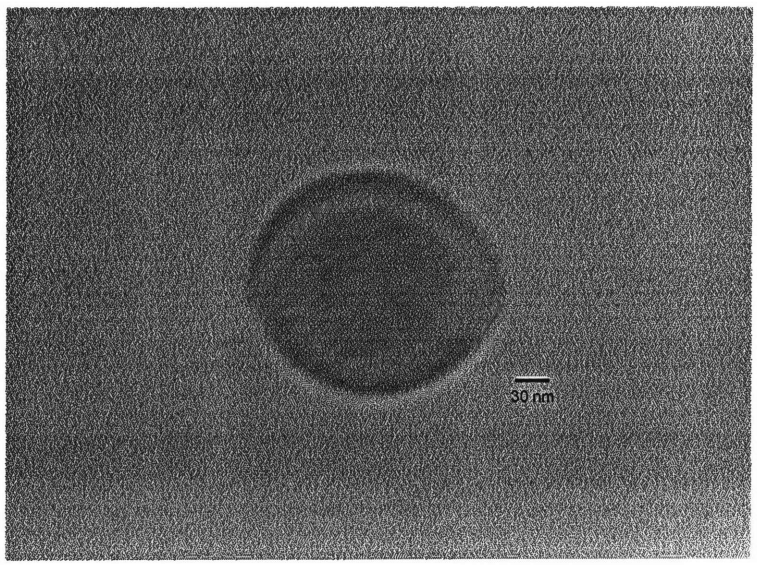

Figure 3-24: TEM micrograph of a silicon nanoparticle deposited through the quadrupole mass filter.

emission. If samples of only these clusters do not emit, then the very small clusters play no role in the emission. Samples were deposited under experimental conditions in which clusters in the size range Si_5-Si_{10} were deposited onto substrates.

3.6.1 TEM Characterization

Upon examination of the quadrupole deposited films in the transmission electron microscope, it was found that the films contained not only the small clusters to which the quadrupole was tuned, but also large silicon particles. An example of one of these large particles is shown in Figure 3-24. This particle was deposited while the quadrupole mass filter was tuned to allow only Si_8 to pass. It is clear that this particle is not one to which the filter was tuned. Particles were observed with a range of sizes, all of which were larger than what was expected to pass through the filter.

When it was discovered that these particles were deposited in the films, two possible explanations were considered. First, the particles might be the result of agglomeration of the very small amorphous clusters after their deposition on the electron microscope grid. Similar behavior has been observed previously.[75] Second, the larger particles were somehow making

their way through the mass filter despite the impact of the electric fields on their trajectory. The first theory would likely have resulted in large amorphous particles being present in the film. Electron diffraction measurements on these particles revealed that they were crystalline, which served to lend more credence to the second theory, although it is possible that the particles were crystallized by the energy provided by the electron beam. There were, however, no observations of any changes in the appearance of the clusters or in the appearance of the diffraction patterns, which would indicate that electron beam crystallization did not occur. The presence of these large particles in films deposited with the mass filter tuned to a value that was not equal to the mass of any cluster of silicon atoms also suggests that the large features are not agglomerations but are survivors of the quadrupole despite their size.

The quadrupole selected samples were also studied using dark field transmission electron microscopy. In the case of crystalline particles, particular diffracted beams were selected for the generation of dark field images. When generating images using the diffracted beam, the regions of the sample in which the crystal planes resulting in that diffraction exist will appear bright, while regions which do not have those crystal planes aligned to the beam appear as dark. Thus, crystalline particles responsible for the diffracted beam were observed as bright spots on a darker background. Large (>50 nm) particles were easily observed to be "lit up" using this dark field imaging approach. To search for the presence of amorphous particles, the diffracted "beam" selected was the amorphous ring observed in the diffraction pattern from a region of the sample in which no distinct particles were visible. The dark field images produced using the amorphous ring diffracted beam were found to have uniform intensity throughout. This indicates that there are not small, localized amorphous regions, in the form of amorphous particles, that are producing this diffraction, and that all of the amorphous material present is in the form of the amorphous carbon support film. To confirm that the analysis was being performed correctly, a dark field image using the rings was measured in a region having a tear in the support film. In this case, the region of the hole was observed to be black, lacking any diffracted beam intensity, while the amorphous film has some intensity which is uniform across the sample. This means that the experiment was performed correctly, but that there was nothing to be seen. The uniform intensity under dark field imaging was observed up to magnifications of 650,000×. The absence of bright regions when using the

amorphous rings to generate dark field images means that either there are no amorphous particles present or that the experiment lacked the beam brightness and resolution to view them. The absence of amorphous particles was expected due to the absence of any diffraction rings having the spacings expected for the radial distribution function of amorphous silicon.

3.6.2 STEM Characterization

In order to decide if the films containing large particles were built up from agglomeration of small particles, scanning transmission electron microscopy (STEM) was enlisted. STEM was able to reveal the composition of the film as a whole. If it was found that the large particles consisted of silicon and there was no other silicon in the film, then it could be concluded that all of the small clusters had agglomerated to form the large features. If silicon remained distributed throughout the film, then it was likely that the larger clusters had been deposited through the quadrupole filter. Figure 3-25 shows a scanning transmission electron microscope (STEM) image of a region of the sample in which no large particles were observed. Also shown is an x-ray map of the region which records the concentration profile of silicon within this area of the sample. Note that nearby this region, although not pictured in the image or the x-ray map, large silicon particles were observed. It is clear from this sample that silicon is present in regions of the sample that do not have large particles. Thus, the large particles are not a product of all of the small clusters coalescing. Regions of silicon concentration on the scale of 3-10 nm are present in the x-ray map, which represent silicon nanoparticles that are present in the films. The size of these features roughly correlates with what would be necessary to observe quantum confinement effects in silicon, indicating that these features could be the source of the luminescence. To arrive at a conclusion regarding this, the sizes of the particles that make up the quadrupole selected films must be more fully characterized.

3.6.3 Impact of Particle Velocity on Quadrupole Performance

It is clear that in this application the quadrupole mass filter is not operating in the way it was designed to operate. The key to this difference is in the initial conditions of the particles. A quadrupole mass filter is designed to operate on an ion with a small velocity

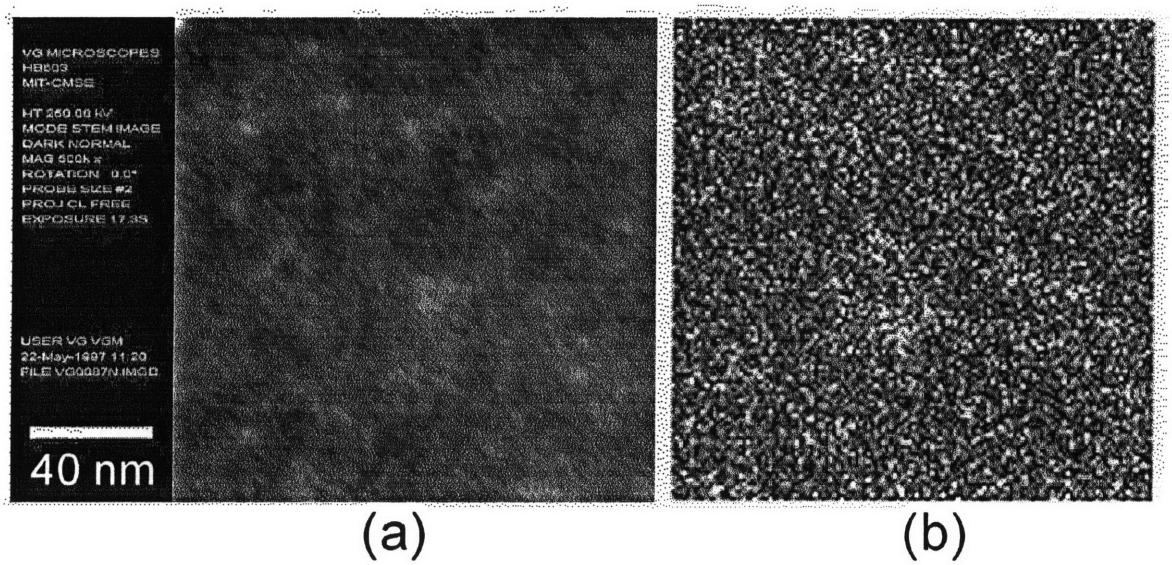

Figure 3-25: STEM image (a) of a quadrupole selected sample. Not many features are present at this scale. Silicon X-ray map of the same region (b), revealing a distribution of sililcon throughout in 3-10 nm sized regions.

directed along the axis of the filter. As the ion migrates into the region of space over which the electric field of the filter acts, its trajectory is altered by the attraction or repulsion it feels. The path of particles having mass smaller than that to which the mass is tuned is mainly determined by the R.F. component of the voltage. When these particles enter the quadrupole, they begin to wildly oscillate off of the quadrupole axis, eventually colliding with the poles. The path of particles larger than the mass to which the filter is tuned is mainly determined by the D.C. component of the voltage. These particles will begin to drift toward one pole as they progress through the filter, eventually colliding with the pole. This is illustrated schematically in Figure 3-26. It is clear from the figure that, for a given mass, ions with greater kinetic energy, or axial velocity, can proceed further down the quadrupole filter before colliding with the poles. In the event that the kinetic energy is large enough, it is even possible for large particles, whose mass is not that to which the filter is tuned, to pass through the quadrupole entirely. This is a consequence of the fact that the quadrupole fields do not have sufficient time to act upon the particles and knock them off of the filter axis.

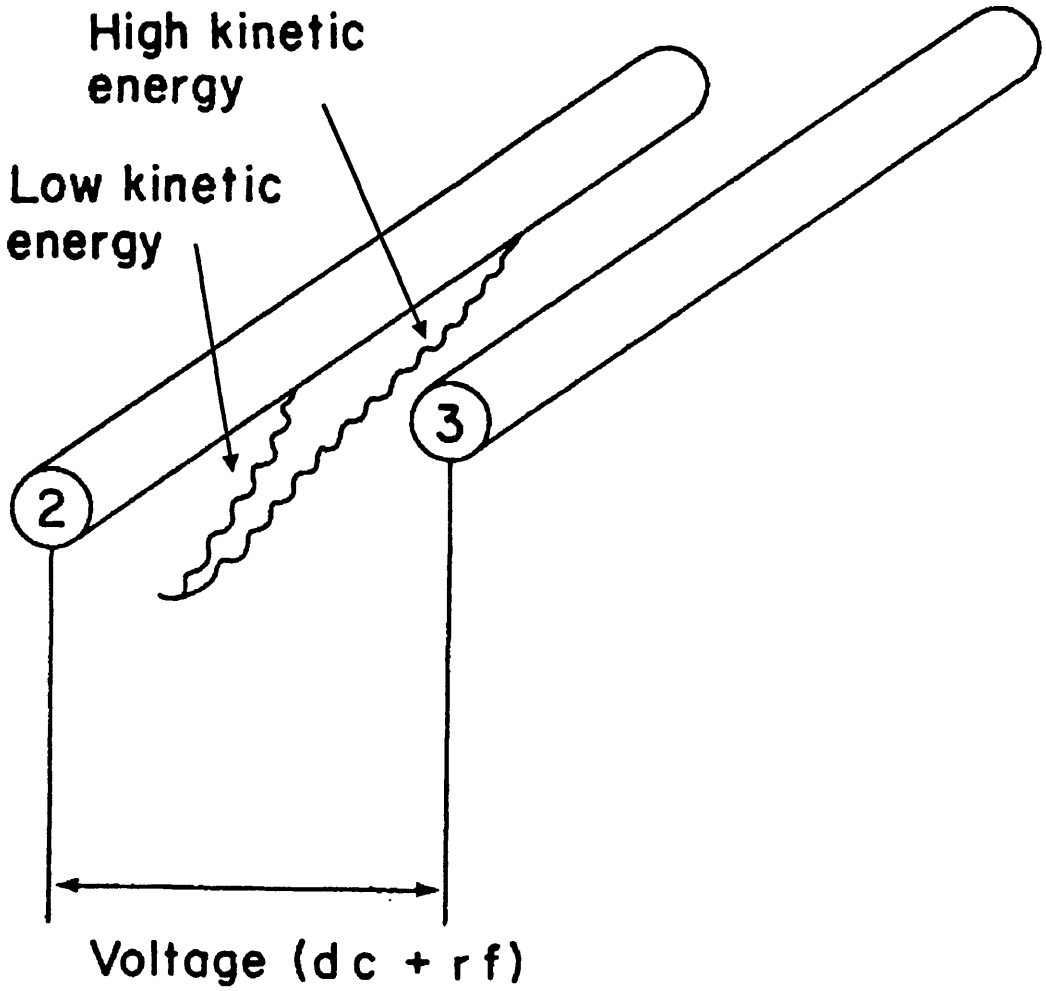

Figure 3-26: Impact of initial axial kinetic energy or velocity on the path taken by an ion in a quadrupole mass filter. With sufficient kinetic energy, it is possible for an ion to pass through the filter despite the fact that it is not of the mass to which the filter is tuned. From Reference [138].

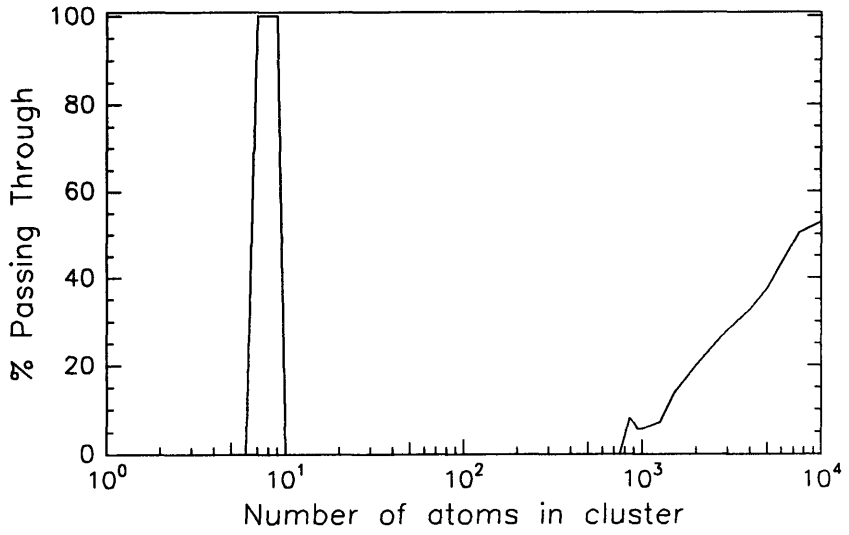

Figure 3-27: Plot of percentage of ions of a given mass that are capable of passing through the quadrupole as a function of mass. These results were obtained using the SIMION ion optics modeling software, configured for the experimental conditions with a quadrupole tuned to Si_8.

In Section 2.1.1, it was noted that the silicon particles synthesized by pulsed laser ablation supersonic expansion have a large velocity along the cluster beamline, which is coincident with the quadrupole axis. This velocity is large enough to allow particles in a certain size range to pass through the quadrupole regardless of the mass to which it is tuned. To determine which sizes are capable of making it through the quadrupole, the motion of ions through the quadrupole was modeled using SIMION, an ion optics modeling program.

Figure 3-27 plots the results of the ion motion modeling. The percentage of particles of a given size that can pass through the quadrupole is plotted as a function of particle size. The ion pathways were calculated for ions having the kinetic energy determined by the experimentally measured particle velocity and the particle mass. The calculation was performed for a quadrupole set to allow Si_8 clusters to pass. The model predicts the expected passage of the clusters to whose mass the quadrupole was tuned. The figure was computed using 85% mass tuning, which also allows Si_7 and Si_9 clusters to pass. As the resolution setting is

increased, only ions of the mass to which the quadrupole is tuned can pass. For the highest resolution setting, no small clusters can pass through the filter. Visibly photoluminescent samples were deposited under experimental conditions in which no small clusters were allowed to pass. The modeling also demonstrates that for silicon clusters having approximately 750 atoms, some clusters are able to pass through the filter. The percentage of clusters which can pass increases as the cluster mass increases above this value. No clusters with fewer than 750 atoms are capable of passing through the filter, despite their nonzero velocity. Clusters containing 750 or more atoms are approximately 3 nm in diameter and larger.

3.6.4 Photoluminescence Properties

If quantum confinement effects are producing the visible photoluminescence from silicon nanoparticle films, it should be possible to predict the impact of the omission of particles smaller than 750 atoms on the luminescence spectrum. The energy of emissions that are excluded from the luminescence can be predicted using a model of size dependence of the energy gap in silicon nanoparticles. Figure 3-28 shows the results of a calculation of energy gap as a function of size for silicon nanoparticles, including both particle size in nanometers and number of silicon atoms per cluster. It is evident that for silicon particles in the size range known to be present in the quadrupole selected films, the energy gap in the particles, which determines the emission wavelength, is coincident with the wavelength of the photoluminescence spectrum measured.

The energy gap predicted for 750 atom particles, which are approximately 3 nm in diameter, is ~2.2 eV. By omitting all particles smaller than this, the light emission at energies of 2.2 eV and higher should also be eliminated from the spectrum. The small fraction of particles that are able to pass through the quadrupole at the small end of the size range allowed to pass, as shown in Figure 3-27, will also mean that the intensity in the higher energy portion of the spectrum (>2 eV) will be diminished to a greater extent than that in the lower energy portion of the emission spectrum.

Figure 3-29 plots the photoluminescence emission spectra from both a quadrupole mass selected sample and a control sample deposited at the same time in the primary chamber. Comparison of these luminescence spectra shows that the emission from the quadrupole

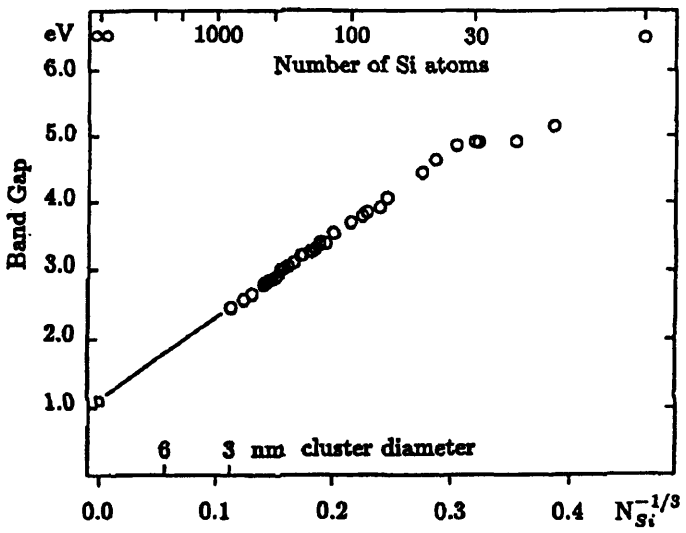

Figure 3-28: Variation of energy gap in silicon nanoparticles as a function of size, showing particle size in nm and in number of atoms. From Reference [16].

selected film looks similar to that from a non-size selected film, with the exception of a reduction in intensity at the high energy portion of the spectrum. This is consistent with the idea that light emission results from quantum confinement effects. The observation of photoluminescence from films with all particles smaller than 750 atoms rules out the role of small amorphous particles in the PL. The high energy cutoff of the emission at ~2.15 eV is at the energy predict by the quantum confinement model for a film containing only particles of more than 750 atoms. The presence of particles having the necessary dimensions for quantum confinement and the fact that the emission occurs at the wavelength predicted for these particles leads to the conclusion that quantum confinement effects are responsible for the light emission from the silicon nanoparticle films. Thus, three of the four theories that have been proposed for the photoluminescence for silicon materials can now be excluded. The observation of no luminescence from large oxidized particles coupled with photoluminescence from particles in HF rules out the oxide defect mechanism for luminescence, and the unimportance of the smallest particles in the luminescence from the films eliminates amorphous silicon as a source of light emission. The particle size and wavelength data, coupled with the excitation intensity dependence of the photoluminescence, rules out the surface state model.

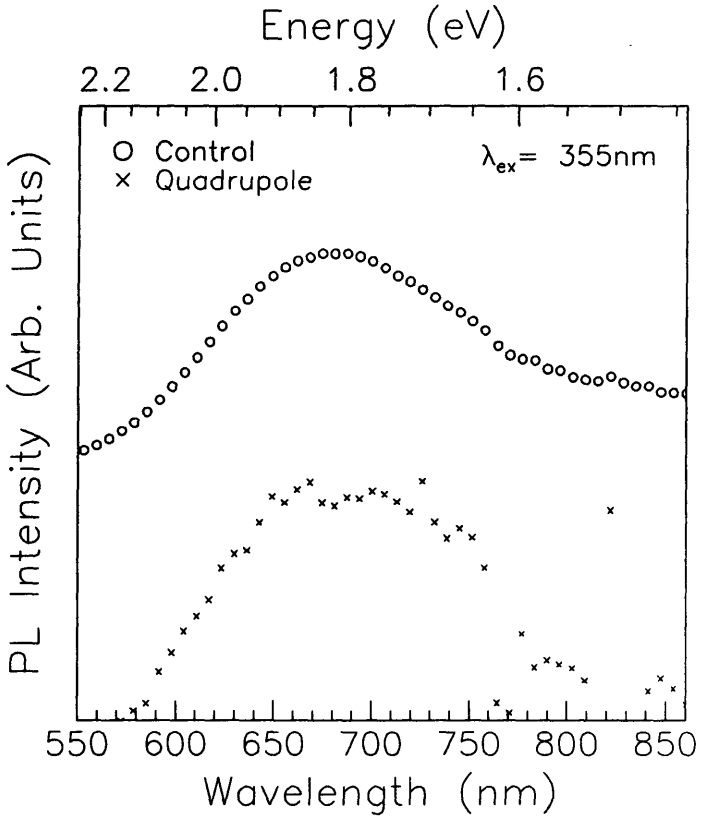

Figure 3-29: Photoluminescence emission spectra from both a quadrupole mass selected film and a control film deposited at the same time. Excitation source was a cw Xe lamp operating at $\lambda = 355$ nm.

This leaves the conclusion that the visible photoluminescence from silicon nanoparticles is a result of quantum confinement effects.

Chapter 4

Conclusions

A pulsed laser ablation supersonic expansion source was used to synthesize thin films of silicon nanoparticles. These films were found to exhibit efficient visible photoluminescence, similar to that observed from porous silicon and silicon nanoparticles synthesized by other techniques. There has been much debate about the origin of this photoluminescence. The goal of this document was to identify the origin of the emission. To do this, the microstructure of the films was studied using TEM, XRD, and STEM. Attempts were made to deposit films of different sized particles using mechanical velocity selection, deflection of particles by light or gas jet, and a quadrupole mass filter. The photoluminescence properties of these films and standard films were studied. The intensity and temporal nature of the light sources were varied in order to probe the luminescence mechanism. Through these studies, it was determined that quantum confinement effects are responsible for the visible photoluminescence from silicon nanoparticles.

The observation of visible photoluminescence from silicon nanostructures has opened a wide range of possibilities for new display technologies, optical interconnects, and photonic materials. In order to truly exploit these materials, it is necessary to understand the mechanism of light emission and the identity of the luminescing species. Wide ranging and conflicting observations of luminescence behaviors from porous silicon and silicon nanoparticles have prevented the research community from making any definitive statements of what is causing the luminescence. In this study, it was found that quantum confinement, the original motivation for studying the light emitting behavior of silicon nanostructures, gives

rise to the luminescence.

Through the study of large (10+ nm diameter) oxidized silicon nanoparticles, it was shown that these particles show no visible photoluminescence. The proposed mechanism of luminescence through oxide defects should result in photoluminescence from these particles. As a result, this mechanism can be ruled out as the origin of the light emission.

Deposition of silicon nanoparticle thin films using a quadrupole mass filter to exclude the smallest, amorphous-like particles allowed for the study of the role of these particles in the luminescence. It was found that films lacking the smallest particles exhibit the same luminescence as films containing the entire particle ensemble. This is evidence that the small, non-bulk particles are not responsible for the luminescence. From this, the proposal that amorphous silicon is the light emitting species in porous silicon and silicon nanoparticle films can be ruled out.

This leaves only two mechanisms, either a pure quantum confinement mechanism or a smart quantum confinement/surface state mechanism. Strong evidence has been produced by our group which indicates that the luminescence emission wavelength is dependent on particle size, as varied by chemical processing steps.[121] As the particles are allowed to oxidize after deposition, the photoluminescence spectrum shifts to the blue. The magnitude of the shift is consistent with that predicted by quantum confinement for the reduction in size resulting from the continued oxidation of the particles. If this oxide is removed chemically and then a new oxide is allowed to regrow, the emission shifts further toward higher energy. The magnitude of this shift is also consistent with the shift expected for the particle size change resulting from the growth of a new oxide layer. This size dependence of the emission points toward a simple quantum confinement model of luminescence. The differences between these two models are less an issue of mechanism as they are a question of the luminescence pathway.

By changing the nature of the excitation source and observing the dependence of the luminescence on sample temperature, the light emission pathway in silicon nanoparticle films was determined. At low excitation intensity, the luminescence intensity was found to increase with excitation intensity, as expected. At higher intensity excitation from a continuous source, the luminescence intensity was found to saturate uniformly with increasing

excitation intensity. This saturation disappeared with reduction of the sample temperature. Under high intensity pulsed excitation, a shift of the peak luminescence wavelength to higher energy was observed. This phenomenon persisted at low temperature. The continuous source behavior is consistent with what is expected when Auger non-radiative recombination dominates the recombination process. The pulsed behavior resembles that observed for state filling in quantum confined semiconductor nanostructures. The existence of the state filling mechanism in these materials indicates that quantum confinement is indeed responsible for the photoluminescence.

In summary, it was demonstrated that quantum confinement effects are responsible for the visible photoluminescence from silicon nanoparticles. While this theory was the original motivation for studying the emission properties of nanostructured silicon, there has been doubt as to whether this mechanism is truly active. The work herein demonstrates conclusively that it is.

4.1 Proposed Work

While much as been done in the study of light emitting silicon materials, there are still many questions to be answered and boundaries to push outward. Several areas are of particular interest.

4.1.1 Luminescence Lifetime Measurements

It is possible to further characterize the luminescence recombination mechanism by studying the time dependence of the luminescence signal. This information will have significant ramifications for applications of these materials in light emitting devices, which may need to be switched on and off very rapidly. The luminescence lifetime can also reveal more information about the recombination mechanisms. As mentioned in the discussion of porous silicon, emissions in both the blue and red portions of the spectrum have been observed. By comparing the lifetimes of these different emissions, it should be possible to assign them to either similar or different origins and to identify these origins.

4.1.2 Nonlinear Optical Response

One of the other potential applications of silicon quantum dots is in the area of photonic materials. Saturable absorption behavior would be useful for all optical switching, which would eliminate the need for electronic signal switching. This would greatly enhance the information carrying capacity of telecommunication systems. To determine if silicon quantum dots are capable of performing the task, their nonlinear optical response must be monitored. Some brief work has been done in this area [121], but more needs to be done. In particular, it is of interest to look for nonresonant nonlinear optical effects using degenerate four wave mixing. Also, for direct application to potential optical switching, the absorption behavior at higher incident powers should be studied to determine if an absorption saturation occurs.

4.1.3 Quantum Dot Heterostructures

Other work has pointed to the critical role of particle surface in the emission behavior.[121] Presently, the particle surface passivated by a native oxide layer upon removal from vacuum. Some experimental results have pointed to the presence of either amorphous material or disordered material at the surfaces of the clusters. This disorder is likely to be preserved upon oxidation of the particles. If, however, the particles are co-grown in a matrix, the structure of the matrix can be used to control the particle surface structure, and even the entire particle structure.[157] A deposition process for fabricating quantum dot composite materials using the pulsed laser ablation supersonic expansion source has been developed.[158] This technique must be advanced in order to form materials whose surface structure is known and from which efficient devices can be constructed. It must also be combined with an approach to collection particles of within a narrow range of sizes, so that the benefits of quantum confinement can be reaped.

4.1.4 New Synthesis Approaches

While the pulsed laser ablation supersonic expansion approach to silicon nanoparticle synthesis has worked for us here, there are some drawbacks that might be overcome using another technique. The amount of material synthesized is very small, making it difficult to scale up the process for commercial applications and introducing challenges associated with charac-

terizing very thin films. The source produces a distribution of particle sizes, which makes it difficult to produce the clear cut emission wavelength as a function of size evidence for quantum confinement that many researchers would like us to have. The particles produced are bare and the films they build up into consist of merely particles embedded in a native oxide matrix. This morphology is not conducive to constructing devices for optoelectronic applications.

Different synthesis approaches may be capable of addressing these concerns. Techniques based on chemistry are capable of producing much more material than laser ablation. Equilibrium chemical techniques are likely to produce a more uniform particle size distribution than our highly nonequilibrium source. If the correct approach is chosen, it could be possible to grow the particles directly within a host matrix, addressing the film morphology problem. An interesting approach which incorporates all of these improvements is the block copolymer nanoreactor method of Cohen and co-workers, in which clusters are grown within polymer matrices. Cluster size is defined by the polymer system morphology, which is determined by thermodynamics and is thus an equilibrium process.[159] Such a material would allow for the performance of the aforementioned future work on a collection of particles of the same size, making the interpretation of the results much easier. The heterostructure aspect is built in, making the fabrication of actual devices simpler and surface structure control well defined.

Bibliography

[1] J. Weber, W. Schmid, and R. Sauer, Phys. Rev. B 21(6), 2401 (1980).

[2] B. Zheng, J. Michel, F.Y.G. Ren, L.C. Kimerling, D.C. Jacobsen, and J.M. Poate, Appl. Phys. Lett. 64, 2842 (1994).

[3] S. Oguz, W. Paul, T.F. Deutsch, B.-Y. Tsaur, and D.V. Murphy, Appl. Phys. Lett. 43(9), 849 (1983).

[4] L.C. Lenchyshyn, M.L.W. Thewalt, J.C. Sturm, P.V. Schwartz, N.L. Rowell, J.-P. Nöel, and D.C. Houghton, J. Electron. Mater. 22, 233 (1993).

[5] M. Stutzmann, M.S. Brandt, M. Rosenbauer, H.D. Fuchs, S. Finkbeiner, J. Weber, and P. Deák, J. Lumin. 57, 321 (1993).

[6] R.A. Street, Adv. Phys. 30(5), 593 (1981).

[7] J.I. Pankove and D.E. Carlson, Appl. Phys. Lett. 31(7), 450 (1977).

[8] B. Abeles and T. Tiedje, Phys. Rev. Lett. 51(21), 2003 (1983).

[9] D.J. Lockwood, Z.H. Lu, and J.-M. Baribeau, Phys. Rev. Lett. 76(3), 539 (1996).

[10] A.P. Alivisatos, Science 271, 933 (1996).

[11] S. Brandt and H.D. Dahman, *Interquanta* from *Quantum Mechanics on the Personal Computer*, (Springer Verlag, New York, 1989).

[12] L.E. Brus, J. Chem. Phys. 80(9), 4403 (1984).

[13] T. Takagahara and K. Takeda, Phys. Rev. B 46, 15578 (1992).

[14] A.D. Yoffe, Adv. Phys. 42, 173 (1993).

[15] M. Lannoo, C. Delerue, and G. Allan, Phys. Rev. Lett. 74, 3415 (1995).

[16] B. Delley and E.F. Steigmeier, Appl. Phys. Lett. 67, 2370 (1995).

[17] N.A. Hill and K.B. Whaley, J. Electron. Mater. 25, 269 (1996).

[18] J.P. Proot, C. Delerue, and G. Allan, Appl. Phys. Lett. 61 (16), 1948 (1992).

[19] M.S. Hybertsen, Phys. Rev. Lett. 72, 1514 (1994).

[20] C.B. Murray, D.J. Norris, and M.G. Bawendi, J. Am. Chem. Soc. 115, 8706 (1993).

[21] V. Narayanamurti, Physics Today 37(10), 24 (1984).

[22] S. Schmitt-Rink, D.A.B. Miller, and D.S. Chemla, Phys. Rev. B 35, 8113 (1987).

[23] P. Castrillo, D. Hessman, M.-E. Pistol, S. Anand, N. Carlsson, W. Seifert, and L. Samuelson, Appl. Phys. Lett. 67(13), 1905 (1995).

[24] R. Dingle, Festkörperprobleme 15, H.J. Queisser, ed., Pergammon, Braunschweig, 21 (1975).

[25] M. Wachter, F. Schaffler, H.-J. Herzog, K. Thonke, and R. Sauer, Appl. Phys. Lett. 63(3), 376 (1993).

[26] M. Racanelli and D.W. Greve, JOM 43, 32 (1991).

[27] P.N. Saeta and A.C. Gallagher, Phys. Rev. B 55, 4563 (1997).

[28] J.-M. Baribeau, D.J. Lockwood, and Z.-H. Lu, Mater. Res. Soc. Symp. Proc 382, 259 (1995).

[29] Z.H. Lu, D.J. Lockwood, and J.-M. Baribeau, Nature 378, 258 (1995).

[30] B.T. Sullivan, D.J. Lockwood, H.J. Labbé, and Z.-H. Lu, Appl. Phys. Lett. 69, 3149 (1996).

[31] R. Rossetti, S. Nakahara, and L.E. Brus, J. Chem. Phys. 79, 1986 (1983).

[32] M.A. Olshavsky, A.N. Goldstein, and A.P. Alivisatos, J. Am. Chem. Soc. 112, 9439 (1990).

[33] O.I. Mićić, C.J. Curtis, K.M. Jones, J. R. Sprague, and A.J. Nozik, J. Phys. Chem. 98, 4966 (1994).

[34] O.I. Mićić, J.R. Sprague, C.J. Curtis, K.M. Jones, J.L. Machol, A.J. Nozik, H. Giessen, B. Fluegel, G. Mohs, and N. Peyghambarian, J. Phys. Chem. 99(19), 7754 (1995).

[35] C.T. Dameron, R.N. Reese, R.K. Mehra, A.R. Kortan, P.J. Carroll, M.L. Steigerwald, L.E. Brus, and D.R. Winge, Nature 338, 596 (1989).

[36] R.J. Bandaranayake, G.W. Wen, J.Y. Lin, H.X. Jiang, and C.M Sorensen, Appl. Phys. Lett. 67(6), 831 (1995).

[37] S.H. Tolbert and A.P. Alivisatos, J. Chem. Phys. 102(11), 4642 (1995).

[38] S.H. Tolbert, A.B. Herhold, C.S. Johnson, and A.P. Alivisatos, Phys. Rev. Lett. 73(24), 3266 (1994).

[39] S. Sato, S. Nozaki, H. Morisaki, and M. Iwase, Appl. Phys. Lett. 66(23), 3176 (1995).

[40] J. Jiang, K. Chen, X. Huang, Z. Li, and D. Feng, Appl. Phys. Lett. 65(14), 1799 (1994).

[41] S. Vepřek, Z. Iqbal, and F.-A. Sarott, Phil. Mag. B 45(1), 137 (1982).

[42] S.H. Tolbert, A.B. Herhold. L.E. Brus, and A.P. Alivisatos, Phys. Rev. Lett. 76(23), 4384 (1996).

[43] S. Fafard, R. Leon, D. Leonard, J.L. Merz, and P.M. Petroff, Phys. Rev. B 52, 5752 (1995).

[44] S. Fafard, Z. Wasilweski, J. McCaffrey, S. Raymond, and S. Charbonneau, Appl. Phys. Lett. 68, 991 (1996).

[45] D. Hessman, P. Castrillo, M.-E. Pistol, C. Pryor, and L. Samuelson, Appl. Phys. Lett. 69, 749 (1996).

[46] M. Sopanen, M. Taskinen, H. Lipsanen, and J. Ahopelto, Appl. Phys. Lett. 69, 3393 (1996).

[47] W.A. Saunders, P.C. Sercel, H.A. Atwater, and K.J. Vahala, Appl. Phys. Lett. 60(8), 950 (1992).

[48] A. Anedda, A. Serpi, V.A. Karavanskii, I.M. Tiginyanu, and V.M. Ichizli, Appl. Phys. Lett. 67, 3316 (1995).

[49] F. Henneberger, J. Puls, C. Spiegelberg, A. Schulzgen, H. Rossman, V. Jungnickel, and A.I. Ekimov, Semicond. Sci. Tech. 6, A41 (1991).

[50] M.D. Dvorak, B.L. Justus, D.K. Gaskill, and D.G. Hendershot, Appl. Phys. Lett. 66(7), 804 (1995).

[51] A. Nakamura, Y.L. Lee, T. Kataoka, and T. Tokizaki, J. Lum. 60&61, 376 (1994).

[52] L.T. Canham, Appl. Phys. Lett. 57(10), 1047 (1990).

[53] A. Uhlir, Bell Syst. Tech. J. 35, 333 (1956).

[54] M.I.J. Beale, J.D. Benjamin, M.J. Uren, N.G. Chew, and A.G. Cullis, J. Cryst. Growth 75, 408 (1986).

[55] S.M. Prokes, J. Appl. Phys. 73(1), 407 (1993).

[56] V. Petrova-Koch, T. Muschik, A. Kux, B.K. Meyer, F. Koch, and V. Lehmann, Appl. Phys. Lett. 61(8), 943 (1992).

[57] S.C. Bayliss, D.A. Hutt, Q. Zhang, P. Harris, N.J. Phillips, and A. Smith, Thin Solid Films 255, 128 (1995).

[58] L. Tsybeskov, Ju. V. Vandyshev, and P.M. Fauchet, Phys. Rev. B 49(11), 7821 (1994).

[59] V. Lehmann and U. Gösele, Appl. Phys. Lett. 48(8), 381 (1991).

[60] M.I.J. Beale, N.G. Chew, M.J. Uren, A.G. Cullis, and J.D. Benjamin, Appl. Phys. Lett. 46(1), 86 (1985).

[61] A.G. Cullis, L.T. Canham, G.M. Williams, P.W. Smith, and O.D. Dosser, J. Appl. Phys. 75(1), 493 (1994).

[62] L. Pavesi, C. Mazzoleni, A. Tredicucci, and V. Pellegrini, Appl. Phys. Lett. 67, 3280 (1995).

[63] J. von Behren, K.B. Ũçer, L. Tsybeskov, J.V. Vandyshev, and P.M. Fauchet, J. Vac. Sci. Tech. B 13, 1225 (1995).

[64] Y. Saito, J. Cryst. Growth 47, 61 (1979).

[65] S. Iijima, Jpn. J. Appl. Phys. 26(3), 357 (1987).

[66] J. Dundurs, L.D. Marks, and P.M. Ajayan, Phil. Mag. A 57, 605 (1988).

[67] P.M. Ajayan and L.D. Marks, Phase Trans. 24-26, 229 (1990).

[68] S. Hayashi and H. Abe, Jap. J. Appl. Phys. 23(11), L824 (1984).

[69] D.E. Powers, S.G. Hansen, M.E. Geusic, A.C. Pulu, J.B. Hopkins, T.G. Dietz, M.A. Duncan, P.R.R. Langridge-Smith, and R.E. Smalley, J. Phys. Chem. 86, 2556 (1982).

[70] J.R. Heath, Y. Liu, S.C. O'Brien, Q.-L. Zhang, R.F. Curl, F.K. Tittel, and R.E. Smalley, J. Chem. Phys. 83, 5520 (1985).

[71] R. Schäfer, S. Schlecht, J. Woenckhaus, and J.A. Becker, Phys. Rev. Lett. 76, 471 (1996).

[72] M.L. Mandich, W.D. Reents, Jr., and K.D. Kolenbrander, Pure & Appl. Chem. 62(9), 1653 (1990).

[73] M.F. Jarrold, U. Ray, and Y. Ijiri, Z. Phys. D 19, 337 (1991).

[74] E.C. Honea, A. Ogura, C.A. Murray, K. Raghavachari, W.O. Sprenger, M.F. Jarrold, and W.L. Brown, Nature 366, 42 (1993).

[75] A. Ogura, E.C. Honea, C.A. Murray, K. Raghavachari, W.O. Sprenger, M.F. Jarrold, and W.L. Brown, Mater. Res. Soc. Symp. Proc. 332, 333 (1994).

[76] M.F. Jarrold and V.A. Constant, Phys. Rev. Lett. 67(21), 2994 (1991).

[77] M.L. Mandich, Intl. J. Mod. Phys. B 6(23&24), 3747 (1992).

[78] K. Raghavachari and V. Logovinsky, Phys. Rev. Lett. 55(26), 2853 (1985).

[79] K. Raghavachari, J. Chem. Phys. 84(10), 5672 (1986).

[80] D. Tomańek and M.A. Schluter, Phys. Rev. B 36(2), 1208 (1987).

[81] S. Li, R.J. Van Zee, W. Weltner, Jr., and K. Raghavachari, Chem. Phys. Lett. 243, 275 (1995).

[82] K. Jackson, M.R. Pederson, D. Porezag, Z. Hajnal, and T. Frauenheim, Phys. Rev. B 55(4), 2549 (1997).

[83] M.R. Pederson, K. Jackson, D.V. Porezag, Z. Hajnal, and T. Frauenheim, Phys. Rev. B. 54(4), 2863 (1996).

[84] C.H. Patterson and R.P. Messmer, Phys. Rev. B 42(12), 7530 (1990).

[85] H. Kupka and K. Jug, Chem. Phys. 130, 23 (1989).

[86] K. Jug and M. Krack, Chem. Phys. 173, 439 (1993).

[87] M.V. Ramakrishna and J. Pan, J. Chem. Phys. 101(9), 8108 (1994).

[88] U. Röthlisberger, W. Andreoni, and M. Parinello, Phys. Rev. Lett. 72(5), 665 (1994).

[89] E. Kaxiras and K. Jackson, Phys. Rev. Lett. 71(5), 727 (1993).

[90] K.A. Littau, P.J. Szajowski, A.J. Muller, A.R. Kortan, and L.E. Brus, J. Phys. Chemi. 97, 1224 (1993).

[91] S. Schuppler, S.L. Friedman, M.A. Marcus, D.L. Adler, Y.-H. Xie, F.M. Ross, Y.J. Chabal, T.D. Harris, L.E. Brus, W.L. Brown, E.E. Chaban, P.F. Szajowski, S.B. Christman, and P.H. Citrin, Phys. Rev. B 52, 4910 (1995).

[92] W.A. Saunders, P.C. Sercel, R.B. Lee, H.A. Atwater, K.J. Vahala, R.C. Flagan, and E J. Escorcia-Aparcio, Appl. Phys. Lett. 63, 1549 (1993).

[93] J.R. Heath, Science 258, 1131 (1992).

[94] J.M. Jasinski and F.K. LeGoues, Chem. Mater. 3, 989 (1991).

[95] S. Furukawa and T. Miyasato, Phys. Rev. B 38, 5726 (1988).

[96] B. Hamilton, Semicond. Sci. Tech. 10(9), 1187 (1995).

[97] G.G. Qin, H.Z. Song, B.R. Zhang, J. Lin, J.Q. Duan, and G.Q. Yao, Phys. Rev. B 54, 2548 (1996).

[98] J.H. Stathis and M.A. Kastner, Phys. Rev. B 35, 2972 (1987).

[99] A. Loni, A.J. Simons, P.D.J. Calcott, and L.T. Canham, J. Appl. Phys. 77(7), 3557 (1995).

[100] Y. Kanemitsu, S. Okamoto, M. Otobe, and S. Oda, Phys. Rev. B 55, R7375 (1997).

[101] K. Takeda and K. Shiraishi, Sol. St. Comm. 85(4), 301 (1993).

[102] Y.H. Xie, W.L. Wilson, F.M. Ross, J.A. Mucha, E.A. Fitzgerald, J.M. Macaulay, and T.D. Harris, J. Appl. Phys. 71, 2403 (1992).

[103] S.M. Prokes, J. Mater. Res. 11, 305 (1996).

[104] P.D.J. Calcott, K.J. Nash, L.T. Canham, M.J. Kane, and D. Brumhead, J. Phys.: Cond. Matt. 5, L91 (1993).

[105] L.E. Brus, P.F. Szajowski, W.L. Wilson, T.D. Harris, S. Schuppler, and P.H. Citrin, J. Am. Chem. Soc. 117, 2915 (1995).

[106] S.C. Bayliss, D.A. Hutt, Q. Zhang, P. Harris, N.J. Phillips, and A. Smith, Thin Solid Films 255, 128 (1995).

[107] M. Kondo and H. Yokomichi, J. Phys. Soc. Jpn. 63B, 145 (1994).

[108] F. Koch, V. Petrova-Koch, and T. Muschik, J. Lum. 57, 271 (1993).

[109] A. Nakajima, T. Itakura, S. Watanabe, and N. Nakayama, Appl. Phys. Lett. 61(1), 46 (1992).

[110] W.L. Wilson, P.F. Szajowski, and L.E. Brus, Science 262, 1242 (1993).

[111] V. Petrova-Koch, T. Muschik, A. Kux, B.K. Meyer, F. Koch, and V. Lehmann, Appl. Phys. Lett. 61(8), 943 (1992).

[112] M. Rosenbauer, M. Stutzmann, H.D. Fuchs, S. Finkbeiner, and J. Weber, J. Lum. 57, 153 (1993).

[113] J. Lin, L.Z. Zhang, B.R. Zhang, B.Q. Zong, and G.G. Qin, J. Phys.: Cond. Matt. 6, 565 (1994).

[114] E. Werwa, A.A. Seraphin, L.A. Chiu, C. Zhou, and K.D. Kolenbrander, Appl. Phys. Lett. 64, 1821 (1994).

[115] K.D. Kolenbrander and M.L. Mandich, J. Chem. Phys. 92, 4759 (1990).

[116] S. DePaul, D. Pullman, and B. Freidrich, J. Phys. Chem. 97, 2167 (1993).

[117] C.-R. Wang, R.-B. Huang, Z.-Y. Liu, and L.-S. Zheng, Chem. Phys. Lett. 227, 103 (1994).

[118] K. Raghavachari, Phase Trans. 24-26, 35 (1990).

[119] L.A. Chiu, S.M. Thesis, Massachusetts Institute of Technology (1993).

[120] L.A.Chiu, A.A. Seraphin, and K.D. Kolenbrander, J. Electron. Mater. 23(3), 347 (1994).

[121] A. A. Seraphin, Ph.D. Thesis, Massachusetts Institute of Technology (1996).

[122] A.A. Seraphin, S.-T. Ngiam, and K.D. Kolenbrander, J. Appl. Phys. 80(11), 6429 (1996).

[123] W.R. Cannon, S.C. Danforth, J.H. Flint, J.S. Haggerty, and R.A. Marra, J. Am. Chem. Soc. 65, 324 (1982).

[124] D. T. Castro, Sc.D. Thesis, Massachusetts Institute of Technology (1997).

[125] H.U. Hostettler and R.B. Bernstein, Rev. Sci. Inst. 31, 872 (1960).

[126] M. Arnold, J. Kowalski, G. Zu Putlits, T. Stehlin, and F. Trager, Surf. Sci. 156, 149 (1985).

[127] J.F. Roux, B. Cabaud, G. Fuchs, D. Guillot, A. Hoareau, and P. Melinon, Appl. Phys. Lett. 64, 1212 (1994).

[128] U. Buck and H. Meyer, Surface Science 156, 275 (1985).

[129] A. Goerke, M. Feser, H. Palm, C.P. Schulz, and I.V. Hertel, Z. Phys. D 19, 157 (1991).

[130] A. Ashkin, Science 210, 1081 (1980).

[131] A .Ashkin, Phys. Rev. Lett. 24(4), 156 (1970).

[132] A. Ashkin, Phys. Rev. Lett. 25(19), 1321 (1970).

[133] G. Timp, R.E. Behringer, D.M. TEnnant, J.E. Cunningham, M. Prentiss, and K.K. Berggren, Phys. Rev. Lett. 69(11), 1636 (1992).

[134] J.J. McClelland, R.E. Scholten, E.C. Palm, and R.J. Celotta, Science 262, 877 (1993).

[135] R.J. Celotta, R. Gupta, R.E. Scholten, and J.J. McClelland, J. Appl. Phys. 79(8), 6079 (1996).

[136] M. Morinaga, M. Yasuda, T. Kishimoti, F. Shimizu, J. Fujita, and S. Matsui, Phys. Rev. Lett. 77(5), 802 (1996).

[137] P.H. Dawson and N.R. Whetten, Adv. Electronics and Electron Phys. 27, 59 (1969).

[138] R. Davis and M. Frearson, *Mass Spectrometry*, (John Wiley & Sons, New York, 1987).

[139] "SIMION 3D Version 6.0" by David A. Dahl, 43ed ASMS Conference on Mass Spectrometry and Allied Topics, May 21-26 1995, Atlanta, GA, p.717.

[140] B.D. Cullity, *Elements of X-Ray Diffraction*, (Addison-Wesley, Reading, MA, 1978).

[141] R.P. Vasquez, R.W. Fathauer, T. George, A. Ksendzov, and T.L. Lin, Appl. Phys. Lett. 60(8), 1004 (1992).

[142] M. Nirmal, private communication.

[143] S. Fukatsu, J. Cryst. Gr. 157, 1 (1995).

[144] K. Morigaki, M. Yamaguchi, and I. Hirabayashi, J. Non-Cryst. Sol. 164-166, 571 (1993).

[145] I. Mihalcescu, J.C. Vial, A. Bsiesy, F. Muller, R. Romestain, E. Martin, C. Delerue, M. Lannoo, and G. Allan, Phys. Rev. B 51, 17605 (1995).

[146] M. Koos, I. Pocsik, and E.B. Vazsonyi, Appl. Phys. Lett. 62, 1797 (1993).

[147] C. Delerue, M. Lannoo, G. Allan, E. Martin, I. Mihalcescu, J.C. Vial, R. Romestain, F. Muller, and A. Bsiesy, Phys. Rev. Lett. 75, 2228 (1995).

[148] A.I. Ekimov, F. Hache, M.C. Schanne-Klein, D. Richard, C. Flytzanis, I.A. Kudryavtsev, T.V. Yazeva, A.V. Rodina, and Al. L. Efros, J. Opt. Soc. Am. B 10, 100 (1993).

[149] S. Guha, G. Hendershot, D. Peebles, P. Steiner, F. Kozlowski, and W. Lang, Appl. Phys. Lett. 64, 613 (1994).

[150] A.R. Beattie and P.T. Landsberg, Proc. Royal Soc. London 249, 16 (1959).

[151] L.C. Feldman and J.W. Mayer, *Fundamentals of Surface and Thin Film Analysis*, (Elsevier, New York, 1986) p. 257.

[152] G.W. Neudeck, *The PN Junction Diode*, (Addison-Wesley, Reading, MA, 1989), p. 128.

[153] R.R. Kunz, P.M. Nitishin, H.R. Clark, M. Rothschild, and B. Ahern, Appl. Phys. Lett. 67(12), 1766 (1995).

[154] R.P. Vasquez, A. Madhukar, and A.R. Tanguay, Jr., J. Appl. Phys. 58, 2337 (1985).

[155] J.D. Joannopoulos and M.L. Cohen, Phys. Rev. B 7, 2644 (1973).

[156] J. Singh, Phys. Rev. B 23, 4156 (1981).

[157] S. Balasubramanian, S.M. Thesis, Massachusetts Institute of Technology (1996).

[158] S.-T. Ngiam, Ph.D. Thesis, Massachusetts Institute of Technology (1996).

[159] V. Sankaran, J. Yue, R.E. Cohen, R.R. Schrock, and R.J. Silbey, Chem. Mater. 5(8),1133 (1993).